FILTERBANK MULTICARRIER TECHNIQUES FOR RADIO FREQUENCY AND UNDERWATER CHANNELS

by

Chung Him Yuen

A dissertation submitted to the faculty of
The University of Utah
in partial fulfillment of the requirements for the degree of

Doctor of Philosophy

Department of Electrical and Computer Engineering

The University of Utah

May 2015

The University of Utah Graduate School

STATEMENT OF DISSERTATION APPROVAL

The dissertation of **Chung Him Yuen**

has been approved by the following supervisory committee members:

Behrouz Farhang-Boroujeny	, Chair	**1/29/2015** Date Approved
Rong-Rong Chen	, Member	**1/29/2015** Date Approved
Cynthia Furse	, Member	**1/29/2015** Date Approved
Tolga Tasdizen	, Member	**1/29/2015** Date Approved
Sneha Kasera	, Member	**1/29/2015** Date Approved

and by **Gianluca Lazzi** , Chair/Dean of

the Department/College/School of **Electrical and Computer Engineering**

and by David B. Kieda, Dean of The Graduate School.

ABSTRACT

The use of multicarrier techniques has allowed the rapid expansion of broadband wireless communications. Orthogonal frequency division multiplexing (OFDM) has been the most dominant technology in the past decade. It has been deployed in both indoor Wi-Fi and cellular environments, and has been researched for use in underwater acoustic channels.

Recent works in wireless communications include the extension of OFDM to multiple access applications. Multiple access OFDM, or orthogonal frequency division multiple access (OFDMA), has been implemented in the third generation partnership project (3GPP) long-term evolution (LTE) downlink. In order to reduce the intercarrier interference (ICI) when user's synchronization is relaxed, filterbank multicarrier communication (FBMC) systems have been proposed. The first contribution made in this dissertation is a novel study of the classical FBMC systems that were presented in 1960s. We note that two distinct methods were presented then. We show that these methods are closely related through a modulation and a time/frequency scaling step. For cellular channels, OFDM also has the weakness of relatively large peak-to-average power ratios (PAPR). A special form of OFDM for the uplink of multiple access networks, called single carrier frequency division multiple access (SC-FDMA), has been developed to mitigate this issue. In this regard, this dissertation makes two contributions. First, we develop an optimization method for designing an effective precoding method for SC-FDMA systems. Second, we show how an equivalent to SC-FDMA can be developed for systems that are based on FBMC.

In underwater acoustic communications applications, researchers are investigating the use of multicarrier communication systems like OFDM in underwater channels. The movement of the communicating vehicles scales the received signal along the time axis, which is often referred to as Doppler scaling. To undo the signal degradation, researchers have investigated methods to estimate the Doppler scaling factor and restore the original signal using resampling. We investigate a method called nonuniform fast Fourier transform (NUFFT) and apply that to increase the precision in the detection and correction of the Doppler scaling factor. NUFFT is applied to both OFDM and FBMC and its performance over the experimental data obtained from at sea experiments is investigated.

CONTENTS

LIST OF FIGURES

LIST OF TABLES

CHAPTER 1

INTRODUCTION

The use of multicarrier techniques has allowed the rapid expansion of broadband wireless communications. Orthogonal frequency division multiplexing (OFDM) has been the most dominant technology in the past decade. It has been deployed in both indoor Wi-Fi and cellular environments, and has been researched for use in underwater acoustic channels. OFDM is desirable because of a number of advantages it offers. For example, the amount of intersymbol interference (ISI) across data symbols is related to the span of multipath across time, and in OFDM we multiplex a high-rate stream of data symbols into a number of parallel subcarriers that are at a much slower rate. In these subcarriers, data symbols are modulated by a set of complex sine waves, which means that at the receiver we can perform simple single-tap equalization. These closely spaced orthogonal subcarriers also partition the available bandwidth to maximize the utilization of bandwidth efficiency and transmission rate. These points are understood and documented in the literature [1], [2].

Recent works in wireless communications include the extension of OFDM to multiple access applications [3]. Multiple access OFDM, or orthogonal frequency division multiple access (OFDMA), has been implemented in LTE downlinks. Another OFDM based technology, multi-user multiple-input and multiple-output (MU-MIMO), has been listed for the standard in IEEE 802.11ac Wave 2, and this allows multiple devices to communicate with the wireless Wi-Fi router simultaneously.

In the multiple access situation, each user node in the network is assigned a subset of the available subcarriers. Signals from different users must be synchronized at the receiver to prevent intercarrier interference (ICI). OFDMA works well in the network downlink of a base station, as all of the subcarriers are transmitted together from the transmitter in the base station. However, in the network uplink synchronization can be an issue, as different user nodes are transmitting their signals separately. Due to the relatively large side-lobes of the spectra of the subcarriers in the OFDM signal, ICI will limit the performance in these situations.

Synchronization of all of the users is a nontrivial task, and additional signal processing procedures have to be performed to address these issues for OFDM. This increases the complexity to an OFDM receiver significantly [4]. In order to reduce the ICI due to user synchronization issues, filterbank multicarrier communication (FBMC) systems have been proposed. FBMC systems use a bank of filters, which are a modulated version of a prototype filter, in the synthesis and analysis of multicarrier signals. The prototype filter is designed with small side-lobes and can limit the ICI to adjacent subcarrier bands [5].

For cellular channels, OFDM also has the weakness of relatively large peak-to-average power ratios (PAPR). This affects the power efficiency and increases the cost and complexity of the amplifiers at the transmitters in the network uplink. A special form of OFDM for the uplink of multiple access networks, called single carrier frequency division multiple access (SC-FDMA), has been developed to mitigate this issue [17]. SC-FDMA applies precoding in the transmitter to lower the PAPR in the LTE uplink. In this application, filterbank multicarrier techniques can be applied to further reduce the PAPR by reducing the side-lobes of the subcarriers. This stops the side-lobes from adding constructively and increasing the PAPR.

In underwater acoustic communications applications, researchers are investigating the use of multicarrier communication systems like OFDM in underwater channels. The impact of the mobility of the communicating vehicles is one of the major issues affecting the performance in underwater acoustic channels [31], [32], [33]. Unlike electromagnetic waves where the signal travels at the speed of light, underwater acoustic signals propagate at the speed of sound. The movement of the communicating vehicles scales the received signal along the time axis, which is often referred to as Doppler scaling. For multicarrier systems like OFDM, the main effect of Doppler scaling on the received signal is the frequency dependent shifts of the center frequency of the subcarriers. The misalignment of the subcarriers creates a destructive distortion to the received signal.

To undo the signal degradation, researchers have investigated methods to estimate the Doppler scaling factor and restore the original signal using resampling. However, if there is a slight offset in the detection and correction of the Doppler scaling factor, the effect of ICI will degrade the OFDM signal. A method called Non-Uniform Fast Fourier Transform (NUFFT) can increase the precision in the detection and correction of the Doppler scaling factor, and the use of FBMC can reduce the amount of ICI and improve the bit error rate in the detection of the received signal. These possibilities are explored in this dissertation.

In this chapter, the basics of OFDM are discussed in Sec. 1.1. Several filterbank

multicarrier communications methods are introduced in Sec. 1.2. Single carrier frequency division multiple access (SC-FDMA) is presented in Sec. 1.3. The introduction of underwater acoustic channels with Doppler scaling is given in Sec. 1.4. Finally, the contributions and organization of this dissertation are described.

1.1 Orthogonal Frequency Division Multiplexing (OFDM)

In an OFDM system, the transmitter starts by taking the multiplexed data symbol vector $\mathbf{s}[n] = [s_0[n], s_1[n], \cdots, s_{N-1}[n]]^{\mathrm{T}}$ and performs the N-point inverse discrete Fourier transform (IDFT) to obtain the OFDM symbol $\mathbf{S}[n] = [S_0[n], S_1[n], \cdots, S_{N-1}[n]]^{\mathrm{T}}$, where

$$S_l[n] = \frac{1}{N} \sum_{k=0}^{N-1} s_k[n] e^{-j\frac{2\pi k}{N} l}. \tag{1.1}$$

If we define $\mathbf{f}_k$ as $\mathbf{f}_k = \left[1, e^{-j\frac{2\pi k}{N}1}, e^{-j\frac{2\pi k}{N}2}, \cdots, e^{-j\frac{2\pi k}{N}(N-1)}\right]^{\mathrm{T}}$, then we can write (1.1) as

$$\mathbf{S}[n] = \frac{1}{N} \sum_{k=0}^{N-1} s_k[n] \mathbf{f}_k. \tag{1.2}$$

This shows that for each stream the kth symbol $s_k[n]$ modulates a complex carrier at frequency $\frac{k}{N}$, and the output OFDM symbol consists of the sum of these signals at different subcarriers.

For the purpose of transmission, the OFDM symbols vectors $\mathbf{S}[n]$ are concatenated and modulated to an RF band. At the receiver, the signal is demodulated from the RF band back to the baseband. In an ideal channel environment, applying the discrete Fourier transform (DFT) to each OFDM symbol at the receiver will give us the multiplexed data symbol vector $\mathbf{s}[n]$. However, the presence of multipath fading in the channel will introduce intersymbol interference (ISI) among the OFDM symbols at the receiver. To eliminate ISI, a guard interval consisting of the cyclic prefix (CP) is inserted before each OFDM symbol at the transmitter, and the length of the CP is chosen to be more than the length of the channel impulse response. A single-tap equalizer is then used for each subcarrier channel to undo the effect of the complex channel gain.

1.2 Filterbank Multicarrier (FBMC) Methods

As mentioned previously, synchronization problems of OFDM can be resolved if the filters that synthesize the subcarrier signals had smaller side-lobes. A set of filter banks can be designed with small side-lobes for the synthesis and analysis of multicarrier signals.

The first FMBC system was proposed by Chang [6] in which a parallel set of real valued pulse amplitude modulated (PAM) symbol sequences was transmitted through a bank of overlapping filters within a minimum bandwidth. In order to obtain high efficiency, overlapping vestigial side-band (VSB) modulated signals were used. Later, Saltzberg [7] extended the idea and showed how Chang's method could be modified for complex-valued quadrature amplitude modulated (QAM) symbols using double side-band modulated format. We refer to Chang's method as cosine modulated multitone (CMT) and Saltzberg's method as staggered modulated multitone (SMT).

1.2.1 Cosine Modulated Multitone (CMT)

In CMT, parallel streams of PAM data symbols are transmitted through a set of overlapping vestigial side-bands (VSB) that are minimally spaced to maximize the bandwidth efficiency. It was first introduced by Chang in 1966. Change's method was later re-invented by Sandberg and Tzannes in the 1990s who were developing a method for digital subscriber line (DSL) called discrete wavelet multitone (DWMT).

With a square-root Nyquist filter and an ideal channel, perfect reconstruction of the PAM data symbols can be achieved. Under non-ideal channel scenarios, simple equalizer designs were proposed.

1.2.2 Staggered Modulated Multitone (SMT)

In SMT, the transmitter first separates the real and imaginary parts of the complex QAM symbols and they are transmitted with an offset in time that is half of the symbol duration. This is an extension of Chang's method that was developed by Saltzberg.

Similar to CMT, perfect reconstruction of the QAM symbols can be achieved by using a square-root Nyquist filter at the transmitter and receiver in ideal channel conditions.

1.3 Single Carrier Frequency Division Multiple Access (SC-FDMA)

The third generation partnership project (3GPP) long-term evolution (LTE) radio standard has adopted a special form of the OFDM method for the uplink of multiple access networks. This method, which is called single carrier frequency division multiple access (SC-FDMA), applies a precoding to each user data set in each OFDM symbol to control its peak-to-average power ratio (PAPR). Reducing the PAPR in any transmission system is always desirable as it allows use of more power efficient and cheaper amplifiers at the transmitter. The standard has recognized this as a critical component to the success

of 3GPP LTE products, noting that reducing PAPR directly translates to a lower power consumption and thus a longer battery life.

The basic principles of SC-FDMA, in the form adopted in the 3GPP LTE standard, are laid out in [17], and an example of the transmitter structure is presented in [27]. Fig. 1.1 presents a block diagram of such a SC-FDMA transmitter. A user data stream $s[n]$ is passed through a serial-to-parallel converter (S/P) that divides it into M parallel substreams. In a conventional OFDMA, these substreams are directly allocated to M subcarriers in an OFDM modulator (the IFFT block in Fig. 1.1) with a total of $N > M$ subcarriers. In SC-FDMA, a precoder is inserted between the S/P and OFDM modulator. The precoder takes the M output samples of S/P and premultiplies them with a DFT matrix $\mathbf{P}$ of size $M \times M$.

1.4 OFDM and FBMC in Doppler Scaling Channels

Recently, due to the need for high speed communication in underwater acoustic (UWA) channels, multicarrier communication techniques have been researched and proposed for UWA communications. Due to the limitation of electromagnetic (EM) wave propagation in water, communication in underwater channels is established through acoustical waves. The far slower speed of the sound, as compared to EM waves, creates peculiar problems in underwater acoustic (UWA) channels that have no parallel in the EM medium. The particular problem that is explored as part of this dissertation is the impact of the mobility of the communicating vehicles on the UWA signals: *the time is scaled* by a factor equal to $1 + v(t)/c$, when the spacing between the vehicles is varied at a speed of $v(t)$ and c denotes the speed of the propagating sound waves. The time scaling is often referred to as *Doppler scaling*.

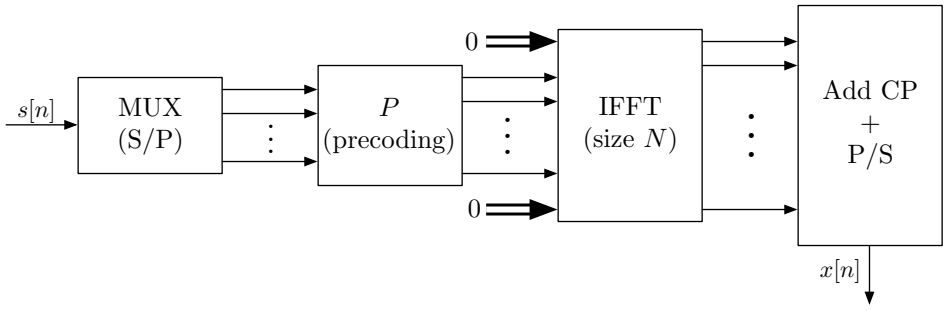

Figure 1.1: An SC-FDMA transmitter.

1.5 Contribution of the Dissertation

This dissertation will focus on the use of FBMC techniques in several different applications. First, for SMT and CMT we perform mathematical analysis on the impact of timing and carrier offset, and study in detail the similarities and differences between the two FBMC systems. Second, with the use of FBMC techniques, we analyze mathematically the effect of the precoder on an SC-FDMA system and present an optimal solution to a design that gives us the lowest PAPR in SC-FDMA. We show that the complementary cumulative distribution function (CCDF) of our design has a lower PAPR when we compare it with existing precoders using software simulations. Third, we perform analysis of OFDM and FBMC performance in UWA channels with Doppler scaling. We propose the method of NUFFT to estimate and correct Doppler scaling in an underwater environment, and show that we are able to extract the correct data symbols with FBMC having lower mean square error than OFDM.

The contributions of this dissertation are as follows:

- We analyze mathematically the timing and carrier offset sensitivity for SMT and CMT systems. Using closed form equations, we identify the signal to interference ratio and plot it versus the amount of timing or carrier offset. By understanding the timing and carrier offset sensitivity of these two FBMC systems, we then show that there is a simple relationship between SMT and CMT and we propose a novel method of how one can be transformed into the other one with the multiplication of a complex sine wave. This contribution has been published in [22].

- We present a novel formulation of SC-FDMA which is a special form of OFDM signaling for the uplink of multiple access networks in the 3GPP LTE radio standard. We explore possible mimicking of the DFT precoding method for FBMC and investigate the direct application of SC-FDMA to FBMC systems. We compare the results with a single carrier SMT system and show how FBMC can reduce the PAPR significantly over SC-FDMA even without the precoder. Relevant publications are [23] and [24].

- We investigate the use of DFT precoders with window functions having rolled-off edges in SC-FDMA, and develop further analysis of SC-FDMA that explains the reasons behind why the conventional SC-FDMA precoding with a rectangular window has inferior performance to the cases where a window function with smoothly rolled-off edges is used. Several different prototype filters used commonly in FBMC systems

are applied as the window function in the precoder and the PAPR performance is investigated and compared to conventional SC-FDMA. Closed form equations are developed to find the upperbounds for the PAPR of these systems. Relevant publications are [24] and [25].

- Using the minimization of the variance of the instantaneous power of the output signal of the transmitter as a means of reducing PAPR to near its minimum value, we develop a mathematical procedure to search for an optimal window that minimizes the PAPR. We formulate the problem in the form of a method of Lagrange multipliers and analyze its second-order conditions to confirm analytically that the optimal window is indeed a strict local minimizer. We also analyze and compensate the noise enhancement penalty of the optimal window. Our analysis also leads us to find new window functions that further reduce the PAPR and improve the bit error rate (BER) performance. Relevant publications are [24] and [25].

- We investigate the use of OFDM and FBMC systems for underwater acoustic channels with Doppler scaling where the communicating vehicles are moving. We show how the existence of Doppler scaling leads to unevenly spaced sampling in the receiver. We introduce the use of nonuniform fast Fourier transform (NUFFT) in detection of multicarrier signals in the presence of Doppler scaling in which the received samples are unevenly spaced. We show how NUFFT can be implemented using numerical approximation methods and present the equations for the procedure. Relevant publications are [36], [37] and [41].

- We present a method of Doppler scaling estimation by using a novel pilot structure in which isolated pilot subcarriers are inserted in an OFDM or FBMC underwater acoustic signal. A gradient search method is proposed to perform acquisition and tracking of the Doppler scaling factor using NUFFT. We show how our estimation method performs better than traditional resampling in both linear and nonlinear Doppler scaling. We develop the necessary equations that show how NUFFT should be applied to undo the effect of Doppler scaling if the amount of Doppler scaling is known to us. Using both software simulation and real world at-sea experiment results, we show how our novel method is able to estimate and correct the effect of Doppler scaling in underwater acoustic (UWA) channels due to the mobility of the communicating vehicles. Furthermore, we show that FBMC performs better than OFDM in terms of

mean square error of the detected data symbols. Relevant publications are [36], [37] and [41].

1.6 Organization of the Dissertation

In Chapter 2, a review on FBMC systems is presented. The structures of the SMT and CMT transceiver systems are discussed. Timing and carrier frequency offset sensitivity analyses are performed, and the equivalence relationship between SMT and CMT is shown mathematically.

In Chapter 3, the extension of SC-FDMA to FBMC systems is discussed. A novel formulation of SC-FDMA is presented. Analysis of using the DFT precoding method for FBMC is performed. Comparison of the results with a single carrier SMT system using cumulative complementary distribution functions is presented, and it is shown how FBMC can reduce the PAPR significantly over SC-FDMA even without the precoder.

In Chapter 4, the use of DFT precoders with window functions having rolled-off edges in SC-FDMA was investigated. Analysis of PAPR in SC-FDMA with different window functions used commonly in FBMC systems is performed. A novel method is shown to explain why the conventional SC-FDMA precoding with a rectangular window has inferior performance to the cases where a window function with smoothly rolled-off edges is used. Closed form equations are developed to find the upperbounds for the PAPR of these systems. With the use of variance of the instantaneous power, a mathematical procedure is developed to search for an optimal window that minimizes the PAPR. Compensation of noise enhancement penalty is performed to further reduce the PAPR and improve the BER performance.

In Chapter 5, the use of OFDM and FBMC systems for underwater acoustic channels with Doppler scaling is investigated. The existence of Doppler scaling leads to unevenly spaced sampling in the receiver. The application of using NUFFT in the detection of multicarrier signals in the presence of Doppler scaling is proposed. Implementation of NUFFT is presented using numerical approximation methods with closed form equations.

In Chapter 6, the method of Doppler scaling estimation using a novel pilot structure is proposed. Isolated pilot subcarriers are inserted in an OFDM or FBMC underwater acoustic signal, and a gradient search method is used with NUFFT to perform acquisition and tracking of the Doppler scaling factor. Performance comparison is done to show how our estimation method performs better than tradition resampling in both linear and nonlinear Doppler scaling. Necessary equations are developed to show how NUFFT can be applied to undo the effect of Doppler scaling when the Doppler scaling factor is known to the receiver.

Using both software simulation and real world at-sea experiment results, it is shown how our novel method is able to estimate and correct the effect of Doppler scaling in UWA channels due to the mobility of the communicating vehicles, and how FBMC performs better than OFDM in terms of mean square error of the detected data symbols.

Finally, in Chapter 7, the concluding remarks and future research are presented. Several topics of future research are identified and proposed.

CHAPTER 2

REVIEW OF FILTERBANK MULTICARRIER SYSTEMS

Filterbank multicarrier (FBMC) systems use filterbanks to divide the available bandwidth of a channel into a number of subcarriers. FBMC systems are a class of multicarrier communication systems that are different from the OFDM system which is currently used in a majority of communication applications. First, unlike OFDM, FBMC does not require guard intervals, which results in improved bandwidth efficiency. Second, unlike OFDM in which there is significant overlap among the subcarriers due to the significant side lobes, each subcarrier in FBMC only overlaps with its adjacent counterparts. This lowers the sensitivity issue due to carrier offsets, doppler effects, and loss of synchronization of carriers at different nodes in multiple access applications. Third, implementation of FBMC is more complex than OFDM due to the prototype filters. The complexity can be lowered by using polyphase structures.

In 1966, Chang [6] proposed an FBMC technique in which real-valued pulse amplitude modulated (PAM) symbols were transmitted over a set of (partially) overlapping vestigial side-band (VSB) modulated channels. A year later in 1967, Saltzberg [7] showed how Chang's method could be modified to transmit complex-valued quadrature amplitude modulated (QAM) symbols. A half symbol space delay in time between the in-phase and quadrature components of the QAM symbols is inserted and it was shown that this allows perfect reconstruction of the data symbols. These methods also achieve the maximum bandwidth efficiency over the bandwidth the signal is being transmitted over. Polyphase structures for efficient implementation of the Saltzberg's method were later proposed in [8]. Due to the half symbol space delay between the in-phase and quadrature components, Saltzberg's method has been referred to as offset quadrature amplitude modulation (OQAM) or OFDM-OQAM. We refer to Chang's method as cosine modulated multitone (CMT), and Saltzberg's method as staggered modulated multitone (SMT).

Filtered multitone (FMT) is another multicarrier modulation techinque that was initially

developed for digital subscriber lines (DSL) [9]. In this method, adjacent subcarriers do not overlap unlike SMT and CMT. This allows FMT to be used to transmit normal QAM symbols without staggering, which makes it easily generalizable to multiple-input multiple-output (MIMO) systems but will result in losing some spectral efficiency.

In this chapter, we first present the transceivers of staggered modulated multitone (SMT) and cosine modulated multitone (CMT), which are two members of FBMC. The structures of the transmitter and receiver are discussed in Section 2.1. Timing and carrier frequency offset sensitivity analysis in SMT and CMT are presented in Sec. 2.2. Similarities and differences of SMT and CMT and the equivalence relationship between them are derived in Sec. 2.3.

2.1 SMT and CMT Transceiver

From [13], the continuous time structure of an SMT or CMT transceiver is shown in Fig. 2.1 and 2.2. The input signals $s_1(t)$ through $s_{N-1}(t)$ are continuous time signals obtained from the data symbols $s_1[n]$ through $s_{N-1}[n]$ with

$$s_k(t) = \sum_n s_k[n]\delta(t - nT).$$

In SMT, $s_k[n]$ are complex-valued data symbols such as QAM or PSK, while in CMT $s_k[n]$ are real-valued. Furthermore, in SMT, the real and imaginary parts of $s_k[n]$ are separated and time staggered by $T/2$. The signal is then filtered by the prototype filter $h(t)$ in SMT or $h(t)e^{j\frac{\pi}{2T}t}$ in CMT, and for each k, the kth stream signal is then multiplied by $e^{jk(\frac{2\pi}{T}t+\frac{\pi}{2})}$. The signals from each subcarrier are summed and modulated to the RF band to be transmitted.

At the receiver, the signal is first demodulated from the RF band to obtain the complex baseband signal. The kth stream signal is retrieved by a multiplication of $e^{-jk(\frac{2\pi}{T}t+\frac{\pi}{2})}$ and filtering by $h(t)$ in SMT or $h(t)e^{j\frac{\pi}{2T}t}$ in CMT. In SMT the time staggering will also need to be undone to extract the real and imaginary parts of the data symbols.

2.2 Sensitivity Analysis

In this section, we proceed with an analysis of performance loss of CMT and SMT that may result from channel impairments such as multipath, carrier frequency and/or timing phase offset and compare the two methods with these respects.

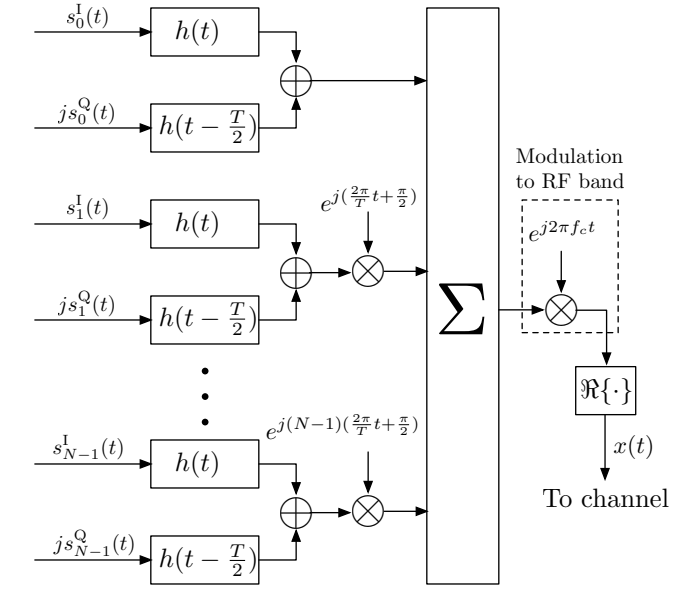

(a)

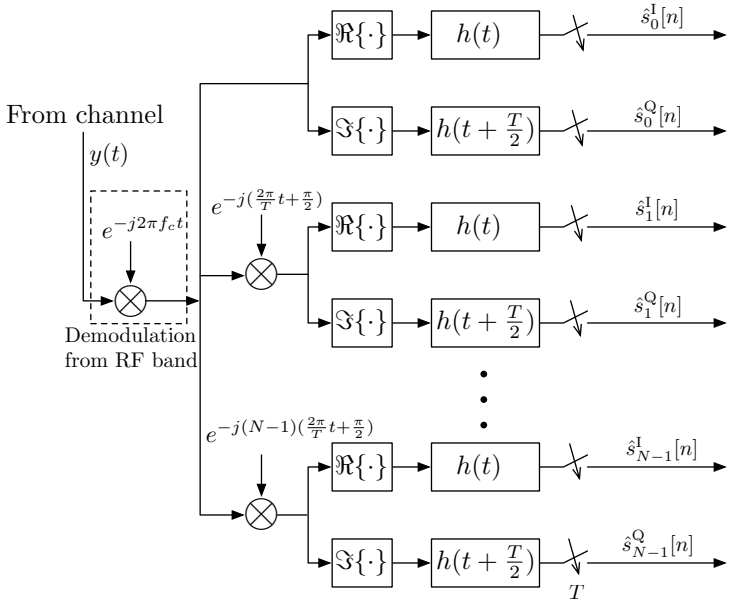

(b)

Figure 2.1: SMT transceiver system: (a) transmitter; (b) receiver.

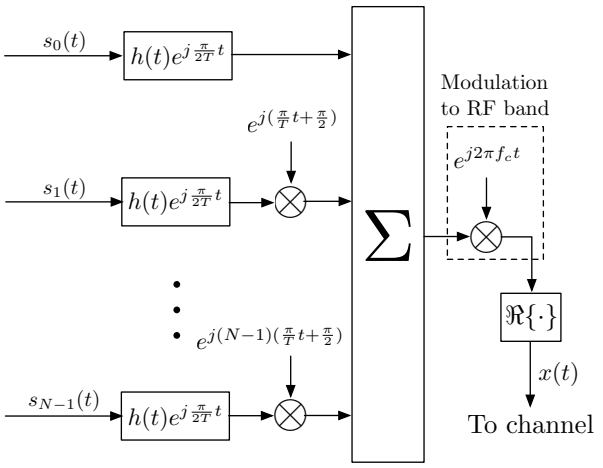

(a)

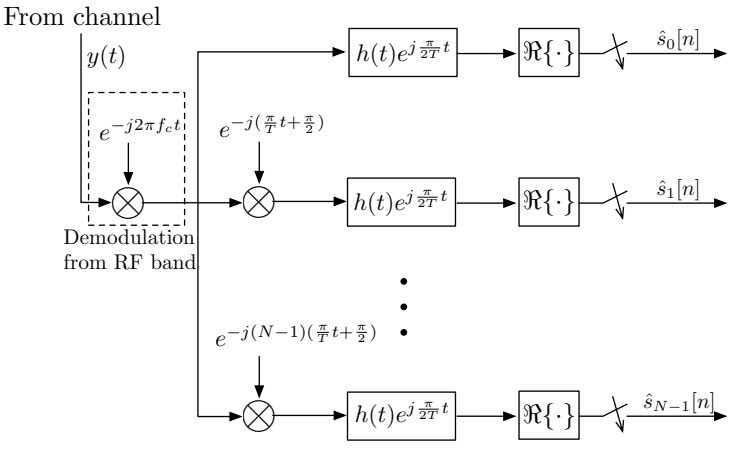

(b)

Figure 2.2: CMT transceiver system: (a) transmitter; (b) receiver.

2.2.1 CMT

Following Fig. 2.1, and assuming a frequency offset Δf_c between the transmitter and receiver carriers, one finds that the kth output of the receiver before the sampler is given by

$$\hat{s}_k(t) = \Re\left\{\frac{1}{C_k}\left((v(t)\star c(t))e^{j2\pi\Delta f_c t}e^{-jk(\frac{\pi}{T}t+\frac{\pi}{2})}\right)\star\left(h(t)e^{j\frac{\pi}{2T}t}\right)\right\} \tag{2.1}$$

where $v(t)$ is the output of the summer at the transmitter, $c(t)$ is the impulse response of the baseband equivalent of the passband channel, and we have approximated the channel over the kth subcarrier band by a flat gain C_k. Hence, the multiplier $\frac{1}{C_k}$ in (2.1) may be thought of as a single-tap equalizer. We also note that

$$\begin{aligned} v(t) &= \sum_{l=0}^{N-1}\sum_{n=-\infty}^{\infty} s_l[n]h(t-nT)e^{j\frac{\pi}{2T}(t-nT)}e^{jl(\frac{\pi}{T}t+\frac{\pi}{2})} \\ &= \sum_{l=0}^{N-1}\sum_{n=-\infty}^{\infty} (-j)^n s_l[n]h(t-nT)e^{j\frac{\pi}{2T}t}e^{jl(\frac{\pi}{T}t+\frac{\pi}{2})}. \end{aligned} \tag{2.2}$$

Substituting (2.2) into (2.1), we obtain

$$\begin{aligned} \hat{s}_k(t) = \Re\Bigg\{\frac{1}{C_k}\Bigg(\Bigg(\sum_{l=0}^{N-1}\sum_{n=-\infty}^{\infty}(-j)^n s_l[n]\left(h(t-nT)e^{j\frac{\pi}{2T}t}e^{jl(\frac{\pi}{T}t+\frac{\pi}{2})}\star c(t)\right)\Bigg) \\ e^{j2\pi\Delta f_c t}e^{-jk(\frac{\pi}{T}t+\frac{\pi}{2})}\Bigg)\star\left(h(t)e^{j\frac{\pi}{2T}t}\right)\Bigg\}. \end{aligned} \tag{2.3}$$

To simplify this result, we let $c_l(t) = c(t)e^{-j\frac{\pi}{2T}t}e^{-jl\frac{\pi}{T}t}$ or, equivalently, $c(t) = c_l(t)e^{j\frac{\pi}{2T}t}e^{jl\frac{\pi}{T}t}$ and note that

$$\begin{aligned} & h(t-nT)e^{j\frac{\pi}{2T}t}e^{jl(\frac{\pi}{T}t+\frac{\pi}{2})}\star c(t) \\ = \; & h(t-nT)e^{j\frac{\pi}{2T}t}e^{jl(\frac{\pi}{T}t+\frac{\pi}{2})}\star c_l(t)e^{j\frac{\pi}{2T}t}e^{jl\frac{\pi}{T}t} \\ = \; & \int_{-\infty}^{\infty} h(\tau-nT)e^{j\frac{\pi}{2T}\tau}e^{jl(\frac{\pi}{T}\tau+\frac{\pi}{2})}c_l(t-\tau)e^{j\frac{\pi}{2T}(t-\tau)}e^{jl\frac{\pi}{T}(t-\tau)}d\tau \\ = \; & g_l(t-nT)e^{j\frac{\pi}{2T}t}e^{jl(\frac{\pi}{T}t+\frac{\pi}{2})} \end{aligned} \tag{2.4}$$

where

$$g_l(t) = h(t)\star c_l(t). \tag{2.5}$$

Substituting (2.4) into (2.3) and rearranging the result, we obtain

$$\begin{aligned} & \hat{s}_k(t) \\ = \; & \Re\left\{\frac{1}{C_k}\left(\sum_{l=0}^{N-1}\sum_{n=-\infty}^{\infty}(-j)^n s_l[n]g_l(t-nT)e^{j(l-k)(\frac{\pi}{T}t+\frac{\pi}{2})}e^{j2\pi(\Delta f_c+\frac{1}{4T})t}\right)\star\left(h(t)e^{j\frac{\pi}{2T}t}\right)\right\}. \end{aligned} \tag{2.6}$$

Next, without any loss of generality, we concentrate on the detection $s_k[n]$, for $n = 0$. For this purpose, we note that $\hat{s}_k(t)$ may be expanded as

$$\hat{s}_k(t) = \hat{s}_k^0(t) + \hat{s}_k^{\mathrm{ISI}}(t) + \hat{s}_k^{\mathrm{ICI}}(t) \tag{2.7}$$

where

$$\hat{s}_k^0(t) = s_k[0]\Re\left\{g_k^k(t)\right\} \tag{2.8}$$

$$\hat{s}_k^{\mathrm{ISI}}(t) = \sum_{\substack{n=-\infty \\ n\neq 0}}^{\infty} s_k[n]\Re\left\{e^{j2\pi\Delta f_c nT} g_k^k(t-nT)\right\} \tag{2.9}$$

$$\hat{s}_k^{\mathrm{ICI}}(t) = \sum_{\substack{l=0 \\ l\neq k}}^{N-1} \sum_{n=-\infty}^{\infty} (-1)^{(l-k)n} s_l[n]\Re\left\{e^{j2\pi\Delta f_c nT} g_k^l(t-nT)\right\} \tag{2.10}$$

and

$$g_k^l(t) = \frac{1}{C_k} g_l(t) e^{j(l-k)(\frac{\pi}{T}t+\frac{\pi}{2})} e^{j2\pi(\Delta f_c + \frac{1}{4T})t} \star h(t) e^{j\frac{\pi}{2T}t}. \tag{2.11}$$

Under an ideal channel condition, i.e., when $c(t) = \delta(t)$, $\Delta f_c = 0$, and $h(t)$ is a properly designed pulse-shaping filter according to the Nyquist criteria, one finds that $\hat{s}_k^0(0) = s_k[0]$, and $\hat{s}_k^{\mathrm{ISI}}(0) = \hat{s}_k^{\mathrm{ICI}}(0) = 0$. That is, as one would expect, in the absence of channel impairments, ISI and ICI free detection is possible. Impairments in the channel, including timing phase error and carrier offset, result in ISI and ICI and, thus, some distortion in the detected symbols. These, collectively, may be quantified by evaluating the ratio of the desired symbol power over the ISI plus ICI power. For a timing phase error τ, this ratio is given by

$$\rho_{\mathrm{CMT}} = 10\log_{10} \frac{\left(\Re\left\{g_k^k(\tau)\right\}\right)^2}{\sum\limits_{\substack{n=-\infty \\ n\neq 0}}^{\infty} \left(\Re\left\{e^{j2\pi\Delta f_c nT} g_k^k(\tau-nT)\right\}\right)^2 + \sum\limits_{\substack{l=0 \\ l\neq k}}^{N-1} \sum\limits_{n=-\infty}^{\infty} \left(\Re\left\{e^{j2\pi\Delta f_c nT} g_k^l(\tau-nT)\right\}\right)^2}. \tag{2.12}$$

In practice, where Δf_c and τ are small, the terms in the denominator of (2.12), i.e., the ISI and ICI powers, are small. Under such conditions, a good approximation to the equalizer gain $\frac{1}{C_k}$ that results in minimum mean square error in the estimation of $s_k[0]$ is obtained by setting $g_k^k(\tau) = 1$ or, equivalently,

$$C_k = \left(g_k(t) e^{j2\pi(\Delta f_c + \frac{1}{4T})t} \star h(t) e^{j\frac{\pi}{2T}t}\right)_{t=\tau}. \tag{2.13}$$

2.2.2 SMT

Following the same line of derivations to those presented above, for the SMT, one finds that the kth output of the receiver before the sampler is given by

$$\hat{s}_k^{\mathrm{I}}(t) = \Re\left\{\frac{1}{C_k}\left((v(t)\star c(t))e^{j2\pi\Delta f_c t}e^{-jk(\frac{2\pi}{T}t+\frac{\pi}{2})}\right)\star h(t)\right\} \tag{2.14}$$

and

$$\hat{s}_k^{\mathrm{Q}}(t) = \Re\left\{\frac{1}{C_k}\left((v(t)\star c(t))e^{j2\pi\Delta f_c t}e^{-jk(\frac{2\pi}{T}t+\frac{\pi}{2})}\right)\star h\left(t+\frac{T}{2}\right)\right\} \tag{2.15}$$

where $c(t)$ is the impulse response of the baseband equivalent of the passband channel, and $v(t)$ is the output of the summer at the transmitter, which is given by

$$v(t) = \sum_{l=0}^{N-1}\sum_{n=-\infty}^{\infty}\left(s_l^{\mathrm{I}}[n]h(t-nT) + js_l^{\mathrm{Q}}[n]h\left(t-\frac{T}{2}-nT\right)\right)e^{jl(\frac{2\pi}{T}t+\frac{\pi}{2})}. \tag{2.16}$$

Here, we let $c_l(t) = c(t)e^{-jl\frac{2\pi}{T}t}$ or, equivalently, $c(t) = c_l(t)e^{jl\frac{2\pi}{T}t}$, and note that

$$\begin{aligned} h(t-nT)e^{jl(\frac{2\pi}{T}t+\frac{\pi}{2})}\star c(t) &= h(t-nT)e^{jl(\frac{2\pi}{T}t+\frac{\pi}{2})}\star c_l(t)e^{jl\frac{2\pi}{T}t} \\ &= \int_{-\infty}^{\infty} h(\tau-nT)e^{jl(\frac{2\pi}{T}\tau+\frac{\pi}{2})}c_l(t-\tau)e^{jl\frac{2\pi}{T}(t-\tau)}d\tau \\ &= g_l(t-nT)e^{jl(\frac{2\pi}{T}t+\frac{\pi}{2})} \end{aligned} \tag{2.17}$$

where

$$g_l(t) = h(t)\star c_l(t). \tag{2.18}$$

Moreover, one finds that

$$h\left(t-\frac{T}{2}-nT\right)e^{jl(\frac{2\pi}{T}t+\frac{\pi}{2})}\star c(t) = g_l(t-\frac{T}{2}-nT)e^{jl(\frac{2\pi}{T}t+\frac{\pi}{2})}. \tag{2.19}$$

Substituting (2.16) into (2.14) and (2.15), and using (2.17) and (2.19), we obtain

$$\begin{aligned} \hat{s}_k^{\mathrm{I}}(t) = \Re\Bigg\{\frac{1}{C_k}\Bigg(&\sum_{l=0}^{N-1}\sum_{n=-\infty}^{\infty}\left(s_l^{\mathrm{I}}[n]g_l(t-nT) + js_l^{\mathrm{Q}}[n]g_l\left(t-\frac{T}{2}-nT\right)\right) \\ &e^{j2\pi(\Delta f_c+\frac{l-k}{T})t}\Bigg)\star h(t)\Bigg\} \end{aligned} \tag{2.20}$$

and

$$\begin{aligned} \hat{s}_k^{\mathrm{Q}}(t) = \Re\Bigg\{\frac{1}{C_k}\Bigg(&\sum_{l=0}^{N-1}\sum_{n=-\infty}^{\infty}\left(s_l^{\mathrm{I}}[n]g_l(t-nT) + js_l^{\mathrm{Q}}[n]g_l\left(t-\frac{T}{2}-nT\right)\right) \\ &e^{j2\pi(\Delta f_c+\frac{l-k}{T})t}\Bigg)\star h\left(t+\frac{T}{2}\right)\Bigg\}. \end{aligned} \tag{2.21}$$

Next, without any loss of generality, we concentrate on the detection $s_k^{\mathrm{I}}[n]$, for $n = 0$. We note that $\hat{s}_k^{\mathrm{I}}(t)$ may be expanded as

$$\hat{s}_k^{\mathrm{I}}(t) = \hat{s}_k^{0,\mathrm{I}}(t) + \hat{s}_k^{\mathrm{ISI,I}}(t) + \hat{s}_k^{\mathrm{ICI,I}}(t) \tag{2.22}$$

where

$$\hat{s}_k^{0,\mathrm{I}}(t) = s_k^{\mathrm{I}}[0]\Re\left\{g_k^{k,\mathrm{II}}(t)\right\} \tag{2.23}$$

$$\begin{aligned}\hat{s}_k^{\mathrm{ISI,I}}(t) &= \sum_{\substack{n=-\infty \\ n\neq 0}}^{\infty} s_k^{\mathrm{I}}[n]\Re\left\{e^{j2\pi\Delta f_c nT} g_k^{k,\mathrm{II}}(t-nT)\right\} \\ &\quad + \sum_{n=-\infty}^{\infty} s_k^{\mathrm{Q}}[n]\Re\left\{je^{j2\pi\Delta f_c nT} g_k^{k,\mathrm{QI}}(t-nT)\right\}\end{aligned} \tag{2.24}$$

$$\begin{aligned}\hat{s}_k^{\mathrm{ICI,I}}(t) &= \sum_{\substack{l=0 \\ l\neq k}}^{N-1} \sum_{n=-\infty}^{\infty} (-1)^{(l-k)n} \left(s_l^{\mathrm{I}}[n]\Re\left\{e^{j2\pi\Delta f_c nT} g_k^{l,\mathrm{II}}(t-nT)\right\}\right. \\ &\quad \left. + s_l^{\mathrm{Q}}[n]\Re\left\{je^{j2\pi\Delta f_c nT} g_k^{k,\mathrm{QI}}(t-nT)\right\}\right)\end{aligned} \tag{2.25}$$

with

$$g_k^{l,\mathrm{II}}(t) = \frac{1}{C_k} g_l(t) e^{j(l-k)(\frac{2\pi}{T}t+\frac{\pi}{2})} e^{j2\pi\Delta f_c t} \star h(t) \tag{2.26}$$

$$g_k^{l,\mathrm{QI}}(t) = \frac{1}{C_k} g_l(t-\frac{T}{2}) e^{j(l-k)(\frac{2\pi}{T}t+\frac{\pi}{2})} e^{j2\pi\Delta f_c t} \star h(t). \tag{2.27}$$

In the above equations $g_k^{l,\mathrm{II}}(t)$ is the impulse response between the lth in-phase input to the k in-phase output, and $g_k^{l,\mathrm{QI}}(t)$ is the impulse response between the lth quadrature input to the k in-phase output, before taking the real part at the output.

We can now evaluate the ratio of the desired symbol power over the ISI plus ICI power. For a timing phase error τ, this ratio is given by

$$\rho_{\mathrm{SMT}} = 10\log_{10}\frac{|g_k^{k,\mathrm{II}}(\tau)|^2}{A} \tag{2.28}$$

where

$$\begin{aligned}A &= \sum_{\substack{n=-\infty \\ n\neq 0}}^{\infty} \left|\Re\left\{e^{j2\pi\Delta f_c nT} g_k^{k,\mathrm{II}}(t-nT)\right\}\right|^2 + \sum_{n=-\infty}^{\infty} \left|\Re\left\{je^{j2\pi\Delta f_c nT} g_k^{k,\mathrm{QI}}(t-nT)\right\}\right|^2 \\ &\quad + \sum_{\substack{l=0 \\ l\neq k}}^{N-1} \sum_{n=-\infty}^{\infty} \left(\left|\Re\left\{e^{j2\pi\Delta f_c nT} g_k^{l,\mathrm{II}}(t-nT)\right\}\right|^2 + \left|\Re\left\{je^{j2\pi\Delta f_c nT} g_k^{l,\mathrm{QI}}(t-nT)\right\}\right|^2\right).\end{aligned} \tag{2.29}$$

We also note that as in the case of CMT, here also, when Δf_c and τ are small, the terms on the right-hand side of (2.29) are small, a good approximation to the equalizer gain $\frac{1}{C_k}$

that results in minimum mean square error in the estimation of $s_k^{\mathrm{I}}[0]$ is obtained by setting $g_k^{k,\mathrm{II}}(\tau) = 1$ or, equivalently,

$$C_k = \left(g_k(t) e^{j2\pi\Delta f_c t} \star h(t) \right)_{t=\tau}. \tag{2.30}$$

Note that in the above equations, we have concentrated on the in-phase component of $s_k[n]$. Because of the symmetry of the in-phase and quadrature components in a QAM system (including staggered QAM/SMT), similar equations are obtained if one explores the interference received on the quadrature component of $s_k[n]$. Using MATLAB, we implement the equations and observe the effect of carrier frequency or timing phase offset on $\hat{s}_l(t)$ at t=0. We plot ρ_{CMT} and ρ_{SMT} against different values of carrier frequency offset Δf_c and timing phase offset τ. Fig. 2.3, 2.4, 2.5, and 2.6 show the results.

2.2.3 Mathematical Comparison of ρ_{CMT} and ρ_{SMT}

In this section, the values of ρ_{CMT} and ρ_{SMT} are evaluated for the case where channel is ideal but with carrier frequency offset Δf_c and timing phase offset τ. The finding is that when subcarrier spacing in both CMT and SMT is the same, $\rho_{\mathrm{CMT}} = \rho_{\mathrm{SMT}}$, i.e., the two methods are equally sensitive to timing offset and carrier frequency offset. However, ρ_{CMT} and ρ_{SMT} deviate in presence of the channel. Nevertheless, this deviation remains negligible as long as a flat gain approximation over each subcarrier channel can be assumed. This interesting result has been confirmed numerically in [10].

For a fair comparison, while we use T to represent the symbol interval in the case of SMT, T is replaced by $T/2$ in the case of CMT.

In CMT, when the channel is ideal, $c_l(t) = c(t) = \delta(t)$ and it follows from (2.5) that $g_l(t) = h(t)$. Substituting this result, and also T by $T/2$, (2.8), (2.9) and (2.10), respectively, reduce to

$$\begin{aligned} \hat{s}_k^0(t) &= s_k[0] c_k^0(t) \\ &\quad \text{with } c_k^0(t) = \Re\left\{ \frac{1}{C_k} q(t) \right\} \end{aligned} \tag{2.31}$$

where $q(t) = h(t) e^{j\frac{\pi}{T}t} e^{j2\pi\Delta f_c t} \star h(t) e^{j\frac{\pi}{T}t} = p(t) e^{j\frac{\pi}{T}t}$ and $p(t) = h(t) e^{j2\pi\Delta f_c t} \star h(t)$,

$$\begin{aligned} \hat{s}_k^{\mathrm{ISI}}(t) &= \sum_{\substack{n=-\infty \\ n\neq 0}}^{\infty} s_k[n] c_k^{\mathrm{ISI}}(t) \\ &\quad \text{with } c_k^{\mathrm{ISI}}(t) = \Re\left\{ \frac{1}{C_k} h(t - nT/2) e^{j\frac{\pi}{T}(t-nT/2)} e^{j2\pi\Delta f_c t} \star h(t) e^{j\frac{\pi}{T}t} \right\}, \end{aligned} \tag{2.32}$$

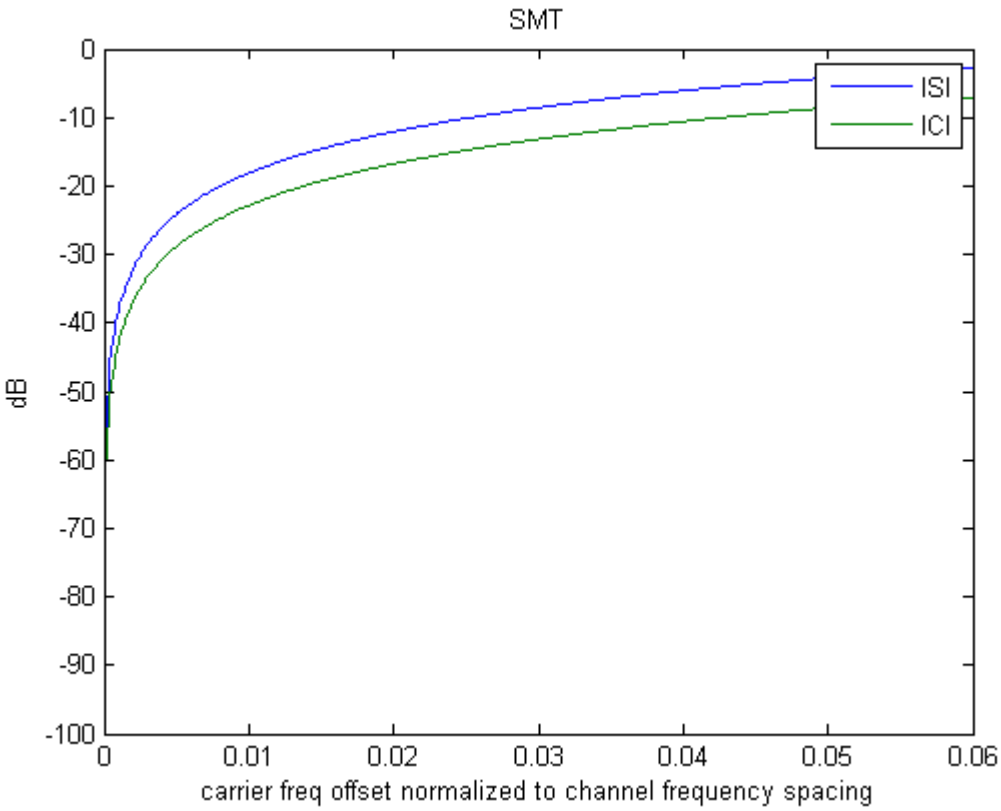

Figure 2.3: SMT carrier frequency offset analysis.

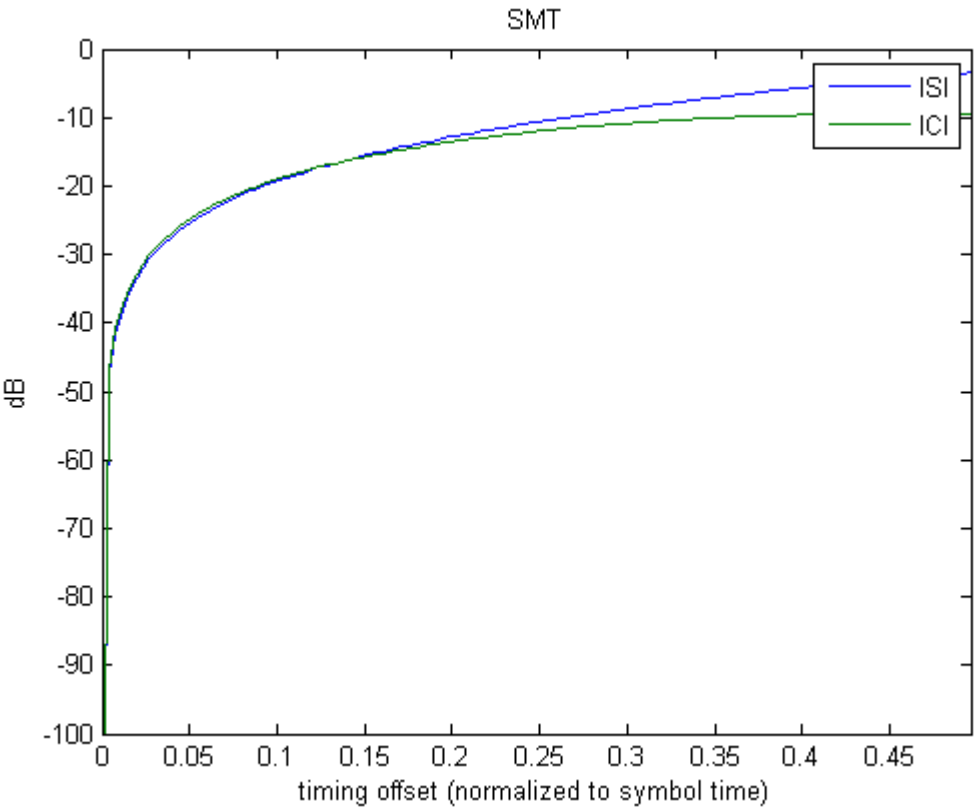

Figure 2.4: SMT timing offset analysis.

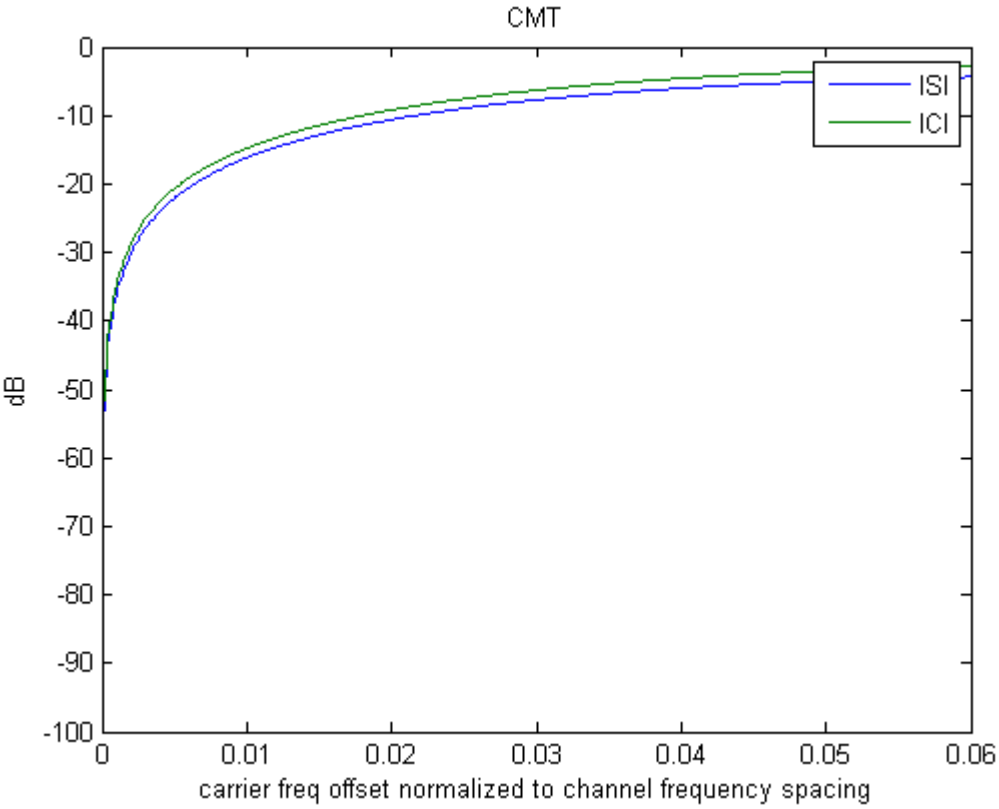

Figure 2.5: CMT carrier frequency offset analysis.

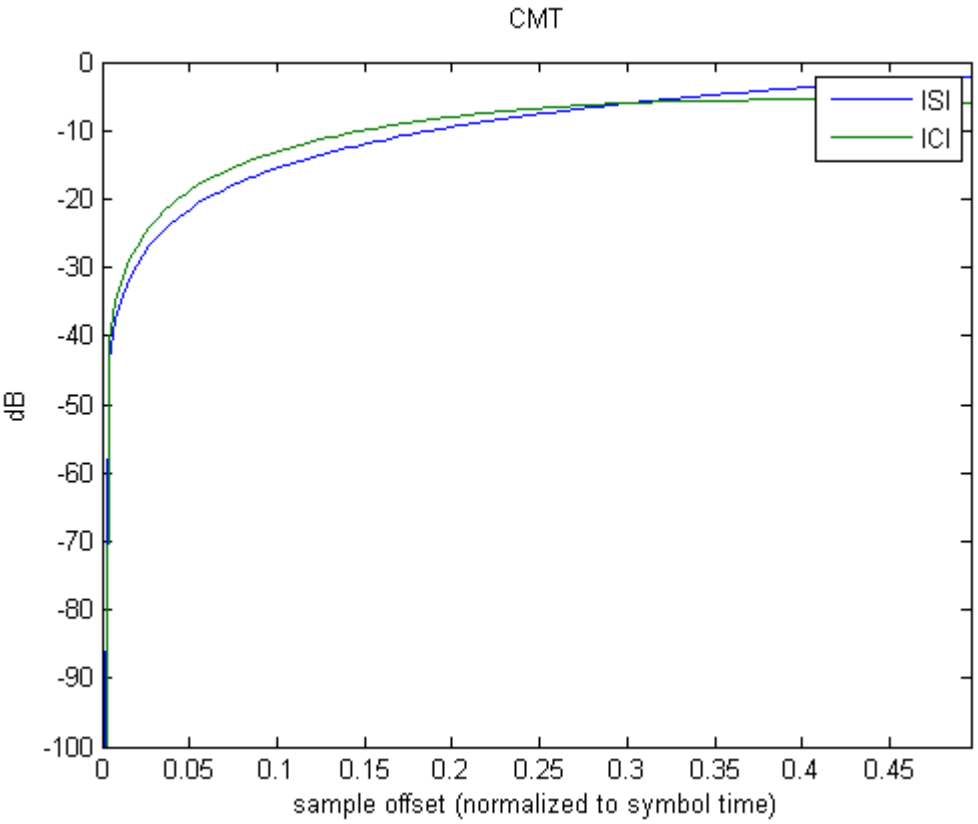

Figure 2.6: CMT timing offset analysis.

and

$$\hat{s}_k^{\mathrm{ICI}}(t) = \sum_{\substack{l=0 \\ l\neq k}}^{N-1} \sum_{n=-\infty}^{\infty} s_l[n] c_l^{\mathrm{ICI}}(t) \tag{2.33}$$

$$\text{with} \qquad c_l^{\mathrm{ICI}}(t) = \Re\left\{ \frac{1}{C_k} h(t-nT/2) e^{j\frac{\pi}{T}(t-nT/2)} e^{j(l-k)(\frac{2\pi}{T}t+\frac{\pi}{2})} e^{j2\pi\Delta f_c t} \star h(t) e^{j\frac{\pi}{T}t} \right\}.$$

We note the impulse response between $s_k[0]$ and the analyzed signal before equalization is $q(t)$. This, in turn, implies, for a timing phase τ, the channel gain between $s_k[0]$ and the analyzed signal before equalization is $q(\tau)$. Hence, to equalize the channel one should choose $C_k = q(\tau) = p(\tau)e^{j\frac{\pi}{T}\tau}$. Substituting this choice of C_k in (2.31), 2.43) and (2.33), we obtain

$$\hat{s}_k^0(\tau) = s_k[0] \tag{2.34}$$

$$\hat{s}_k^{\mathrm{ISI}}(\tau) = \sum_{\substack{n=-\infty \\ n\neq 0}}^{\infty} s_k[n] c_k^{\mathrm{ISI}}(\tau) \tag{2.35}$$

$$\hat{s}_k^{\mathrm{ICI}}(\tau) = \sum_{\substack{l=0 \\ l\neq k}}^{N-1} \sum_{n=-\infty}^{\infty} s_l[n] c_l^{\mathrm{ICI}}(\tau) \tag{2.36}$$

where

$$\begin{aligned} c_k^{\mathrm{ISI}}(\tau) &= \Re\left\{ \frac{e^{j2\pi\Delta f_c nT/2} q(\tau - nT/2)}{q(\tau)} \right\} \\ &= \Re\left\{ \frac{e^{j2\pi\Delta f_c nT/2} (-j)^n p(\tau - nT/2)}{p(\tau)} \right\} \\ &= \begin{cases} \Re\left\{ (-1)^m \dfrac{e^{j2\pi\Delta f_c mT/2} p(\tau - mT)}{p(\tau)} \right\} & n = 2m \text{ (even)} \\ \Re\left\{ j(-1)^{m+1} \dfrac{e^{j2\pi\Delta f_c (mT+T/2)} p(\tau - T/2 - mT)}{p(\tau)} \right\}, & n = 2m+1 \text{ (odd)} \end{cases} \end{aligned} \tag{2.37}$$

and

$$
\begin{aligned}
&c_l^{\mathrm{ICI}}(\tau) \\
&\quad = \Re\left\{\frac{e^{j2\pi\Delta f_c nT/2}(-1)^{(l-k)n} r_{l,k}(\tau - nT/2)}{q(\tau)}\right\} \\
&\quad = \Re\left\{\frac{e^{j2\pi\Delta f_c nT/2}(-1)^{(l-k)n}(-j)^n u_{l,k}(\tau - nT/2)}{p(\tau)}\right\} \\
&\quad = \begin{cases} \Re\left\{\dfrac{(-1)^m e^{j2\pi\Delta f_c mT} u_{l,k}(\tau - mT)}{p(\tau)}\right\} & n = 2m \text{ (even)} \\ \Re\left\{\dfrac{j(-1)^{l-k+m+1} e^{j2\pi\Delta f_c(mT+T/2)} u_{l,k}(\tau - T/2 - mT)}{p(\tau)}\right\}, & n = 2m+1 \text{ (odd)} \end{cases}
\end{aligned} \tag{2.38}
$$

where

$$
r_{l,k}(t) = h(t)e^{j\frac{\pi}{T}t} e^{j(l-k)(\frac{2\pi}{T}t+\frac{\pi}{2})} e^{j2\pi\Delta f_c t} \star h(t)e^{j\frac{\pi}{T}t} = u_{l,k}(t)e^{j\frac{\pi}{T}t} \tag{2.39}
$$

and

$$
u_{l,k}(t) = h(t)e^{j(l-k)(\frac{2\pi}{T}t+\frac{\pi}{2})} e^{j2\pi\Delta f_c t} \star h(t). \tag{2.40}
$$

Then the ratio ρ_{CMT} from (2.12) can be simplified into

$$
\rho_{\mathrm{CMT}} = 10\log_{10}\frac{1}{B}
$$

where

$$
\begin{aligned}
B \;=\; & \sum_{\substack{m=-\infty \\ m\neq 0}}^{\infty} \left(\Re\left\{\frac{e^{j2\pi\Delta f_c mT} p(\tau - mT)}{p(\tau)}\right\}\right)^2 \\
& + \sum_{m=-\infty}^{\infty} \left(\Re\left\{\frac{j e^{j2\pi\Delta f_c(mT+T/2)} p(\tau - T/2 - mT)}{p(\tau)}\right\}\right)^2 \\
& + \sum_{\substack{l=0 \\ l\neq k}}^{N-1} \sum_{m=-\infty}^{\infty} \left(\Re\left\{\frac{e^{j2\pi\Delta f_c mT} u_{l,k}(\tau - mT)}{p(\tau)}\right\}\right)^2 \\
& + \sum_{\substack{l=0 \\ l\neq k}}^{N-1} \sum_{m=-\infty}^{\infty} \left(\Re\left\{\frac{j e^{j2\pi\Delta f_c(mT+T/2)} u_{l,k}(\tau - T/2 - mT)}{p(\tau)}\right\}\right)^2.
\end{aligned} \tag{2.41}
$$

Similarly, in SMT, with $c_l(t) = c(t) = \delta(t)$, it follows from (2.18) that $g_l(t) = h(t)$. Substituting this result and $\Delta f_c = 0$, (2.23), (2.24) and (2.25), respectively, reduce to

$$
\begin{aligned}
\hat{s}_k^{0,\mathrm{I}}(t) \;=\; & s_k^{\mathrm{I}}[0] c_k^{0,\mathrm{I}}(t) \\
& \text{with } c_k^{0,\mathrm{I}}(t) = \Re\left\{\frac{1}{C_k} p(t)\right\} \\
& \text{and } p(t) = h(t)e^{j2\pi\Delta f_c t} \star h(t),
\end{aligned} \tag{2.42}
$$

$$\hat{s}_k^{\mathrm{ISI,I}}(t) = \sum_{\substack{n=-\infty \\ n\neq 0}}^{\infty} s_k^{\mathrm{I}}[n] c_k^{\mathrm{ISI,II}}(t) + \sum_{n=-\infty}^{\infty} s_k^{\mathrm{Q}}[n] c_k^{\mathrm{ISI,QI}}(t) \tag{2.43}$$

$$\text{with } c_k^{\mathrm{ISI,II}}(t) = \Re\left\{ \frac{1}{C_k} h(t-nT) e^{j2\pi\Delta f_c t} \star h(t) \right\}$$

$$\text{and } c_k^{\mathrm{ISI,QI}}(t) = \Re\left\{ \frac{1}{C_k} j h(t-T/2-nT) e^{j2\pi\Delta f_c t} \star h(t) \right\},$$

and

$$\hat{s}_k^{\mathrm{ICI,I}}(t) = \sum_{\substack{l=0 \\ l\neq k}}^{N-1} \sum_{n=-\infty}^{\infty} s_l^{\mathrm{I}}[n] c_l^{\mathrm{ICI,II}}(t) + s_l^{\mathrm{Q}}[n] c_l^{\mathrm{ICI,QI}}(t) \tag{2.44}$$

$$\text{with } c_l^{\mathrm{ICI,II}}(t) = \Re\left\{ \frac{1}{C_k} h(t-nT) e^{j(l-k)(\frac{2\pi}{T}t+\frac{\pi}{2})} e^{j2\pi\Delta f_c t} \star h(t) \right\}$$

$$\text{and } c_l^{\mathrm{ICI,QI}}(t) = \Re\left\{ \frac{1}{C_k} j h(t-T/2-nT) e^{j(l-k)(\frac{2\pi}{T}t+\frac{\pi}{2})} e^{j2\pi\Delta f_c t} \star h(t) \right\}.$$

To equalize the channel we should choose $C_k = p(\tau)$. Applying this, the above results reduce to

$$\hat{s}_k^{0,\mathrm{I}}(\tau) = s_k^{\mathrm{I}}[0] \tag{2.45}$$

$$\hat{s}_k^{\mathrm{ISI,I}}(\tau) = \sum_{\substack{n=-\infty \\ n\neq 0}}^{\infty} s_k^{\mathrm{I}}[n] c_k^{\mathrm{ISI,II}}(\tau) + \sum_{n=-\infty}^{\infty} s_k^{\mathrm{Q}}[n] c_k^{\mathrm{ISI,QI}}(\tau) \tag{2.46}$$

$$\hat{s}_k^{\mathrm{ICI,I}}(\tau) = \sum_{\substack{l=0 \\ l\neq k}}^{N-1} \sum_{n=-\infty}^{\infty} s_l^{\mathrm{I}}[n] c_l^{\mathrm{ICI,II}}(\tau) + s_l^{\mathrm{Q}}[n] c_l^{\mathrm{ICI,QI}}(\tau) \tag{2.47}$$

where

$$c_k^{\mathrm{ISI,II}}(\tau) = \Re\left\{ \frac{e^{j2\pi\Delta f_c nT} p(\tau-nT)}{p(\tau)} \right\},$$

$$c_k^{\mathrm{ISI,QI}}(\tau) = \Re\left\{ \frac{j e^{j2\pi\Delta f_c (nT+T/2)} p(\tau-T/2-nT)}{p(\tau)} \right\},$$

$$c_l^{\mathrm{ICI,II}}(\tau) = \Re\left\{ \frac{e^{j2\pi\Delta f_c nT} u_{l,k}(\tau-nT)}{p(\tau)} \right\},$$

and

$$c_l^{\mathrm{ICI,QI}}(\tau) = \Re\left\{ \frac{j(-1)^{l-k} e^{j2\pi\Delta f_c (nT+T/2)} u_{l,k}(\tau-T/2-nT)}{p(\tau)} \right\}.$$

Then the ratio ρ_{SMT} from (2.28) can be simplified into

$$\rho_{\mathrm{SMT}} = 10 \log_{10} \frac{1}{C} \tag{2.48}$$

where

$$
\begin{aligned}
C &= \sum_{\substack{n=-\infty \\ n\neq 0}}^{\infty} \left(\Re \left\{ \frac{e^{j2\pi\Delta f_c nT} p(\tau - nT)}{p(\tau)} \right\} \right)^2 \\
&\quad + \sum_{n=-\infty}^{\infty} \left(\Re \left\{ \frac{j e^{j2\pi\Delta f_c (nT+T/2)} p(\tau - T/2 - nT)}{p(\tau)} \right\} \right)^2 \\
&\quad + \sum_{\substack{l=0 \\ l\neq k}}^{N-1} \sum_{n=-\infty}^{\infty} \left(\Re \left\{ \frac{e^{j2\pi\Delta f_c nT} u_{l,k}(\tau - nT)}{p(\tau)} \right\} \right)^2 \\
&\quad + \sum_{\substack{l=0 \\ l\neq k}}^{N-1} \sum_{n=-\infty}^{\infty} \left(\Re \left\{ \frac{j e^{j2\pi\Delta f_c (nT+T/2)} u_{l,k}(\tau - T/2 - nT)}{p(\tau)} \right\} \right)^2 . \qquad (2.49)
\end{aligned}
$$

Comparing (2.41) and (2.49), one finds that $B = C$, thus, $\rho_{\text{CMT}} = \rho_{\text{SMT}}$, for any τ and Δf_c.

2.3 Similarities and Differences of SMT and CMT

The advantage of FBMC systems over OFDMA systems is the lower stopband attenuation, which allows better ICI cancellation. Besides the above analytical development, this dissertation has studied the similarities and differences of CMT and SMT. The key point which results in ICI cancellation among adjacent subcarrier channels in both CMT and SMT is the fact that the same prototype filter $h(t)$ is used at both the transmitter and receiver sides. It is interesting to note that ICI cancellation among adjacent subcarrier channels does not impose any other restriction on the choice of $h(t)$. The condition that $p(t) = h(t) \star h(t)$ be a Nyquist pulse, thus, $h(t)$ should be an even symmetric square-root Nyquist filter, is imposed to avoid ISI. Moreover, $h(t)$ was chosen to be band-limited to minimize ICI among nonadjacent subcarrier channels. Also, for CMT, the even symmetry constraint of $h(t)$ can be relaxed, if the phase response of $H(f)$, the frequency domain of $h(t)$, satisfies an additional odd symmetry condition with respect to the midpoint of its transition band. It is straightforward to follow the same line of argument and show that the same is true in the case of SMT. Therefore, the fundamental concepts based on which both CMT and SMT have been developed are the same. The main difference between CMT and SMT is the modulation type. In SMT, data symbols are QAM and, thus, the modulation is double side-band (DSB). In CMT, on the other hand, data symbols are PAM and, thus, in order to keep the same bandwidth efficiency, vestigial side-band (VSB) modulation is used. Moreover, if we assume that each DSB subcarrier channel in SMT has the same width

as a VSB subcarrier channel in CMT, one finds that the symbol rate in each subcarrier channel of CMT will be double that of SMT. Next, we proceed to put these observations in a mathematical formulation.

The complex baseband signal for SMT before modulation to RF band is given by

$$v_{\mathrm{SMT}}(t) = \sum_{l=0}^{N-1} \sum_{n=-\infty}^{\infty} \left(s_l^{\mathrm{I}}[n] h(t-nT) + j s_l^{\mathrm{Q}}[n] h\left(t - \frac{T}{2} - nT\right)\right) e^{jl(\frac{2\pi}{T}t + \frac{\pi}{2})}. \tag{2.50}$$

On the other hand, the complex baseband signal for CMT (with T replaced by $T/2$ to equalize the subcarrier bandwidth of CMT with SMT) before modulation to RF band is given by

$$v_{\mathrm{CMT}}(t) = \sum_{l=0}^{N-1} \sum_{n=-\infty}^{\infty} s_l[n] h(t - nT/2) e^{j\frac{\pi}{T}(t-nT/2)} e^{jl(\frac{2\pi}{T}t + \frac{\pi}{2})}. \tag{2.51}$$

Separating the even and odd terms in $v_{CMT}(t)$, we can obtain

$$\begin{aligned}
v_{\mathrm{CMT}}(t) &= \sum_{l=0}^{N-1} \sum_{n=-\infty}^{\infty} s_l[n] h(t - nT/2) e^{j\frac{\pi}{T}(t-nT/2)} e^{jl(\frac{2\pi}{T}t + \frac{\pi}{2})} \\
&= \sum_{l=0}^{N-1} \sum_{n=-\infty}^{\infty} (-j)^n s_l[n] h(t - nT/2) e^{j\frac{\pi}{T}t} e^{jl(\frac{2\pi}{T}t + \frac{\pi}{2})} \\
&= \sum_{l=0}^{N-1} \sum_{k=-\infty}^{\infty} (-j)^{2k} s_l[2k] h(t - (2k)T/2) e^{j\frac{\pi}{T}t} e^{jl(\frac{2\pi}{T}t + \frac{\pi}{2})} \\
&\quad + \sum_{l=0}^{N-1} \sum_{k=-\infty}^{\infty} (-j)^{2k+1} s_l[2k+1] h(t - (2k+1)T/2) e^{j\frac{\pi}{T}t} e^{jl(\frac{2\pi}{T}t + \frac{\pi}{2})} \\
&= \sum_{l=0}^{N-1} \sum_{k=-\infty}^{\infty} (-1)^k s_l[2k] h(t - kT) e^{j\frac{\pi}{T}t} e^{jl(\frac{2\pi}{T}t + \frac{\pi}{2})} \\
&\quad + \sum_{l=0}^{N-1} \sum_{k=-\infty}^{\infty} j(-1)^{k+1} s_l[2k+1] h\left(t - \frac{T}{2} - kT\right) e^{j\frac{\pi}{T}t} e^{jl(\frac{2\pi}{T}t + \frac{\pi}{2})} \\
&= \sum_{l=0}^{N-1} \sum_{k=-\infty}^{\infty} \Big((-1)^k s_l[2k] h(t - kT) \\
&\qquad + j(-1)^{k+1} s_l[2k+1] h\left(t - \frac{T}{2} - kT\right)\Big) e^{j\frac{\pi}{T}t} e^{jl(\frac{2\pi}{T}t + \frac{\pi}{2})}.
\end{aligned} \tag{2.52}$$

Now, if we remap the bits such that $s_l^{\mathrm{I}}[n] = (-1)^k s_l[2k]$ and $s_l^{\mathrm{Q}}[n] = (-1)^{k+1} s_l[2k+1]$, we find that

$$v_{\mathrm{CMT}}(t) = v_{\mathrm{SMT}}(t) e^{j\frac{\pi}{T}t}. \tag{2.53}$$

Applying Fourier transform to both sides of (2.53), we obtain

$$V_{\mathrm{CMT}}(f) = V_{\mathrm{SMT}}\left(f - \frac{1}{4T}\right). \tag{2.54}$$

These results show that there is a simple relationship between CMT and SMT. The complex-valued baseband signal $v_{\mathrm{CMT}}(t)$ can be constructed by first synthesizing the corresponding $v_{\mathrm{SMT}}(t)$ signal and then modulating the results with the complex-valued sine-wave $e^{j\frac{\pi}{T}t}$. Alternatively, one may start with synthesizing a respective $v_{\mathrm{CMT}}(t)$ signal and modulate the result with $e^{-j\frac{\pi}{T}t}$ to obtain a desired $v_{\mathrm{SMT}}(t)$ baseband signal. These also apply to the respective analysis filter banks. This observation has the following implications:

- SMT and CMT are equally sensitive to channel impairments, including time and frequency spread, carrier frequency offset and timing offset. Therefore any analysis done for one is applicable to the other.

- A few structures have been proposed for efficient implementation of SMT (often referred to as OFDM- OQAM) [11], [12]. These structures, with minor modifications, are readily applicable to CMT.

CHAPTER 3

EXTENSION OF SC-FDMA TO FILTERBANK MULTICARRIER SYSTEMS

The third generation partnership project (3GPP) long-term evolution (LTE) radio standard has adopted a special form of orthogonal frequency division multiplexing (OFDM) method for the uplink of multiple access networks. This method, which is called single carrier frequency division multiple access (SC-FDMA), applies a precoding to each user data set in each OFDM symbol to control its peak-to-average power ratio (PAPR). In this chapter, we present a novel formulation of the SC-FDMA and explore possible mimicking of the same method when filter bank multicarrier (FBMC) is used for transmission. We find that such direct application of SC-FDMA to FBMC systems is not successful. However, we show that FBMC techniques offer other opportunities that when used correctly lead to a significant reduction in PAPR.

Reducing the PAPR in any transmission system is always desirable as it allows use of more power efficient and cheaper amplifiers at the transmitter. The 3GPP LTE radio standard has adopted SC-FDMA, a special form of OFDM signaling, for the uplink of multiple access networks. SC-FDMA applies a precoding to each user data set in each OFDM symbol to control PAPR, [14, 15, 16]. The standard has recognized this as a critical component to the success of 3GPP LTE products, noting that reducing PAPR directly translates to a lower power consumption and thus a longer battery life of mobile stations.

3.1 Single Carrier Frequency Division Multiple Access System

The basic principle of SC-FDMA, in the form adopted in the 3GPP LTE standard (i.e., when a set of contiguous subcarriers is allocated to each user), are laid out in [27]. Fig. 3.1 presents a block diagram of such a SC-FDMA transmitter. A user data stream $s[n]$ is passed through a multiplexer (a serial-to-parallel converter (S/P)) that divides it into M

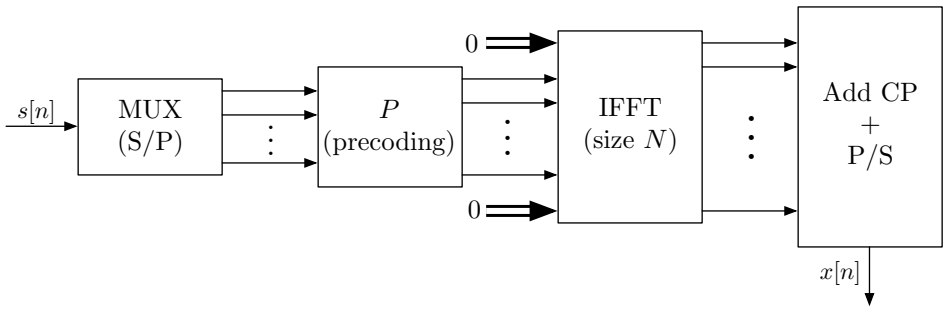

Figure 3.1: An SC-FDMA transmitter.

parallel substreams. In a conventional OFDMA, these substreams are directly allocated to M subcarriers in an OFDM modulator with a total of $N > M$ subcarriers. In SC-FDMA, a precoder is inserted between the multiplexer and OFDM modulator. The precoder takes the M output samples of multiplexer and premultiplies them with a matrix P of size $L \times M$, where $L \geq M$. The choice of $L > M$ allows addition of some redundancy that are used to further reduce PAPR. It has been noted in [27] that when $L = M$, a good choice of P is the DFT matrix, and when $L > M$, P is obtained by extending the $M \times M$ DFT matrix vertically and premultiplying the resulting $L \times M$ matrix with a diagonal matrix whose diagonal elements form a proper window function. The raised-cosine and square-root raised-cosine window functions have been suggested in [27].

To develop a more in depth understanding of the SC-FDMA, we note that the SC-FDMA transmitter is a multirate digital signal processing system with the data sequence $s[n]$ at its input and the synthesized signal $x[n]$ at its output. Fig. 3.2 casts this multirate system in a form that will allow its manipulation using the standard multirate signal processing tools. Here, the multiplexer is implemented using a tapped delay line of length M and a set of M-fold decimators. $\mathbf{P}$ is the precoder matrix, of size $L \times M$. $\mathbf{E}$ takes the precoder output of length L and expands it to the length N, by appending zeros to its beginning and its end. The precoded and expanded samples are passed to an inverse fast Fourier transform (IFFT) block denoted by $\boldsymbol{\mathcal{F}}^{-1}$. The parallel-to-serial (P/S) block of the structure is implemented using a set of N-fold expanders, followed by a set of shift and add operations. The cyclic prefix (CP) samples are added at the end.

Using the standard tools from multirate signal processing, [20, 13], the structure presented in Fig. 3.2 may be converted to Fig. 3.3.

The transfer function between the single input $s[n]$ and multiple outputs $x_0[n]$ through $x_{N-1}[n]$ is thus obtain as

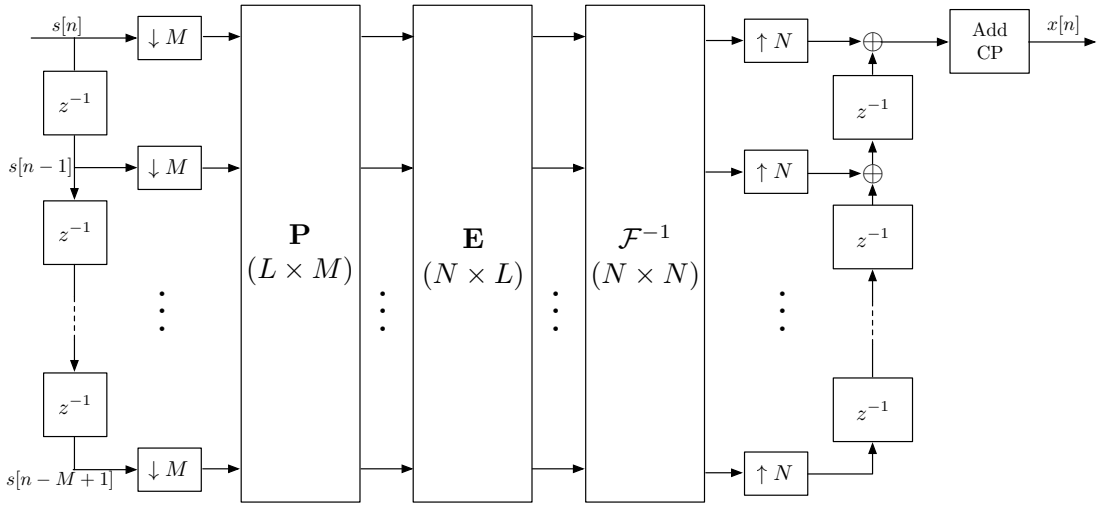

Figure 3.2: The SC-FDMA transmitter of Fig. 3.1 implemented using the standard multirate signal processing blocks.

$$\mathbf{H}(z) = \frac{\mathbf{X}(z)}{S(z)} = \mathbf{G}\mathbf{z} \tag{3.1}$$

where $\mathbf{G} = \boldsymbol{\mathcal{F}}^{-1}\mathbf{E}\mathbf{P}$ and $\mathbf{z}$ is a tapped delay line vector of compatible length. Here,

$$\mathbf{z} = \begin{bmatrix} 1 & z^{-1} & \cdots & z^{-(M-1)} \end{bmatrix}^{\mathrm{T}} \tag{3.2}$$

where the superscript T denotes matrix or vector transpose. Alternatively, one may note that the vector of impulse response between the input $s[n]$ and the kth output $x_k[n]$ is the kth row of $\mathbf{G}$.

Each decimator selects one out of every M samples of each of the sequences $x_0[n]$ through $x_{N-1}[n]$, and the expanders followed by the shift and add blocks effectively construct a P/S that sequentially sends the selected samples to the transmitter output. Accordingly, the PAPR of the SC-FDMA transmitter may be calculated as

$$\mathrm{PAPR} = \frac{\max\limits_{k,n} |x_k[n]|^2}{\mathrm{avg}[|x_k[n]|^2]} \tag{3.3}$$

where $\mathrm{avg}[|x_k[n]|^2]$ is the average of $|x_k[n]|^2$ over all values of k and n.

From the above discussion, one finds that the PAPR of SC-FDMA will be small, if each row of $\mathbf{G}$ has only one significant element, and the significant elements from different rows have amplitudes that are about the same. The ideal case is when each row of $\mathbf{G}$ has one nonzero element and the nonzero elements from all rows have the same magnitude.

From the developments in [27] one may infer that $\mathbf{G}$ fulfills the above desirable properties, to some extent, if $\mathbf{P}$ is a DFT matrix of size $M \times M$. Moreover, a better

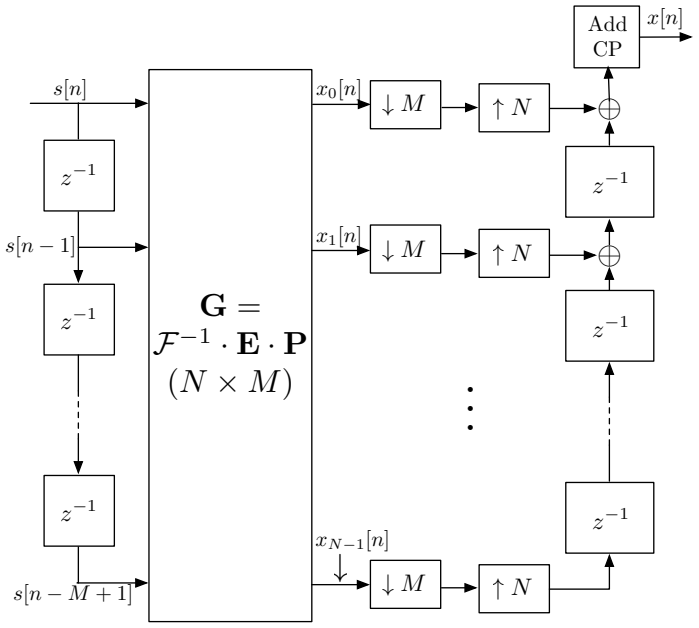

Figure 3.3: A simplified version of the SC-FDMA of Fig. 3.2.

conditioned $\mathbf{G}$ is obtained if $\mathbf{P}$ is constructed by cyclically extending the DFT matrix vertically (i.e., extend $\mathbf{P}$ from size $M \times M$ to $L \times M$, with $L > M$) and applying a rolled-off window to each of its columns. Clearly, here, there is a penalty that one has to pay for reducing PAPR – the number of subcarriers used for transmission of M QAM symbols of a user will increase from M to L.

3.2 SC-FDMA Extension to FBMC

The SC-FDMA structure presented in Fig. 3.2 may be thought of as a special case of a more general structure when the precoder is an analysis filter bank with a prototype filter $H^{\mathrm{a}}(z)$ and the multicarrrier modulator is a synthesis filter bank with a prototype filter $H^{\mathrm{s}}(z)$. Fig. 3.4 presents such a generalization, where $E_k^{\mathrm{a}}(z)$ and $E_k^{\mathrm{s}}(z)$ are the polyphase components associated with $H^{\mathrm{a}}(z)$ and $H^{\mathrm{s}}(z)$. The difference between this structure and that of Fig. 3.2 is the addition of the polyphase components.

Recall from our previous discussions that the choice of the precoder $\mathbf{P}$ results in a well conditioned matrix $\mathbf{G}$ with only one significant element in each of its rows and this leads to a low PAPR. Unfortunately, the presence of the polyphase components $E_k^{\mathrm{a}}(z)$ and $E_k^{\mathrm{s}}(z)$ results in a set of impulse responses between the input and the points prior to the N-fold expanders that will not be as well conditioned as those associated with $\mathbf{G}$. This results in some deterioration of PAPR. To quantify this, Fig. 3.5 compares

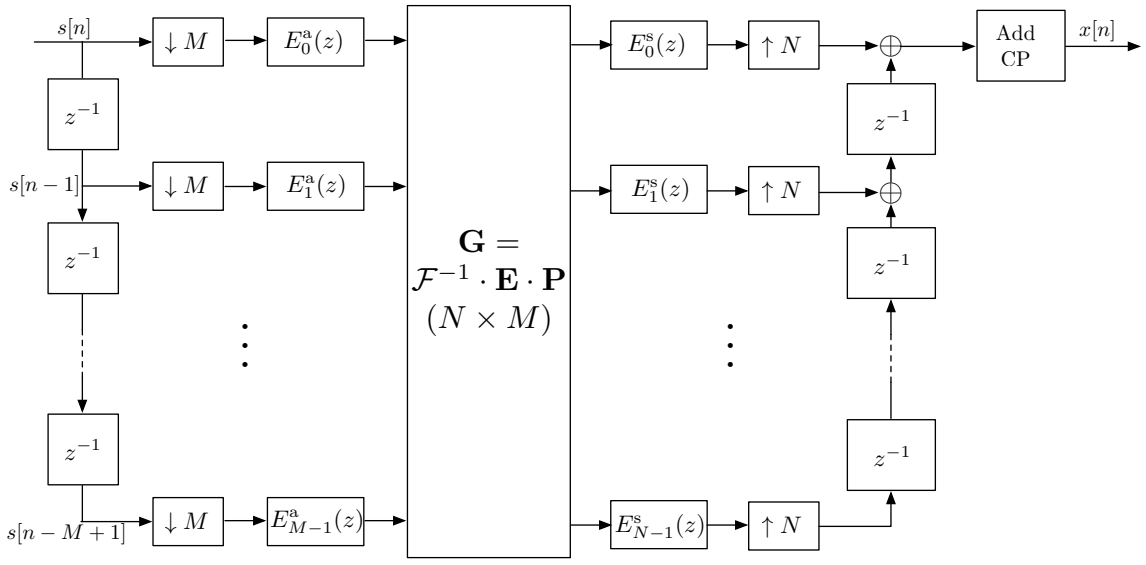

Figure 3.4: A polyphase block diagram of SC-FB. This reduces to Fig. 3.2 when the polyphase components $E_k^{\mathrm{a}}(z)$ and $E_k^{\mathrm{s}}(z)$ are all equal to 1.

the cumulative complementary distribution functions (CCDF) of a user signal where 128 contiguous subcarriers out of 512 subcarriers are used. CCDF is a probability function and is defined as the probability of PAPR being greater than the value specified on the horizontal axis. CCDF curves are presented for the cases when (i) there is no precoder, (ii) SC-FDMA is applied to an OFDM system and the precoder is a DFT matrix (DFTp-OFDM), (iii) and (iv) SC-FDMA is applied to an FBMC system and the precoder is either a DFT or a filter bank. These are labeled DFTp-SMT and FBp-SMT, where SMT refers to the staggered multitone modulation. SMT, which in many publications is referred as OFDM/OQAM, is the most widely studied FBMC technique in the literature, [22]. Also presented in Fig. 3.5 is the result of the single carrier FBMC that is developed in the subsequent sections of this chapter. The FBMC uses a square-root prototype filter with roll-off factor $\alpha = 1$. The design method proposed in [21] has been used to design the prototype filter.

The above results and similar numerical results presented in [19], clearly show that mimicking the SC-FDMA developed for OFDMA to FBMC is not as effective in reducing PAPR.

3.3 Filtering Interpretation of SC-FDMA

An alternative way of looking at the SC-FDMA of Fig. 3.1 that includes both OFDM and FBMC is presented in Fig. 3.6. This structure contains M parallel branches, each consisting of an analysis filter, $H_k^{\mathrm{a}}(z)$, an M-fold decimator, an N-fold expander, and a

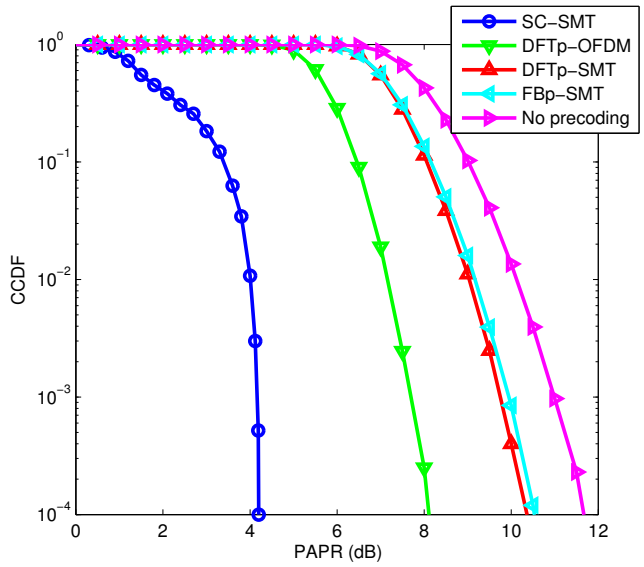

Figure 3.5: Cumulative complementary distribution functions of different modulation methods.

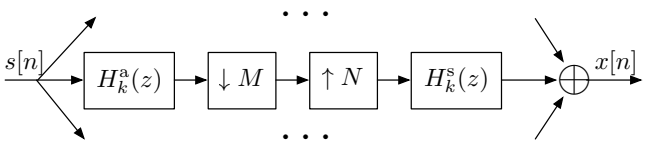

Figure 3.6: The SC-FDMA transmitter presented as a parallel set branches filtering decimator and expanders in the time domain.

synthesis filter, $H_k^{\mathrm{a}}(z)$. Following a few standard steps from the theory of multirate signal processing [20], one finds the z-transform of $x[n]$ as

$$X(z) = \sum_{k=0}^{M-1} A_k(z) S(z^K W_M^k) \tag{3.4}$$

where $K = N/M$ and $W_M = e^{-j2\pi/M}$ and

$$A_k(z) = \frac{1}{M} \sum_{k=0}^{M-1} H_k^{\mathrm{a}}(z^K W_M^k) H_k^{\mathrm{s}}(z). \tag{3.5}$$

If one could design the pair of analysis and synthesis filters such that $A_k(z) = 0$, for $k \neq 0$, (3.4) would simplify to

$$X(z) = A_0(z) S(z^K). \tag{3.6}$$

This result has the following interpretation. The output sequence $x[n]$ is an interpolated version of the input data sequence $s[n]$ with the interpolation factor $K = N/M$ and

interpolation filter $A_0(z)$. Hence, when $s[n]$ is from a specific/known constellation, the PAPR will be a function of $A_0(z)$.

The approach taken in [27] to reduce PAPR by extending the DFT matrix and applying a roll-off window (discussed earlier in this chapter), in fact, serves the purpose of introducing a roll-off to $A_0(z)$ and also forcing $A_k(z) \approx 0$, for $k \neq 0$. However, unfortunately, the results presented in Fig. 3.5 imply that such methods are less effective in FBMC systems.

3.4 Single Carrier for FBMC Systems

Following the above observations, in this section, we concentrate on adopting a novel method for signal carrier modulation in FBMC systems. We note that the presence of the M-fold decimator will introduce M replications of the spectrum of $s[n]$ and, as a result, significant aliasing terms may be introduced in the output sequence $x[n]$, as expressed mathematically in (3.4).

A natural method of removing the aliasing components, is to remove the M-fold decimators from the structure of Fig. 3.6 and instead replace each pair of decimator-expander by an K-fold expander, where, as defined before, $K = N/M$.

Recalling

$$A_0(z) = \frac{1}{M} \sum_{k=0}^{M-1} H_k^{\mathrm{a}}(z^K) H_k^{\mathrm{s}}(z), \tag{3.7}$$

and assuming that $H_k^{\mathrm{a}}(z)$ and $H_k^{\mathrm{s}}(z)$ are square-root Nyquist filters, one will find that the terms under summation in (3.7) are Nyquist filters and when the subcarriers are contiguous (as in the case of SC-FDMA in 3GPP LTE) they add up to a flat passband. Fig. 3.7 depicts this concept. $A_0(z)$ is thus a passband filter with transition bands that resemble that of a Nyquist filter with a roll-off factor α/M, where α is the roll-off factor of the prototype filters used for $H_k^{\mathrm{a}}(z)$ and $H_k^{\mathrm{s}}(z)$. Noting that in most practical implementations of SMT (OFDM/OQAM), $\alpha = 1$ is used, we conclude that $A_0(z)$ is a Nyquist filter with a normalized bandwidth of $M/N = 1/K$, roll-off factor $1/M$, and modulated to desired position within the multiple access band. Moreover, considering the fact that modulation in SMT is offset QAM (OQAM), we propose the structure presented in Fig. 3.8.

In this structure $H(z)$ is a Nyquist filter in which the zero crossings of its impulse response occur at an interval of K samples. The inputs $s_{\mathrm{R}}[n]$ and $s_{\mathrm{I}}[n]$ are the real and imaginary parts of $s[n]$. The additional factor $z^{-\frac{K}{2}}$ is to introduce an offset of half a symbol interval between the phase and quadrature parts of each symbol. Finally, the multiplication by $e^{j2\pi f_c n}$ shifts the generated OQAM signal to the desired part of the multiple access band.

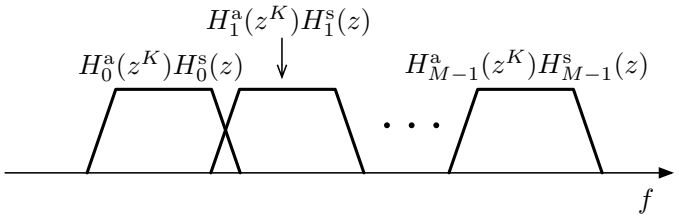

Figure 3.7: The SC-FDMA transmitter presented as a parallel set branches filtering decimator and expanders in the frequency domain.

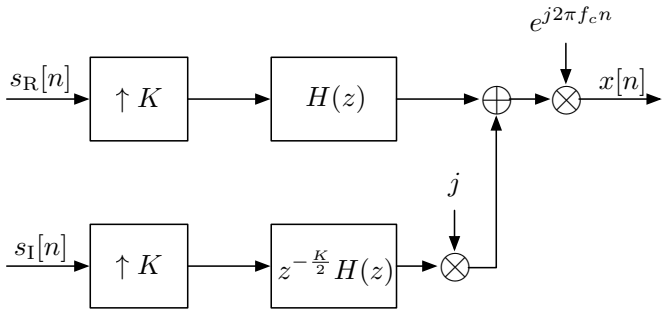

Figure 3.8: The SC-FB structure of a transmitter in the uplink of and FBMC-based multiple access network.

The CCDF result of this modulator is presented in Fig. 3.5 along with those of SC-FDMA proposed in the 3GPP LTE standard and other methods that were discussed earlier. As noted before, direct mimicking of the 3GPP LTE proposed SC-FDMA in an FBMC-based system leads to an inferior PAPR as compared to OFDM. However, as the results presented in Fig. 3.5 show, the single carrier modulation that we propose here results in a PAPR which is almost 4 dB better than the SC-FDMA proposed in the 3GPP LTE standard for OFDM-based systems. Nevertheless, one should note that the PAPR of SC-FDMA can be improved by adding a window at the output of the precoder, [27]. However, this would be at the cost of some loss in bandwidth efficiency. The results presented in Figure 2 of [15] (which uses the same parameters as here) indicate that to achieve a PAPR comparable to the proposed method here, a roll-off factor $\alpha = 0.6$ should be applied to SC-FDMA. This is an additional 60% in bandwidth usage.

We note that part of the reason that the PAPR of the proposed SC-SMT is significantly lower than the PAPR in SC-FDMA is related to the fact that it is based on OQAM modulation. The off-set introduced between the phase and quadrature components of each symbol distributes the power more homogeneously within each symbol period. We also

note that the single carrier nature of the transmitted signal in SC-SMT does not avoid the possibility of using a multicarrier demodulator as in SC-FDMA. Subcarrier analysis and per subcarrier equalization proposed in the 3GPP LTE standard are directly applicable to the single carrier modulated SMT method.

3.5 Conclusion

We presented a study of a SC-FDMA system proposed by the 3GPP LTE standard committee. We also explored a direct mimicking of the SC-FDMA to an FBMC-based network. Our study revealed that such a method does not lead to a satisfactory performance. It also revealed the reasons behind why mimicking SC-FDMA to FBMC-based systems has inferior performance when compared to OFDM-based systems. This understanding of SC-FDMA led us to propose a novel single carrier modulation for FBMC systems. The proposed system can still benefit from the frequency domain equalization that is proposed in 3GPP LTE. In addition, similar to previous reports on FBMC, e.g., [5], one can still argue that the superior confinement of the spectra of different users within different bands makes FBMC an excellent choice for cognitive radios.

CHAPTER 4

ANALYSIS AND OPTIMIZATION OF PEAK-TO-AVERAGE POWER RATIO IN SC-FDMA

In the previous chapter, we explored the method of extending the techniques used in filter bank multicarrier systems to SC-FDMA. We found that the direct application of SC-FDMA to FBMC is not successful, but we also showed that FBMC techniques can lead to significant reduction in PAPR when it is used in a way that is not limited by the structure of SC-FDMA. Thus, in this chapter, we will investigate the use of FBMC techniques to optimize the precoder in SC-FDMA without making major modifications to the structure of SC-FDMA . We find that the precoder can be mathematically optimized, which leads to the reduction of PAPR.

Some recent works have proposed minimization of the variance of the instantaneous power of the output signal of the transmitter as a means of reducing PAPR to near its minimum value. However, the studies so far have been based on intuitions and observation of some numerical results. The goal of this chapter is to develop a mathematical procedure to further establish the significance of this method. We formulate the problem in the form of a method of Lagrange multipliers and analyze its second-order conditions to confirm analytically that the optimal window is indeed a strict local minimizer. We also analyze and compensate the noise enhancement penalty of the optimal window. Our analysis also leads us to find new window functions that further reduce the PAPR and improve the BER performance.

SC-FDMA systems fall into two categories: interleaved FDMA and localized FDMA [15]. While interleaved FDMA performs better in terms of PAPR, it is not an appealing solution when multiple users suffer from even a small mismatch in their carrier frequencies. Noting this, the interleaved FDMA has not been considered in the LTE standard [17]. Therefore, the localized FDMA, where a block of contiguous subcarriers are allocated to each user, is the case of practical interest, hence, the focus of this chapter.

In its simplest form, the localized FDMA takes a set of M data symbols, applies a discrete Fourier transform (DFT) to them, and passes the outputs of the DFT to M contiguous inputs of an inverse DFT (IDFT) of size $N > M$; this has been currently suggested in the LTE standard [17]. The latter block is the multicarrier modulator in an OFDM system. Falconer [26] has studied this setup in some detail and has developed an optimization procedure for weighting the outputs of the DFT to reduce PAPR at the transmitter output, *viz.*, at the output of the IDFT block. Falconer [26] has suggested minimizing the variance of instantaneous power of an FDMA signal, instead of the conventional method of PAPR minimization. He argues that sporadic peaks that may determine the PAPR may result in some insignificant loss in performance and thus should not be over-counted. On the other hand, the variance of instantaneous power takes into account the frequency of the signal peaks and thus provides a better measure of the loss of quality that arises because of the amplifier nonlinearity.

Falconer [26] begins with an arbitrary precoding matrix and runs an optimization procedure to minimize the variance of instantaneous power at the transmitter output. He observes that his optimization procedure always converges to the same solution, irrespective of its starting point. He thus concludes that the cost function (the variance of instantaneous power) that he defines has a global optimum that can be found numerically. The precoder solution found by Falconer [26] is a slight modification to DFT precoder and is suggested in the LTE standard [17]. If one denotes the DFT matrix of size M by $\boldsymbol{\mathcal{F}}_M$, the Falconer precoder is given by

$$\mathbf{P} = \mathbf{W}\boldsymbol{\mathcal{F}}_M \tag{4.1}$$

where $\mathbf{W}$ is a diagonal matrix with elements of w_0, w_1, $\cdots$, w_{M-1}. In other words, each column of $\boldsymbol{\mathcal{F}}_M$ is point-wise multiplied by the column vector $\mathbf{w} = [w_0\ w_1\ \cdots\ w_{M-1}]^{\mathrm{T}}$. We refer to $\mathbf{w}$ as the *window*. Unfortunately, the optimum precoding suggested by Falconer [26] yields only a fraction of 1 dB gain over the conventional SC-FDMA, i.e., when the window $\mathbf{w}$ is a rectangular. It thus seems reasonable to search for other alternative methods that result in a more significant gain in PAPR (or, equivalently, the variance of the instantaneous power).

Slimane [27] has given a different point of view of the precoding that targets the said "more significant gain in PAPR." He proposes a precoding method in which the output samples from the DFT precoder are extended to a length $L > M$ through a periodic repetition and then applying a window to them before passing the result to the IDFT block. This precoding method may mathematically be written as

$$\mathbf{P} = \mathbf{W}\boldsymbol{\mathcal{F}}_M^{\mathrm{e}} \tag{4.2}$$

where $\boldsymbol{\mathcal{F}}_M^{\mathrm{e}}$ is an $L \times M$ matrix obtained by periodically extending each column of $\boldsymbol{\mathcal{F}}_M$ from length M to $L > M$ and $\mathbf{W}$ is a diagonal window matrix with a compatible size. In other words, while the 3GPP-LTE standard and the Falconer approach assumes an SC-FDMA without any excess bandwidth, Slimane [27] allows some excess bandwidth in favor of reducing PAPR. Slimane [27], in his numerical examples, has studied two choices of the window functions: raised-cosine (RC) and square-root raised-cosine (SRRC). The numerical results presented in [27] reveal that for a given excess bandwidth, the SRRC is always a better choice than the RC window. However, one may note that this is a counter-intuitive result, given that the RC window has smoother edges than the SRRC window and thus expectedly (and actually) has smaller time-domain side-lobes. Furthermore, one may wonder if there is any window that gives a better performance than the SRRC.

One may also note that the introduction of an excess bandwidth requires allocation of part of the transmit power to the corresponding subcarriers that may be called, *redundant subcarriers*. This, clearly constitute a loss of power from the subcarriers in the band of interest (called, *data subcarriers*). This loss can be compensated, if the generated transmit signal has lower peak, thus allowing a higher level of transmit signal, when the transmitter power amplifier is peak (but, not power) limited.

We have studied the method of Slimane [27] and have arrived at some logical reasoning as to why the SRRC window outperforms the RC window [24]. We have also extended the study of Falconer to the case where the precoder $\mathbf{P}$ is of size $L \times M$ and have made similar observation to that of [26] in this case as well, i.e., minimizing the variance of the instantaneous power at the transmitter output leads to the precoder matrix $\mathbf{P}$ given in (4.2).

The goal is to further our study of the variance of the instantaneous power as a cost function by making the following contributions:

- Using a novel matrix formulation of the SC-FDMA modulator, we identify the main criteria that leads to improved PAPR and power variance. This formulation, in particular, explains why the SRRC window is superior to the RC window.

- Instead of direct optimization of the precoder matrix $\mathbf{P}$, we formulate the problem to directly optimize the window vector $\mathbf{w}$. This reduces the problem side from LM variables to L, hence leading to a much faster design.

- Simplify and express the power variance as a multinomial with real coefficients and in terms of only the entries w_0, w_1, $\cdots$, w_{L-1}, which enables us to derive its gradient and Hessian for analysis.

- Formulate the problem in a form of the method of Lagrange multipliers and analyze its second-order conditions to confirm analytically that the optimal window is indeed a strict local minimizer.

- Analyze and compensate the noise enhancement penalty of the optimized precoder.

- Compare the Complementary Cumulative Distribution Function (CCDF) of the PAPR of the optimized precoder with existing precoders in the literature and confirm that the precoder obtained from the optimization indeed has the best performance.

4.1 Transfer Function of SC-FDMA

As mentioned in the previous chapter, the basic principles of SC-FDMA in the form adopted in the 3GPP LTE standard are laid out in [17], and an example of the transmitter structure is presented in [27]. Fig. 4.1 presents a block diagram of such a SC-FDMA transmitter. A user data stream $s[n]$ is passed through a serial-to-parallel converter (S/P) that divides it into M parallel substreams. In a conventional OFDMA, these substreams are directly allocated to M subcarriers in an OFDM modulator (the IFFT block in Fig. 4.1) with a total of $N > M$ subcarriers. In SC-FDMA, a precoder is inserted between the S/P and OFDM modulator. The precoder takes the M output samples of S/P and premultiplies them with a matrix $\mathbf{P}$ of size $L \times M$, where $L \geq M$. The choice of $L > M$ allows addition of some redundancy that are used to further reduce PAPR. It has been noted in [27] that when $L = M$, a good choice of $\mathbf{P}$ is the DFT matrix, and when $L > M$, $\mathbf{P}$ is obtained by extending the $M \times M$ DFT matrix vertically (repeating rows cyclically) and premultiplying the resulting $L \times M$ matrix with a diagonal matrix whose diagonal elements form a proper window function. As noted earlier, the RC and SRRC window functions have been suggested in [27].

Fig. 4.1 presents a block diagram of a SC-FDMA transmitter, where the precoding matrix $\mathbf{P}$ is given by (4.2). Using the standard tools from multirate signal processing, [20, 13], in [23] we have shown that Fig. 4.1 may be converted to Fig. 4.2. The transfer function between the single input $s[n]$ and multiple outputs $x_0[n]$ through $x_{N-1}[n]$ is thus obtain as

$$\mathbf{H}(z) = \frac{\mathbf{X}(z)}{S(z)} = \mathbf{Gz} \tag{4.3}$$

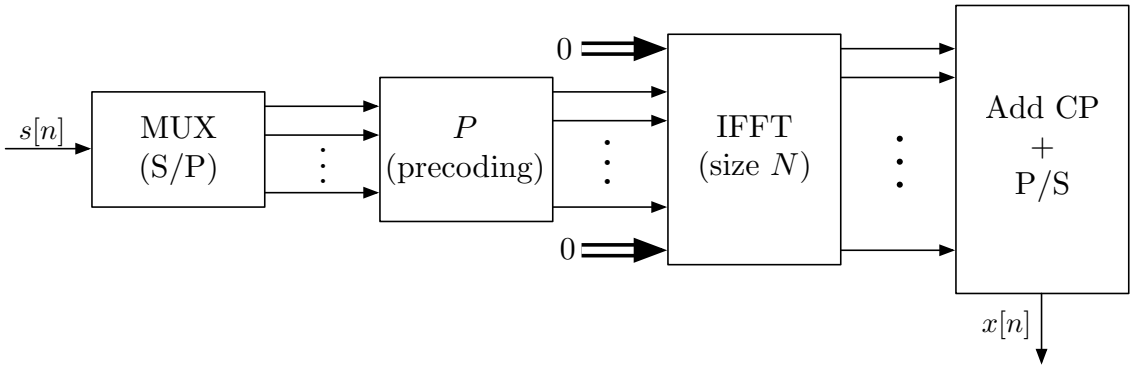

Figure 4.1: An SC-FDMA transmitter.

where $\mathbf{G} = \boldsymbol{\mathcal{F}}_N^{-1}\mathbf{EP}$ and $\mathbf{z}$ is a tapped delay line vector of compatible length, *viz.*, $\mathbf{z} = \begin{bmatrix} 1 & z^{-1} & \cdots & z^{-(M-1)} \end{bmatrix}^{\mathrm{T}}$. The superscript T denotes transpose. $\mathbf{E}$ takes the precoder output of length L and expands it to the length N, by appending zeros.

Alternatively, one may note that the vector of impulse response between the input $s[n]$ and the kth output $x_k[n]$ is the kth row of $\mathbf{G}$.

We also note that the mth column of $\mathbf{P}$ is

$$\begin{bmatrix} w_0 e^{-j\frac{2\pi m f_0}{M}} & w_1 e^{-j\frac{2\pi m f_1}{M}} & \cdots & w_{L-1} e^{-j\frac{2\pi m f_{L-1}}{M}} \end{bmatrix}^{\mathrm{T}},$$

where $\{f_0, f_1, \cdots, f_{L-1}\}$ is a contiguous set of frequency indices from $\{0, 1, \cdots, N-1\}$. In other words, the mth column of $\mathbf{P}$ is the direct product of the window $\mathbf{w}$ and the complex sine-wave $e^{-j\frac{2\pi m f_k}{M}}$, i.e., a modulated version of the window vector $\mathbf{w}$. Hence, the entry (k, m) of $\mathbf{G}$ is obtained as [23]

$$g_{k,m} = \frac{1}{N} \sum_{l=0}^{L-1} w_l e^{-j\frac{2\pi f_l}{N}\left(\frac{Nm}{M} - k\right)}. \tag{4.4}$$

This implies that each column of $\mathbf{G}$ has an envelop that corresponds to the IDFT of $\mathbf{w}$.

For comparison purposes, we can express the $\mathbf{G}$ matrix for an OFDM system. This is done by observing that $\mathbf{P}$ is an identity matrix for OFDM. Then the entry (k, m) of $\mathbf{G}$ becomes $g_{k,m} = \frac{1}{N} e^{-j\frac{2\pi k f_l}{N}}$.

The PAPR of the SC-FDMA transmitter may be calculated as [27]

$$\mathrm{PAPR} = \frac{\max_{k,n} |x_k[n]|^2}{\mathrm{avg}[|x_k[n]|^2]}. \tag{4.5}$$

Following Fig. 4.2, one finds that

$$x_k[n] = \sum_{m=0}^{M-1} g_{k,m} s[n-m]. \tag{4.6}$$

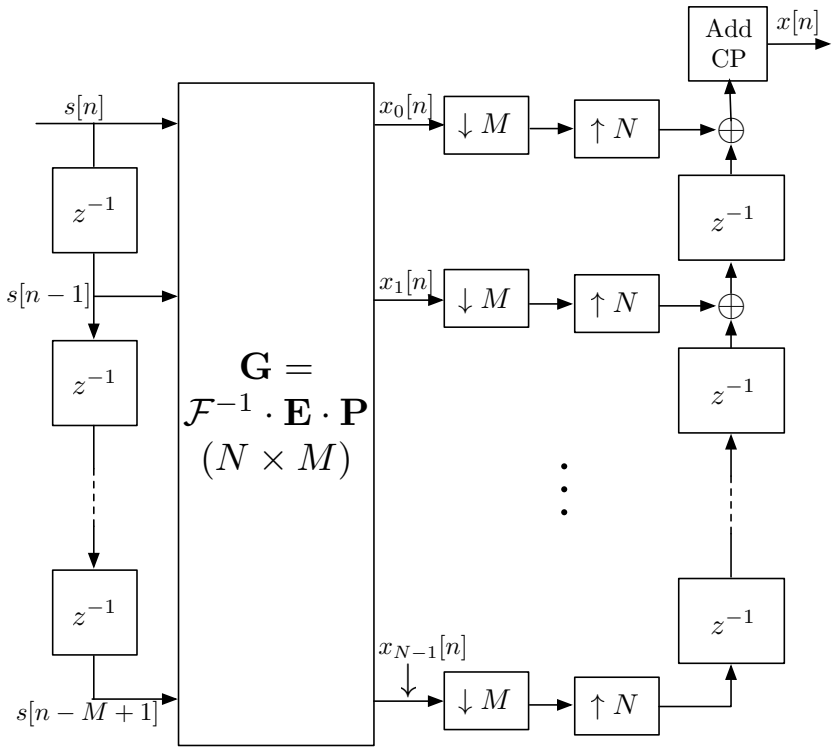

Figure 4.2: A simplified version of the SC-FDMA.

Using $s_{\max}$ to denote $\max |s[n]|$, one finds that

$$x_k[n] \leq \sum_{m=0}^{M-1} |g_{k,m}| s_{\max}. \tag{4.7}$$

Hence, to minimize PAPR, we should look for a $\mathbf{G}$ (or, equivalently, a precoder $\mathbf{P}$) that minimizes $\max_k \sum_{m=0}^{M-1} |g_{k,m}|$, subject to $\text{avg}[|x_k[n]|^2]$ being a constant.

4.2 Precoder Impact on PAPR

In this section, we develop some insight into the properties of the SC-FDMA by studying the matrix $\mathbf{G}$ through a few numerical examples. We plot the magnitudes of the entries of $\mathbf{G}$ for OFDM and three different precoders. The following window functions are considered for $\mathbf{w}$: (i) a rectangular window (conventional SC-FDMA); (ii) an RC window; and (iii) an SRRC window. The window functions are normalized such that the output power at transmitter will always be equal to one; hence, $\max_k \sum_{m=0}^{M-1} |g_{k,m}|$ (in dB) will be equal to PAPR.

Fig. 4.3 presents a set of colormaps of $\mathbf{G}$ for OFDM and the three choices of the window function. Here, we have set $M = 16$, $L = 20$ and $N = 256$. Hence, the matrix $\mathbf{G}$ has 16

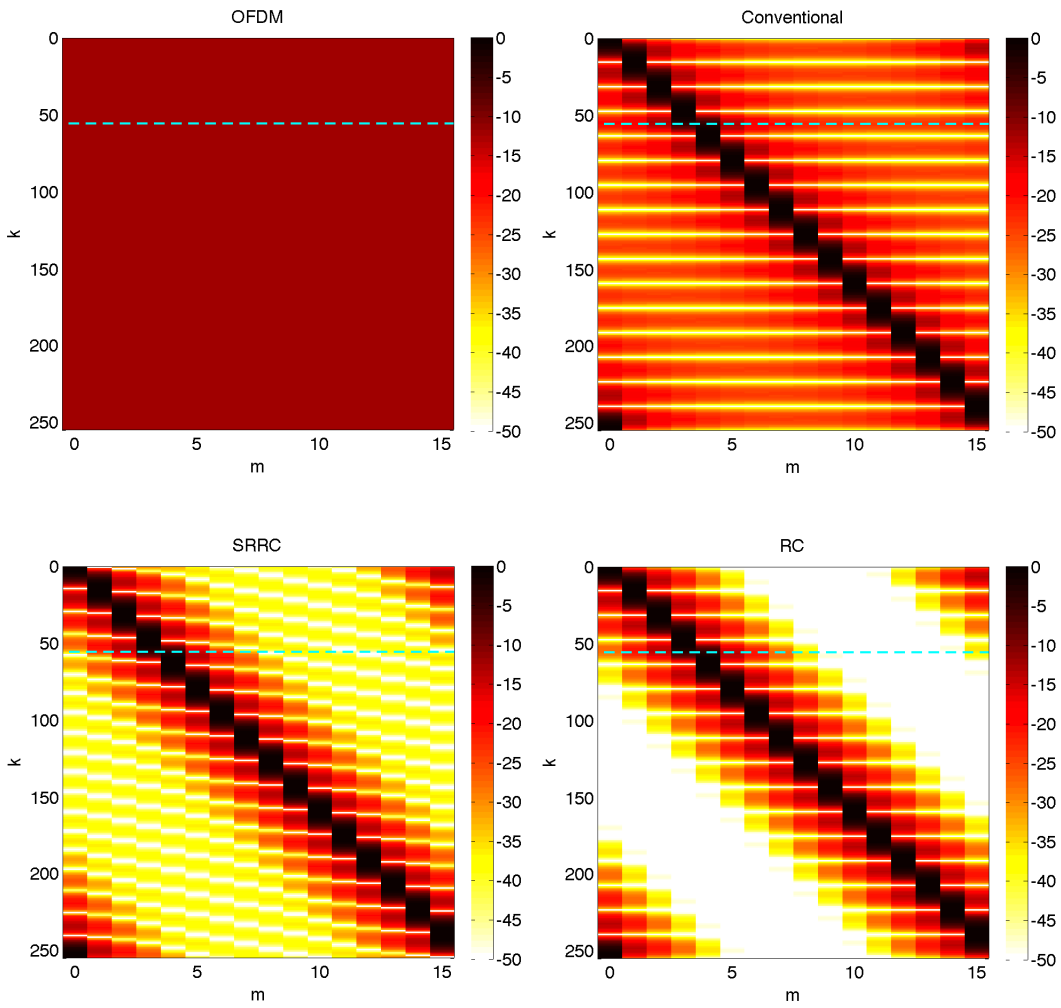

Figure 4.3: Colormaps of $\mathbf{G}$ for OFDM and three different precoders. Colormap scale is in dB. For OFDM, the colormap has a flat amplitude across all elements of $\mathbf{G}$. For other cases, a sinc-like pulse is observed along each column of $\mathbf{G}$.

columns and 256 rows. Observe that for OFDM the corresponding $|g_{k,m}|$ is a constant, thus its colormap is a flat surface. For the three window functions, the patterns of the columns of $\mathbf{G}$, reflect a sinc-like shape along each column, which obviously is the magnitude of the Fourier transform of the window $\mathbf{w}$. Expectedly, for the case of the rectangular window, the side-lobes decay slower than their counterparts in the RC and SRRC window. Moreover, RC window side-lobes are smaller than and decay faster than those of the SRRC window. We also note that the successive columns of $\mathbf{G}$ are obtained by applying circular shifts to its first column. Here, there is a 16-sample shift between each pair of adjacent columns; originating from $N/M = 16$.

Recall that the sum of magnitudes of elements in each row of $\mathbf{G}$, i.e., $\sum_{m=0}^{M-1} |g_{k,m}|$, is

equal to the peak magnitude of the respective output sample, and the maximum of this quantity across all rows of $\mathbf{G}$ (in dB) is equal to PAPR. Also, from the patterns presented in Fig. 4.3, one may note that the rows follow a periodic pattern, with a sample period of 16 ($= N/M$).

Since we are interested in the PAPR, we should compare the maximum value of the sum $\sum_{m=0}^{M-1} |g_{k,m}|$ of three precoders. The results are presented in Table 4.1. Discussed in more detail in Section 4.6, we see that the rectangular window (conventional SC-FDMA) performs the worst out of the three cases. Also, as discussed in [27], the SRRC window outperforms the RC window. For the cases presented in [27], the SRRC gain over RC window is about 1 dB. For the case presented here, we observe 0.6 dB gain. The difference is because the parameters used here are different from those in [27].

Careful examination of the colormaps in Fig. 4.3 reveals that peaks occur at the rows where the summation $\sum_{m=0}^{M-1} |g_{k,m}|$ receives a pair of larger contributing terms from the main lobes of two successive columns (near the edges of the black regions) and a number of smaller contributing terms from the side-lobes in the other columns. The rows where the peaks occur are indicated by the dotted cyan lines on the colormaps in Fig. 4.3. In the case of rectangular window, these smaller terms can add up and increase PAPR significantly. For the cases of the RC and SRRC window, the smaller frequency domain side-lobes, obviously, reduce the contribution of the smaller terms in $\sum_{m=0}^{M-1} |g_{k,m}|$; hence, leading to smaller PAPRs. Moreover, we observe that although in the RC case, the peaks of the side-lobes at different columns align at the same positions across the rows $k = \frac{M}{2}$ + multiples of M (the dotted line being one of them), hence, constructively add and therefore increase the PAPR; this is not the case in SRRC. In other words, the PAPR correlates to the sum of $|g_{k,m}|$ along the dotted lines, and in the case of RC the alignment of the large values of $|g_{k,m}|$ increases the PAPR. This property of the SRRC, which we refer to as *side-lobes misalignment*, explains why the SRRC window leads to a lower PAPR.

4.3 Improving PAPR and Power Variance

From the above observations, the following criteria should be considered in choosing a window function $\mathbf{w}$ that may result in an improved PAPR:

1. The side-lobes of the Fourier transform of $\mathbf{w}$ should be as small as possible.

2. The side-lobes of the sinc-like pulses in columns of $\mathbf{G}$ should not align across the rows of $\mathbf{G}$; see the above discussion related to the RC window. This avoids possible destructive addition of the terms in the summation $\sum_{m=0}^{M-1} |g_{k,m}|$.

Table 4.1: List of the simulated PAPR at CCDF of 10^{-5} (from Fig. 4.9), the theoretical upper limits of the PAPR in dB, the simulated INP at CCDF of 10^{-5} (from Fig. 4.10) and the power variance Σ^2 normalized (theoretical and simulated) for different precoders with the parameters $M = 16, N = 256$ and $L = 20$ (for SRRC, RC, Optimized and Optimized with CNEP). For the simulated values, 10^6 frames of 16-channel QPSK symbols were used.

Precoder type	Simulated PAPR (dB)	$20\log_{10}\left(\max_k \sum_{m=0}^{M-1} \lvert g_{k,m}\rvert\right)$	Simulated INP (dB)	Theoretical Σ^2	Simulated Σ^2
None (OFDM)	10.75	12.0412	9.82	0.9375	0.9366
Conventional SC-FDMA	7.65	8.7162	7.06	0.3320	0.3323
SRRC	5.19	5.3329	4.97	0.2317	0.2316
RC	5.88	5.9515	5.66	0.2582	0.2581
Optimized window	4.45	4.8588	4.11	0.1935	0.1936
Optimized window with CNEP	4.32	4.5737	4.04	0.2018	0.2018

3. In addition, in order to transmit all subcarriers of interest with about the same power, the window function $\mathbf{w}$ should stay close to flat over these subcarriers: the M midpoints in $\mathbf{w}$ over the data subcarriers.

We note that the third criterion is not really necessary, but should not be violated badly, since a small gain at any point in the M midpoints of $\mathbf{w}$ may result in a poor receiver performance. It may also be of interest to note that the third criterion is not satisfied for the SRRC and RC window functions. It is mildly violated near the edges of the frequency band. The impact of variation of $\mathbf{w}$ over the subcarriers of interest is discussed in [26] and to quantify it the noise enhancement penalty

$$\zeta = \sum_{k \in \mathcal{M}} \frac{1}{|w_k|^2} \tag{4.8}$$

is introduced, where $\mathcal{M}$ denotes the set of indices of the data subcarriers. It is argued in [26] that the allocation of different gains to various subcarriers results in a performance loss that can be as large as ζ (in dB), but may be lower for more advance receiver detection schemes. For a zero forcing equalizer the loss is equal to ζ and for a turbo equalizer may be negligibly small.

One may note that the above criteria are vaguely defined. Thus, defining a cost function whose optimization may lead to a good window function with a minimized PAPR may not be a straightforward task. Falconer [26] has suggested minimizing the variance of instantaneous power of an FDMA signal, instead of the conventional method of PAPR minimization. In the next section, we will analyze the power variance of the precoded multicarrier signal as a function of $\mathbf{w}$, the window of the precoder matrix. Instead of direct optimization of the precoder matrix $\mathbf{P}$ as in [26], we formulate the problem to directly optimize the window vector w. We show that this allows us to design better window functions than those that have been proposed in [27].

In order to find a suitable precoder that minimizes the PAPR of a multicarrier system with precoding, we need to quantify the dynamic range of the signal as a cost function. We would like to establish the power variance of the precoded multicarrier signal as a function of $\mathbf{w}$, the window of the precoder matrix. The analysis of power variance is a modified version of the one in [26]. Using (4.3), the mean power of the output samples $x_0[n]$, $x_1[n]$, $\cdots$, $x_{N-1}[n]$ is obtained as

$$\frac{1}{N}\sum_{k=0}^{N-1} E\left(|x_k[n]|^2\right) = \frac{1}{N}\sum_{k=0}^{N-1} E\left(\left|\sum_{m=0}^{M-1} g_{k,m}s[n-m]\right|^2\right)$$
$$= \frac{1}{N}\sum_{k=0}^{N-1}\sum_{m=0}^{M-1} |g_{k,m}|^2, \tag{4.9}$$

assuming $E\left(|s[n-m]|^2\right) = 1$ for all inputs. Using (4.4) and normalizing $\mathbf{w}$ such that $\sum_{l=0}^{L-1} w_l^2 = 1$, this can be simplified to

$$\frac{1}{N}\sum_{k=0}^{N-1}\sum_{m=0}^{M-1} |g_{k,m}|^2 = \frac{1}{N}\sum_{k=0}^{N-1}\sum_{m=0}^{M-1}\left|\sum_{l=0}^{L-1}\frac{1}{N}w_l e^{-j\frac{2\pi f_l}{N}\left(\frac{Nm}{M}-k\right)}\right|^2$$
$$= \frac{1}{N}\sum_{k=0}^{N-1}\sum_{m=0}^{M-1}\left(\sum_{l=0}^{L-1}\frac{w_l^2}{N^2} + \sum_{\substack{p,q=0\\p\neq q}}^{L-1}\frac{w_p w_q}{N^2}e^{-j\frac{2\pi(f_p-f_q)}{N}\left(\frac{Nm}{M}-k\right)}\right)$$
$$= \frac{M}{N^2}, \tag{4.10}$$

if we assume that the amount of excess bandwidth is not too large such that $M \leq L < 2M \leq N$ which implies $\sum_{m=0}^{M-1} e^{-j\frac{2\pi m}{M}(f_p-f_q)} = 0$ and $\sum_{k=0}^{N-1} e^{j\frac{2\pi k}{N}(f_p-f_q)} = 0$ when $p \neq q$. Following [26], we define the variance of power of the output samples $x_0[n]$, $x_1[n]$, $\cdots$, $x_{N-1}[n]$ as the cost function that should be minimized for achieving a good value for PAPR. This cost function can be expanded as

$$\Sigma^2(\mathbf{w}) = \frac{1}{N}\sum_{k=0}^{N-1}\left(E\left[|x_k[n]|^4\right] - \left(\frac{M}{N^2}\right)^2\right)$$
$$= \frac{1}{N}\sum_{k=0}^{N-1} E\left[\left|\sum_{m=0}^{M-1} g_{k,m}s[n-m]\right|^4\right] - \frac{M^2}{N^4}$$
$$= \frac{1}{N}\sum_{k=0}^{N-1}\left[2\left(\sum_{m=0}^{M-1}|g_{k,m}|^2\right)^2 - (2-\sigma_s^4)\left(\sum_{m=0}^{M-1}|g_{k,m}|^4\right)\right] - \frac{M^2}{N^4}, \tag{4.11}$$

where $\sigma_s^4 = E\left(|s[n-m]|^4\right)$. Going through some lengthy derivations, one will find that

$$\frac{1}{N}\sum_{k=0}^{N-1}\left(\sum_{m=0}^{M-1}|g_{k,m}|^2\right)^2 = \frac{M^2}{N^4} + \sum_{\substack{p,q=0\\p\neq q\\f_p-f_q=\pm M}}^{L-1}\frac{M^2}{N^4}w_p^2 w_q^2 + \sum_{\substack{p,q,r,s=0\\p\neq q,r\neq s\\(p,q)\neq(r,s)\\f_p-f_q=f_r-f_s=\pm M}}^{L-1}\frac{M^2}{N^4}w_p w_q w_r w_s \tag{4.12}$$

and

$$\frac{1}{N}\sum_{k=0}^{N-1}\sum_{m=0}^{M-1}|g_{k,m}|^4 = \frac{M}{N^4} + \sum_{\substack{p,q=0\\p\neq q}}^{L-1}\frac{M}{N^4}w_p^2 w_q^2 + \sum_{\substack{p,q,r,s=0\\p\neq q,r\neq s\\(p,q)\neq(r,s)\\f_p-f_q=f_r-f_s}}^{L-1}\frac{M}{N^4}w_p w_q w_r w_s. \tag{4.13}$$

Using these result in (4.11), we obtain (4.14).

$$\begin{aligned}\Sigma^2(\mathbf{w}) &= 2\left(\frac{M^2}{N^4}+\sum_{\substack{p,q=0\\ p\neq q\\ f_p-f_q=\pm M}}^{L-1}\frac{M^2}{N^4}w_p^2w_q^2+\sum_{\substack{p,q,r,s=0\\ p\neq q,r\neq s\\ (p,q)\neq(r,s)\\ f_p-f_q=f_r-f_s=\pm M}}^{L-1}\frac{M^2}{N^4}w_pw_qw_rw_s\right)\\ &\quad-(2-\sigma_s^4)\left(\frac{M}{N^4}+\sum_{\substack{p,q=0\\ p\neq q}}^{L-1}\frac{M}{N^4}w_p^2w_q^2+\sum_{\substack{p,q,r,s=0\\ p\neq q,r\neq s\\ (p,q)\neq(r,s)\\ f_p-f_q=f_r-f_s}}^{L-1}\frac{M}{N^4}w_pw_qw_rw_s\right)-\frac{M^2}{N^4}.\end{aligned} \tag{4.14}$$

The significance of (4.14) is that we obtain the power variance as a cost function in terms of only the entries of $\mathbf{w}$, the window of the precoder matrix. The reader should be reminded that this is done under the assumption that the precoder P is based on DFT and is in the form of (4.2) with real entries in $\mathbf{w}$, as also suggested in [27] and for relatively simple implementation using FFT. As the cost function $\Sigma^2(\mathbf{w})$ is a multinomial of $w_0, w_1, \cdots, w_{L-1}$, the first and second derivatives can be evaluated analytically in a straightforward manner (albeit long) which help us understand the structure of the cost function.

For comparison, we can also evaluate the power variance for OFDM. Recall from Section 4.1 that in the case of OFDM, we have $g_{k,m}=\frac{1}{N}e^{-j\frac{2\pi kf_l}{N}}$. Then

$$\frac{1}{N}\sum_{k=0}^{N-1}\sum_{m=0}^{M-1}|g_{k,m}|^2=\frac{1}{N}\sum_{k=0}^{N-1}\sum_{m=0}^{M-1}\frac{1}{N^2}=\frac{M}{N^2} \tag{4.15}$$

and

$$\begin{aligned}\Sigma^2=&\frac{1}{N}\sum_{k=0}^{N-1}\left[2\left(\sum_{m=0}^{M-1}|g_{k,m}|^2\right)^2-(2-\sigma_s^4)\left(\sum_{m=0}^{M-1}|g_{k,m}|^4\right)\right]-\frac{M^2}{N^4}\\ =&\frac{1}{N}\sum_{k=0}^{N-1}\left[2\left(\sum_{m=0}^{M-1}\frac{1}{N^2}\right)^2-(2-\sigma_s^4)\left(\sum_{m=0}^{M-1}\frac{1}{N^4}\right)\right]-\frac{M^2}{N^4}\\ =&\frac{M^2}{N^4}-(2-\sigma_s^4)\frac{M}{N^4}.\end{aligned} \tag{4.16}$$

4.4 Analysis of Power Variance

Using Lagrange multipliers with the constraint $g(\mathbf{w}) = \sum_{l=0}^{L-1} w_l^2 = 1$, we start with the Lagrangian function

$$l(\mathbf{w}, \lambda) = \Sigma^2(\mathbf{w}) + \lambda \left(g(\mathbf{w}) - 1\right) \tag{4.17}$$

and find the solution of $\nabla l(\mathbf{w}, \lambda) = 0$. The optimum window can be obtained numerically by performing the method of steepest descent using the gradient of $\Sigma^2(\mathbf{w})$ with respect to $\mathbf{w}$. The constraint $\sum_{l=0}^{L-1} w_l^2 = 1$ can be enforced by normalizing $\mathbf{w}$ after each step in the convergence.

Through a vast set of numerical examples, we have found that as long as the coefficients w_l are kept positive, the above procedure always converges to the same solution. This is in line with the results reported in [26]. In this section, we mathematically prove that the converged window is indeed a strict local minimizer of $\Sigma^2(\mathbf{w})$ subject to $g(\mathbf{w}) = 1$. This mathematical proof along with the numerical tests performed by us and Falconer [26] establishes the fact that the constrained cost function (4.17) has a single minimum within the set $\left\{\mathbf{w} = (w_0, w_1, \cdots, w_{L-1}) \middle| w_l > 0 \text{ and } g(\mathbf{w}) = 1\right\}$.

We recall from the theory of Lagrangian functions, [29], that $\mathbf{w}_\mathrm{o}$ is a strict local minimizer of the constrained cost function (4.17) if the following conditions hold:

1. $\nabla\Sigma^2(\mathbf{w}_\mathrm{o}) + \lambda_\mathrm{o}\nabla g(\mathbf{w}_\mathrm{o}) = \mathbf{0}$

2. For any $\mathbf{y}$ such that $\mathbf{y}^\mathrm{T}\mathbf{w}_\mathrm{o} = 0$, $\mathbf{y}^\mathrm{T}\mathbf{L}(\mathbf{w}_\mathrm{o}, \lambda_\mathrm{o})\mathbf{y} > 0$, where $\mathbf{L}(\mathbf{w}_\mathrm{o}, \lambda_\mathrm{o})$ is the Hessian matrix (with respect to $\mathbf{w}$) of the Lagrangian function $l(\mathbf{w}, \lambda)$ evaluated at $\mathbf{w}_\mathrm{o}$ and λ_o. This is known as the second-order sufficient conditions for Lagrange multipliers, [29].

First, we need to figure out the expression for $\mathbf{L}(\mathbf{w}, \lambda)$. The Hessian matrix $\mathbf{L}(\mathbf{w}, \lambda)$ has the following form:

$$\begin{aligned}
\mathbf{L}(\mathbf{w}, \lambda) &= \mathcal{H}(\Sigma^2(\mathbf{w})) + \lambda(\mathcal{H}(g(\mathbf{w}) - 1)) \\
&= \mathcal{H}(\Sigma^2(\mathbf{w})) + \lambda\left(\mathcal{H}\left(\left[\sum_{l=0}^{L-1} w_l^2\right] - 1\right)\right) \\
&= \mathcal{H}(\Sigma^2(\mathbf{w})) + 2\lambda\mathbf{I},
\end{aligned} \tag{4.18}$$

where $\mathcal{H}(\cdot)$ denotes the Hessian of the argument. This simple relationship between $\mathbf{L}(\mathbf{w}, \lambda)$ and $\mathcal{H}(\Sigma^2(\mathbf{w}))$ in (4.18) shows that if $\mathcal{H}(\Sigma^2(\mathbf{w}))$ has an eigenpair $(\alpha, \mathbf{v})$, then $(\alpha + 2\lambda, \mathbf{v})$ is an eigenpair of $\mathbf{L}(\mathbf{w}, \lambda)$. Hence, to proceed, we perform an eigenanalysis of $\mathcal{H}(\Sigma^2(\mathbf{w}))$.

It can be shown that the gradient $\nabla\Sigma^2(\mathbf{w})$ and the Hessian matrix $\mathcal{H}(\Sigma^2(\mathbf{w}))$ are related as

$$3\nabla\Sigma^2(\mathbf{w}) = \mathcal{H}(\Sigma^2(\mathbf{w}))\mathbf{w}. \tag{4.19}$$

This is proved by evaluating $\nabla\Sigma^2(\mathbf{w})$ and $\mathcal{H}(\Sigma^2(\mathbf{w}))$ directly and comparing the results. For an optimum window $\mathbf{w}_\mathrm{o}$, the first condition (above) is derived by letting $\nabla l(\mathbf{w}, \lambda) = 0$. This also leads to

$$\begin{aligned}\nabla\Sigma^2(\mathbf{w}_\mathrm{o}) &= -\lambda_\mathrm{o}\nabla g(\mathbf{w}_\mathrm{o}) \\ &= -2\lambda_\mathrm{o}\mathbf{w}_\mathrm{o}.\end{aligned} \tag{4.20}$$

Substitute (4.20) into (4.19), we obtain

$$-6\lambda_\mathrm{o}\mathbf{w}_\mathrm{o} = \mathcal{H}(\Sigma^2(\mathbf{w}_\mathrm{o}))\mathbf{w}_\mathrm{o}. \tag{4.21}$$

This implies that $(-6\lambda_\mathrm{o}, \mathbf{w}_\mathrm{o})$ is an eigenpair of $\mathcal{H}(\Sigma^2(\mathbf{w}_\mathrm{o}))$. Recalling the discussion about the eigenpairs of $\mathbf{L}(\mathbf{w}, \lambda)$ and $\mathcal{H}(\Sigma^2(\mathbf{w}))$ in the paragraph after (4.18), this, in turn, implies that $(-4\lambda_\mathrm{o}, \mathbf{w}_\mathrm{o})$ is an eigenpair of $\mathbf{L}(\mathbf{w}_\mathrm{o}, \lambda_\mathrm{o})$.

We now have the tools to check whether a numerically obtained optimum window $\mathbf{w}_\mathrm{o}$ satisfies the second-order sufficient conditions for Lagrange multipliers and whether it is indeed a strict local minimizer of the cost function $\Sigma^2(\mathbf{w})$. Let the vectors $\mathbf{v}_0, \mathbf{v}_1, \cdots, \mathbf{v}_{L-1}$ be an orthogonal eigenbasis of $\mathbf{L}(\mathbf{w}_\mathrm{o}, \lambda_\mathrm{o})$ with the corresponding eigenvalues $\alpha_0, \alpha_1, \cdots, \alpha_{L-1}$, and with $\mathbf{v}_0 = \mathbf{w}_\mathrm{o}$ and $\alpha_0 = -4\lambda_\mathrm{o}$. If $\mathbf{y}$ is a vector such that $\mathbf{y}^\mathrm{T}\mathbf{w}_\mathrm{o} = 0$, then $\mathbf{y}$ must be a linear combination of $\mathbf{v}_1, \cdots, \mathbf{v}_{L-1}$. Then we have

$$\begin{aligned}\mathbf{y}^\mathrm{T}\mathbf{L}(\mathbf{w}_\mathrm{o}, \lambda_\mathrm{o})\mathbf{y} &= \left(\sum_{l=1}^{L-1} c_l\mathbf{v}_l\right)^\mathrm{T} \mathbf{L}(\mathbf{w}_\mathrm{o}, \lambda_\mathrm{o}) \left(\sum_{l=1}^{L-1} c_l\mathbf{v}_l\right) \\ &= \left(\sum_{l=1}^{L-1} c_l\mathbf{v}_l\right)^\mathrm{T} \left(\sum_{l=1}^{L-1} c_l\alpha_l\mathbf{v}_l\right) \\ &= \sum_{l=1}^{L-1} \alpha_l c_l^2 > 0,\end{aligned} \tag{4.22}$$

if $\alpha_1, \cdots, \alpha_{L-1}$ are positive. In other words, the second-order sufficient conditions for Lagrange multipliers will be satisfied if the corresponding eigenvalues of the eigenvectors other than $\mathbf{w}_\mathrm{o}$ are positive.

4.5 Compensation of Noise Enhancement Penalty

One may note that the introduction of an excess bandwidth requires allocation of part of the transmit power to the redundant subcarriers. This can be compensated for by slightly increasing the window coefficients over the data subcarriers and decreasing them over the redundant subcarriers. In this section, we introduce a modification to the cost function $\Sigma^2(\mathbf{w})$ for such compensation. We find that through the new cost function, the power wasted over the redundant subcarriers is decreased without any significant impact on the PAPR and the power variance, but a significant improvement in the bit error rate (BER) curves is observed.

At the receiver, an FFT block is applied to the received signal $r[n]$ after the serial-to-parallel operation and the subcarriers allocated to the user are extracted. Thus, the vector of the analyzed signal at the receiver is given by

$$\begin{aligned}\mathbf{y}[n] &= \begin{bmatrix} y_0[n] & y_1[n] & \cdots & y_{L-1}[n] \end{bmatrix}^{\mathrm{T}} \\ &= \mathbf{E}^{\mathrm{T}} \boldsymbol{\mathcal{F}}_N \begin{bmatrix} r[n] & r[n-1] & \cdots & r[n-N+1] \end{bmatrix}^{\mathrm{T}}.\end{aligned} \tag{4.23}$$

Note that $\mathbf{E}^{\mathrm{T}}$ is the transpose of $\mathbf{E}$ mentioned in Section 4.1 and $\mathbf{E}^{\mathrm{T}}\mathbf{E} = \mathbf{I}_L$, the $L \times L$ identity matrix.

To simplify our discussion, here, we consider the case of an additive white Gaussian noise (AWGN) channel where $r[n] = x[n] + v[n]$ and $v[n]$ is a white Gaussian process. In this case, we can write $\mathbf{y}[n]$ as

$$\begin{aligned}\mathbf{y}[n] &= \mathbf{P} \begin{bmatrix} s[n] \\ s[n-1] \\ \vdots \\ s[n-M+1] \end{bmatrix} + \mathbf{E}^{\mathrm{T}} \boldsymbol{\mathcal{F}}_N \begin{bmatrix} v[n] \\ v[n-1] \\ \vdots \\ v[n-N+1] \end{bmatrix} \\ &= \mathbf{y}^s[n] + \tilde{\mathbf{v}}[n]\end{aligned} \tag{4.24}$$

where $\mathbf{y}^s[n]$ is the signal portion of $\mathbf{y}[n]$ and $\tilde{\mathbf{v}}[n]$ is an AWGN channel noise vector. Note that the FFT does not alter the white Gaussian characteristics of the channel noise, and $\mathbf{E}^{\mathrm{T}}$ does not alter the independence of the elements of $v[n]$.

Starting from our optimized window, we propose a method to search for a modification of it by solving the problem of minimizing the cost function

$$C(\mathbf{w}) = \Sigma^2(\mathbf{w}) - \gamma \frac{E\left[\sum_{k\in\mathcal{M}} \left|\frac{y_k^s[n]}{w_k}\right|^2\right]}{\sum_{k\in\mathcal{M}} \frac{1}{|w_k|^2}} \tag{4.25}$$

where γ is a positive compensation parameter. The second term in (4.25) is the signal-to-noise ratio of the subchannels where the data are extracted from at the receiver. Before the equalization and detection can be performed at the receiver, the roll-off introduced by the window $\mathbf{w}$ has to be compensated for through a frequency domain equalizer for each subcarrier. In other words, the gains $\frac{1}{w_k}$ are multiplied to the corresponding subchannel outputs such that the active subchannels form a flat top. This enhances noise and the power of the noise increases by a factor equal to $\zeta = \sum_{k\in\mathcal{M}} \frac{1}{|w_k|^2}$, i.e., the noise enhancement penalty mentioned in (4.8). The parameter γ in (4.25) is a weight factor that is used to balance the two terms and hence to maximize the performance. We call this "optimization with CNEP" (compensation of noise enhancement penalty).

4.6 Numerical Examples

To provide some insight into the above theoretical results, we present a numerical result. We evaluate the optimum window for the case of $\sigma_s^4 = 1$, $M = 16$, $L = 20$ and $N = 256$. The result is presented in Fig. 4.4. It is observed that the shape of the window looks like a "sun hat" with a curved top from subcarriers $k = L - M$ to $k = M - 1$.

For the above example, the first Lagrange multipliers condition is satisfied for the optimum window $\mathbf{w}_\mathrm{o}$, with the corresponding λ_o of 2.2704×10^{-5}. Eigenanalysis is performed on the numerical value of the matrix $\mathbf{L}(\mathbf{w}_\mathrm{o}, \lambda_\mathrm{o})$, and the smallest eigenvalue has the value of $\alpha_0 = -0.9081 \times 10^{-4}$ with the eigenvector $\mathbf{v}_0 = \mathbf{w}_\mathrm{o}$, the optimum window. This checks out with the equation $\alpha_0 = -4\lambda_\mathrm{o}$. The other $L - 1$ eigenvalues $\alpha_1, \cdots, \alpha_{L-1}$ range from 0.2109×10^{-4} to 0.6820×10^{-4} with $\mathbf{v}_1, \cdots, \mathbf{v}_{L-1}$ being perpendicular to $\mathbf{v}_0 = \mathbf{w}_\mathrm{o}$. As $\alpha_1, \cdots, \alpha_{L-1}$ are positive, the second-order sufficient conditions for Lagrange multipliers are satisfied and the optimum window $\mathbf{w}_\mathrm{o}$ we obtained and presented in Fig. 4.4 is indeed a strict local minimizer.

In Table 4.1, we present the theoretic and simulated power variance values for different cases. We have normalized Σ^2 from (4.14) and (4.16) by multiplying it with N^4/M^2 such that the mean power of the output samples $x_0[n]$, $x_1[n]$, $\cdots$, $x_{N-1}[n]$ is 1. For the simulated power variance, we used 10^6 frames of 16-channel quadrature phase-shift keying (QPSK) symbols. We see that, as one would expect, the power variance for the optimized window is the lowest among the precoders we have discussed.

We repeated the above procedure for many random choices of $N > L > M$ (even, odd, prime and nonprime numbers were examined) and found that for all cases the second-order sufficient conditions for Lagrange multipliers are satisfied.

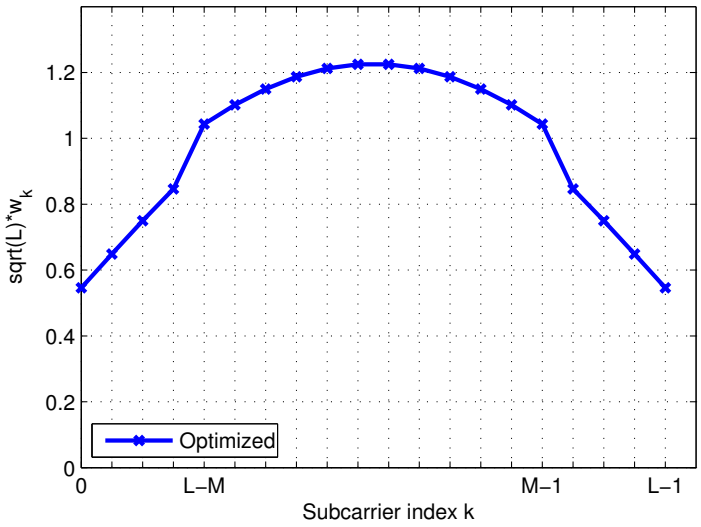

Figure 4.4: Optimized window function obtained from minimizing $\Sigma(\mathbf{w})$ with $M = 16, N = 256$ and $L = 20$.

The colormap of the optimized window is plotted in Fig. 4.5. We can see that the criteria in Section 4.3 are satisfied as the side-lobes of the Fourier transform of the optimized window are small and they do not align across the rows of $\mathbf{G}$. We can also observe from the further results presented in Fig. 4.6 that the area under the line for the power variance optimized precoder is the smallest among the precoders we have discussed so far. This confirms our choice of criteria in the discussion in Section 4.3.

From (4.14), we observe that changing the value of N does not affect the shape of the window, as the conditions in the summations only depend on M and L. Next, through a few numerical examples, we attempt to provide some insight to the effect of the parameters M and N on the shape of the window.

Starting with the above numerical example, we note that the parameters $M = 16$ and $L = 20$ correspond to an excess bandwidth of 25%. We also ran the optimization for other combinations of M and L, and presented them in Fig. 4.7:

1. The window function in cyan presents a case different from the one above, but with the same excess bandwidth 25% and compares the two windows. The new window has the parameters $M = 24$ and $L = 30$. As seen, the new window has the same "sun hat" shape. This and similar examples show that as long as the percentage amount of excess bandwidth stays the same, the shape of the window remains nearly the same. Hence, if one desires a window with other combinations of M and L, an interpolated

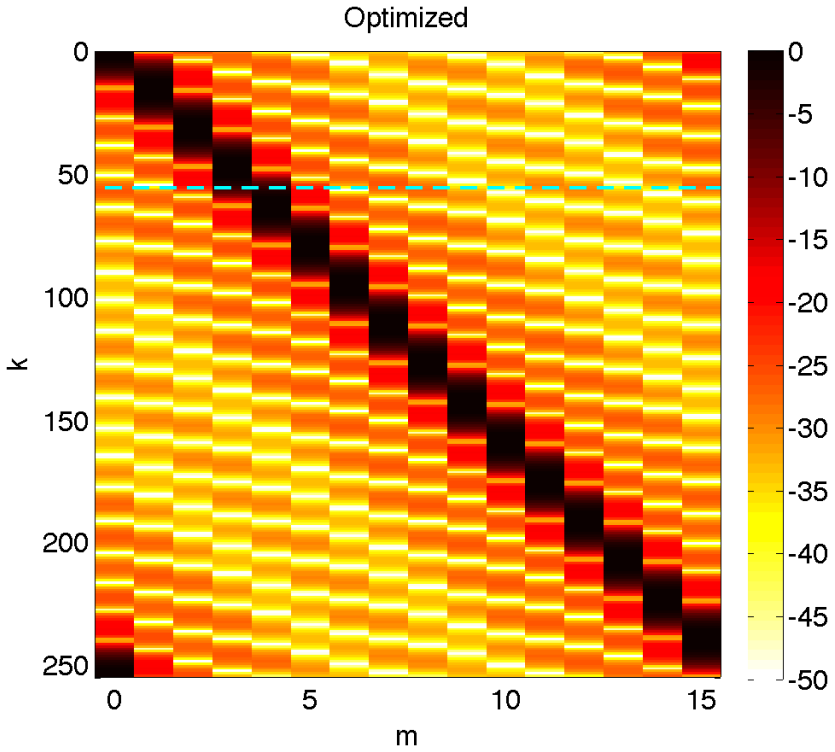

Figure 4.5: Colormap of **G** for power variance optimized precoder. Colormap scale is in dB.

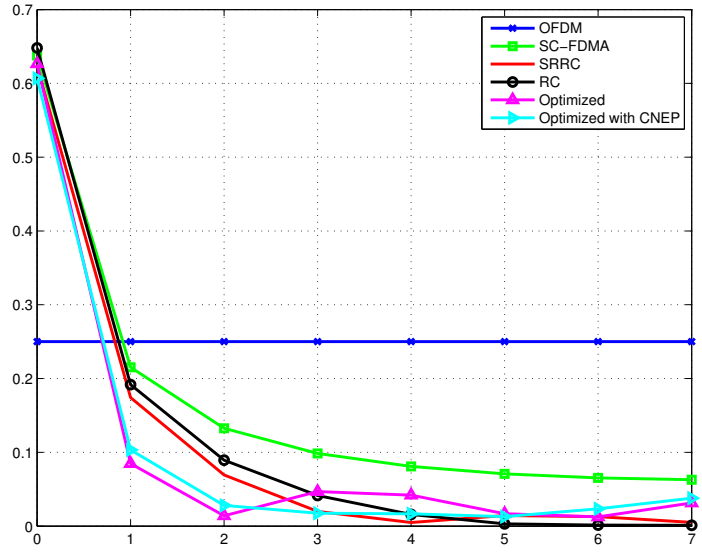

Figure 4.6: Values of $|g_{k,m}|$ along the dotted line in Fig. 4.3 (average of the two sides). The x-axis represents the number of columns away from the peak in **G**. The parameters are $M = 16$, $N = 256$, and $L = 20$ (for SRRC, RC, Optimized and Optimized with CNEP).

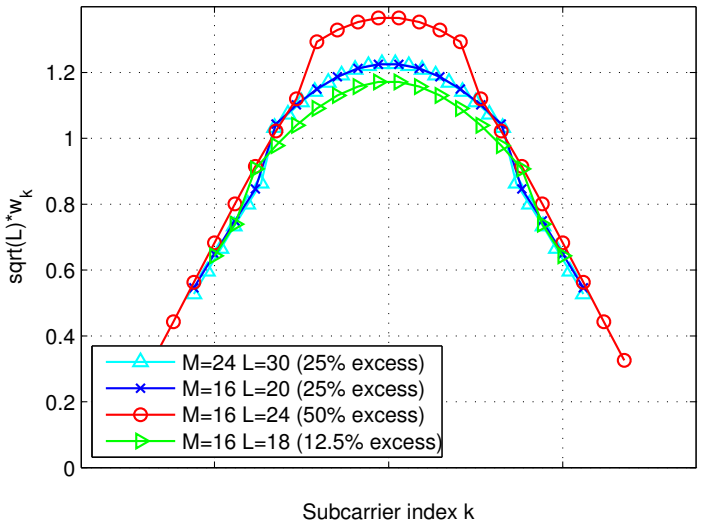

Figure 4.7: Optimized window functions with different combinations of M and L.

version of an existing window can be used, as long as the percentage amount of excess bandwidth does not change.

2. To see the effect of excess bandwidth on the shape of the "sun hat," we keep the value of $M = 16$ and check the optimized window for the values of $L = 18$ and 24 as well. The window top "bump" stay at $k = L - M$ to $k = M - 1$. Its curvature also remains (almost) unchanged. The shift in the top is to satisfy the constraint $\sum_{k=0}^{L-1} w_k^2 = 1$.

Using the gradient search method to find the optimized window for every possible combination of M and L can be a cumbersome task. One may be interested in a general formula that gives a good approximation to the optimum window for all values of M and L. Using the method of least squares on our optimized windows with different amount of excess bandwidths, we obtained the following:

$$w(x) = \begin{cases} -0.3819x^2 + 0.2769 & , |x| \leq 1 - \frac{L}{2M} \\ -0.3727\text{sgn}(x)x + 0.3398 & , \text{otherwise.} \end{cases} \tag{4.26}$$

To determine the window coefficients w_k, we first sample $w(x)$ at $x = -\frac{L-1}{2M} + \frac{k}{M}$ where $k = 0, 1, \cdots, L-1$, and then perform normalization to ensure that $\sum_{k=0}^{L-1} w_k^2 = 1$. We have compared the power variance of the approximated windows to the optimized ones, and they suffer an increase of less than 1%. Further results presented later show that the difference between the optimized and approximated designs in terms of PAPR and INP parameters are also negligible.

Numerical analyses were also performed for the case of CNEP. By trial and error we find that for the case of $M = 16, L = 20$ and $N = 256$, the value of $\gamma = 1.75 \times 10^{-6}$ leads to a good balance between the variance of the instantaneous power and the noise enhancement penalty. Fig. 4.8 (red curve) shows the values of the optimized w_k from the result of the minimization of the cost function $C(\mathbf{w})$. Fig. 4.9 and Fig. 4.10 show the CCDF of PAPR and INP in all of the discussed precoder systems using QPSK. The maximum value of $\sum_{m=0}^{M-1} |g_{k,m}|$, the PAPR and INP of the CCDF at 10^{-5} of the different systems, and Σ^2 (theoretical and simulated) are shown in Table 4.1. By comparing the columns of Table 4.1, we can confirm that the CCDF curves of each system stay below the theoretical upper limit we discussed at the end of Section 4.1. We have also calculated the CCDF of PAPR and INP for the case of quadrature amplitude modulation 16QAM, and we observed similar results that the optimized window has 1 dB improvement over the SRRC window.

To explore the accuracy of the approximation (4.26), the CCDF plots are presented in Fig. 4.11 and Fig. 4.12. The solid lines represent the optimized windows and the dashed lines represent the approximated windows using (4.26). As seen, the approximation leads to almost the same curves as those of the optimized windows. Moreover, as one would expect, increasing the amount of excess bandwidth reduces the PAPR and INP.

The optimized $\mathbf{w}$ with CNEP has a peculiar rough shape with sharp variations at a few points. This rough shape and correctly selected discontinuity points, which are found by the optimization algorithm, introduce irregularities in the locations of the associated

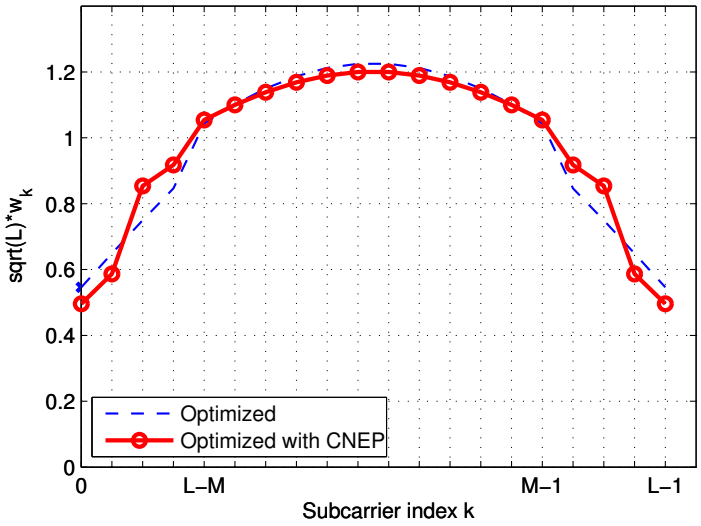

Figure 4.8: Optimized window function obtained from minimizing the cost function $C(\mathbf{w})$.

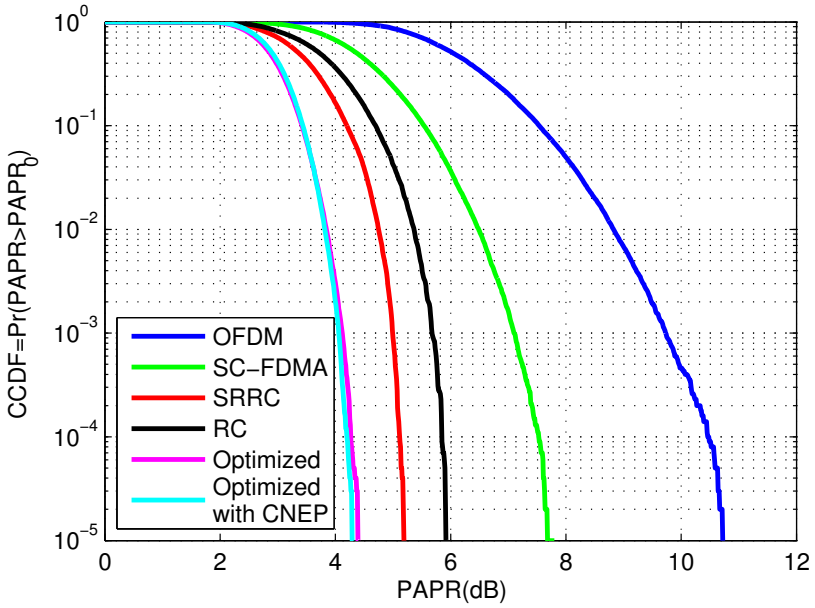

Figure 4.9: CCDF comparison of the PAPR of different systems using 10^6 frames of 16-channel QPSK symbols. $M = 16$ and $N = 256$ for all systems with $L = 20$ for SRRC, RC and Optimized (systems with nonzero excess bandwidth).

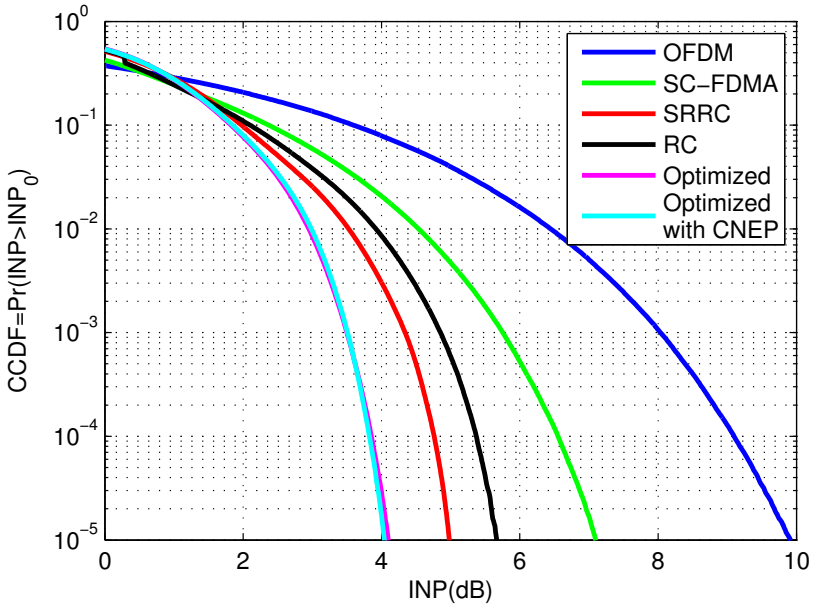

Figure 4.10: CCDF comparison of the instantaneous normalized power of different systems using 10^6 frames of 16-channel QPSK symbols. $M = 16$ and $N = 256$ for all systems with $L = 20$ for SRRC, RC and Optimized (systems with nonzero excess bandwidth).

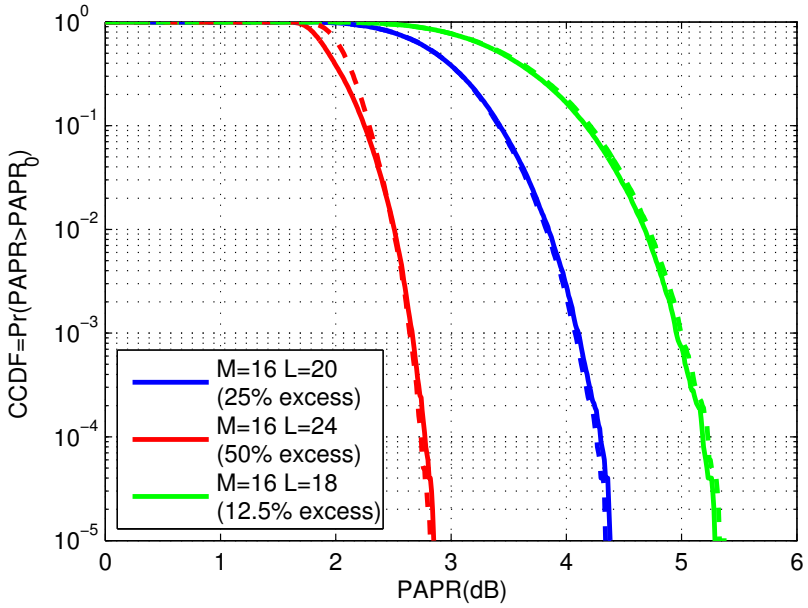

Figure 4.11: CCDF comparison of the PAPR of systems with optimized windows and different amounts of excess bandwidths using 10^6 frames of 16-channel QPSK symbols. $M = 16$ and $N = 256$ for all systems with $L = 20$, 24 and 18, respectively. Solid line: optimized using gradient search. Dashed line: approximation using (4.26).

time-domain side-lobes and these in turn avoid destructive alignment of the terms in the summation $\sum_{m=0}^{M-1} |g_{k,m}|$. We also observe that when compared to the one without CNEP, the optimized precoder with CNEP has a higher power variance (by 4%) while its PAPR and INP stay about the same (by observing the overlap of the curves in Fig. 4.9). One may argue that the PAPR, INP and power variance do not show any improvement with CNEP, however, we will see that the BER performance improves significantly with CNEP in the next paragraph. It should be also noted that although, at this time we do not have any analytical proof for the (local) optimality of the precoder with CNEP, the numerical results presented next indicate that it always converges to a near optimal solution.

A transceiver system with an AWGN channel (with white noise of power spectral density $\frac{N_0}{2}$) is simulated and the transmitted signal is amplitude adjusted (with the peak amplitude normalized to be 1) to take into consideration having an amplitude limited power amplifier. A sufficiently large number ($> 10^7$) of symbols are modulated using the transmitter of each system, and the maximum instantaneous power, which would be used as the saturation level, is recorded and the signal would be scaled accordingly. With this setup the transmitted signal should not breach the saturation level of the amplitude limited power amplifier. We would clip the signal if the instantaneous power is higher than the saturation level,

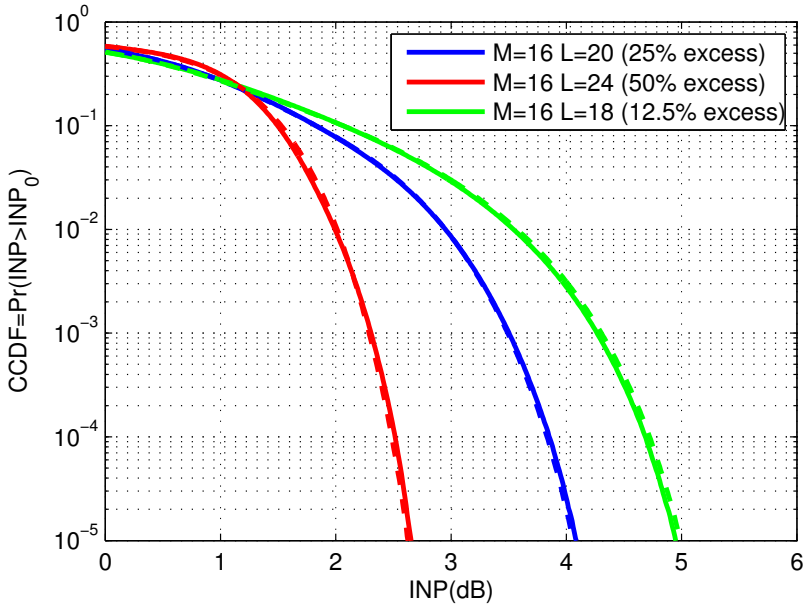

Figure 4.12: CCDF comparison of the instantaneous normalized power of systems with optimized windows and different amounts of excess bandwidths using 10^6 frames of 16-channel QPSK symbols. $M = 16$ and $N = 256$ for all systems with $L = 20$, 24 and 18, respectively. Solid line: optimized using gradient search. Dashed line: approximation using (4.26).

but it was not observed in our simulation. The results of BER performance comparison are shown in Fig. 4.13 and Fig. 4.14, using QPSK and 16QAM, respectively. For both QPSK and 16QAM, the system corresponding to the optimized window with CNEP has the lowest bit error rate. The optimized window with CNEP has only 0.2 dB (QPSK) and 0.5 dB (16QAM) improvement over the SRRC window, while the one with CNEP has about 1 dB (both) improvement over the SRRC window. The noise enhancement penalty for our optimized window with CNEP is larger than SRRC due to the nonflat top, yet it still performs better than SRRC due to the advantage of lower PAPR and power variance. We note that the x-axis in the BER results in Figs. 4.13 and 4.14 is not signal-to-noise ratio (SNR), as is usually the case. Here, because transmit signals are normalized for a peak amplitude of unity, the x-axis is $1/N_0$.

One may argue that precoders with nonzero excess bandwidth occupy extra subcarriers in the spectrum. This can be mitigated by overlapping the redundant subcarriers of different users as they will be removed at the receiver. The amount of wasted bandwidth is then reduced by half. In our example the number of redundant subcarriers is 4 out of 20. With the overlapping of the redundant subcarriers the wasted bandwidth can be reduced from

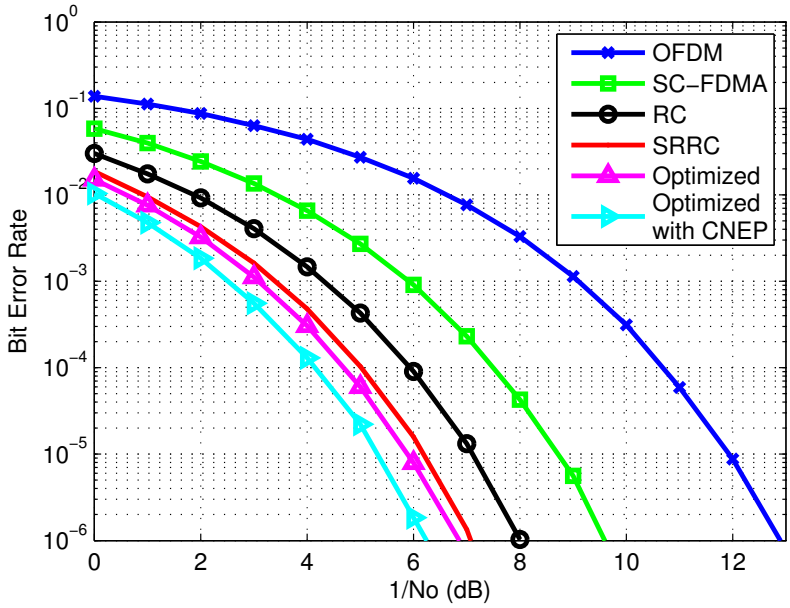

Figure 4.13: BER performance of different systems using QPSK with the same maximum saturation output power. The parameters are $M = 16, N = 256$ and $L = 20$ (for SRRC, RC and Optimized).

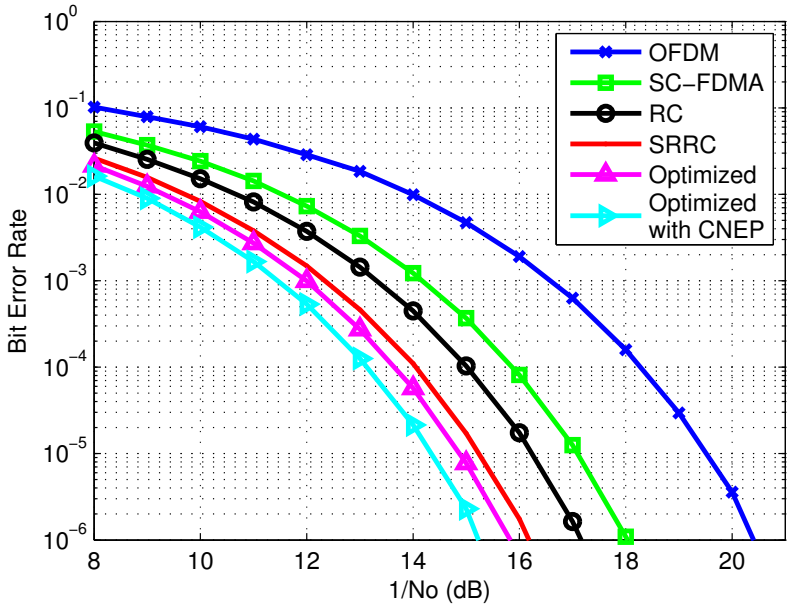

Figure 4.14: BER performance of different systems using 16QAM with the same maximum saturation output power. The parameters are $M = 16, N = 256$ and $L = 20$ (for SRRC, RC and Optimized).

20% to 10%, while the BER performance improves by 4 dB (optimized with CNEP vs SC-FDMA), which is more than the improvement from OFDM to SC-FDMA.

The optimization is customized to the configuration parameters M, L and N. One may argue that an obtained optimized window for one design is not flexible enough to cover other possible configuration parameters. We need to go through the optimization process once again for another set of parameters. However, from the BER performance curve, we see that SRRC is only 1 dB worse than optimum. Also, the flat top of SRRC ensures that the noise enhancement penalty is already small. It can be concluded that using SRRC as the window of the precoder is good enough for some applications where the simplicity of the shape of the SRRC is more valuable.

In transmission schemes with the implementation of MIMO, there are also other precoder designs for the SC-FDMA system using MMSE beamforming techniques [30]. Regular DFT precoders (no excess bandwidth) are implemented with optimization done in the beamforming filter. In the beamforming block, the optimum power allocation is calculated using the knowledge of the MIMO channel. The PAPR can be reduced by exploiting the unused degrees of freedom in designing the beamforming filter. This method is not mutually exclusively to our design, and one can replace the DFT precoder in each antenna with our optimized precoder. The beamforming filter can be adjusted accordingly. We expect the existence of excess bandwidth in our designs would further improve the PAPR in such systems as well.

CHAPTER 5

OFDM AND FBMC IN UNDERWATER ACOUSTIC CHANNELS WITH DOPPLER SCALING

In this chapter we investigate the use of nonuniform fast Fourier transform (NUFFT) in detection of multicarrier signals in underwater acoustic channels. Due to limitation of electromagnetic (EM) wave propagation in water, communication in underwater channels is established through acoustical waves. The far slower speed of the sound, as compared to EM waves, creates peculiar problems in underwater acoustic (UWA) channels that have no parallel in the EM medium. The particular problem that this dissertation aims to tackle is the impact of the mobility of the communicating vehicles on the UWA signals: *the time is scaled* by a factor equal to $1 + v(t)/c$, when the spacing between the vehicles is varied at a speed of $v(t)$ and c denotes the speed of the propagating waves. The time scaling is often referred to as *Doppler scaling*.

This point has been noted in some recent publications and active research by [31], [32] and [33] are going on to solve this challenging problem. The Doppler scaling problem has been found more damaging in communication systems that use orthogonal frequency division multiplexing (OFDM) for signal modulation [33].

In addition to OFDM, filterbank multicarrier (FBMC) techniques have been introduced to UWA communications ([38], [39], and [40]). In [40], the authors showed with real world data that FBMC has a superior performance over OFDM in doubly dispersive UWA channels. However, this study was limited to the case where Doppler scaling was absent.

In [31], [32] and [33], the authors presented several methods that allow for the estimation of the Doppler scale $v(t)/c$. In general, these methods rely on: correlation in the preamble [31]; pilot aided [31]; time duration of a packet [32]; phase tracking [33]; or location of null-subcarriers [31]. After obtaining the estimated value of the Doppler scale, resampling operation is performed to fix the time scale or, equivalently, the rate of the samples. This requires signal interpolation to a much higher rate and down sampling the result to the

desired rate. However, interpolation based methods have a couple of serious problems that render their applicability in practice limited. Firstly, the Doppler scale $v(t)/c$ is assumed fixed within each OFDM block, while in the real world $v(t)$ may change significantly within each OFDM symbol. Secondly, the interpolation accuracy during the resampling process is limited by the interpolation factor which cannot be increased arbitrarily. This is because the complexity of the resampler increases with the interpolation factor. These clearly impose serious limitations and thus new approaches should be developed.

On the other hand, the traditional method of dealing with mobility in underwater acoustic channels was to resample the signal assuming linear Doppler shift. As noted, this may not hold in practice and those methods are not applicable in the case of nonlinear Doppler scaling.

In the presence of nonlinear Doppler scaling, when the received signal is sampled at the nominal rate, the samples will be seen as unevenly spaced within the domain of transmit signal. We introduce the use of nonuniform fast Fourier transform (NUFFT) in detection of OFDM in a situation where the received signal samples are unevenly spaced. We developed the necessary equations that show how NUFFT should be applied to this application.

5.1 Doppler Scaling in Multicarrier Systems

To keep our derivations as simple as possible, the presentation in this section will be limited to one isolated multicarrier symbol, originating from OFDM or FBMC. The complex baseband signal of such a symbol in continuous time, at the transmitter, may be expressed as

$$x(t) = \sum_{k\in\mathcal{K}} s_k p(t) e^{j2\pi \frac{k}{T} t}, \tag{5.1}$$

where s_k is the data symbol on the kth subcarrier, $\mathcal{K}$ indicates the set of active subcarrierrs, T is the inverse of subcarrier spacing, and $p(t)$ is the transmit pulse-shape. In OFDM, $p(t)$ is a rectangular pulse with a duration that is the sum of the symbol period and the cyclic prefix period, while in FBMC, $p(t)$ is usually a square-root Nyquist pulse and can cover several symbol periods. The baseband signal is then modulated into passband, resulting in the transmit signal:

$$\begin{aligned} x_{\mathrm{PB}}(t) &= \Re\left\{x(t)e^{j2\pi f_c t}\right\} \\ &= \Re\left\{\sum_{k\in\mathcal{K}} s_k p(t) e^{j2\pi\left(\frac{k}{T}+f_c\right)t}\right\}, \end{aligned} \tag{5.2}$$

where $\Re\{\cdot\}$ denotes the real part of its argument.

When the signal is sent over an underwater channel, the received signal will, due to variation of the distance between transmitter and receiver, experience a time scaling effect which is expressed as $t' = (1 + \alpha(t))t$ where t is original time variable and t' is the scaled time, and $\alpha(t) = v(t)/c$. We call $(1 + \alpha(t))$ *Doppler scaling factor*. The received waveform at the receiver will then be

$$\begin{aligned} x_{\mathrm{PB}}\left(t'\right) &= \Re\left\{\sum_{k\in\mathcal{K}} s_k p\left(\left[1+\alpha(t)\right]t\right) e^{j2\pi\left(\frac{k}{T}+f_c\right)[1+\alpha(t)]t}\right\} \\ &= \Re\left\{\sum_{k\in\mathcal{K}} s_k p\left(\left[1+\alpha(t)\right]t\right) e^{j2\pi\left[\frac{(1+\alpha(t))k}{T}+(1+\alpha(t))f_c\right]t}\right\}. \end{aligned} \tag{5.3}$$

We note that the presence of a channel also introduces some additional (linear) distortion to the signal. We ignore such distortion, to keep the equations as simple as possible. Nevertheless, the results developed in this chapter are readily applicable to the cases where the channel effect is included.

We can see that the Doppler scaling factor $1+\alpha(t)$ has three main effects on the received signal: (i) it moves the center frequency from f_c to $(1 + \alpha(t))f_c$; (ii) the centers of the subcarriers will experience a frequency dependent shift from $\frac{k}{T}$ to $\frac{(1+\alpha(t))k}{T}$; and (iii) the pulse-shape $p(t)$ will be time scaled.

The first effect can be resolved relatively easily by using existing frequency offset mitigation and tracking methods. However, the second effect is much harder to deal with, since the shifts are different on different subcarriers. After demodulating the signal from passband to baseband and filtering, we have

$$r(t) = \sum_{k\in\mathcal{K}} s_k p\left(\left[1+\alpha(t)\right]t\right) e^{j2\pi\frac{(1+\alpha(t))k}{T}t}. \tag{5.4}$$

The third effect is minor and thus may be ignored.

At the receiver, the received signal $r(t)$ is sampled at the interval of nT/N. This results in signal samples

$$r_n = \sum_{k\in\mathcal{K}} s_k p\left(\frac{(1+\alpha_n)nT}{N}\right) e^{j2\pi\frac{(1+\alpha_n)k}{N}n}, \tag{5.5}$$

where $\alpha_n = \alpha(nT/N)$. One may notice that (5.5) is equivalent to sampling $x(t)$ in (5.1) at $t = \frac{(1+\alpha_n)nT}{N}$. In other words, r_n can be considered as the result of sampling $x(t)$ nonuniformly, over the time grid $t_n = \frac{(1+\alpha_n)nT}{N}$.

We will show how we can use a method called "nonuniform FFT" (NUFFT) based on [43] to extract the data symbols s_k through a clever processing of the nonuniformly sampled values of $r(t)$.

5.2 Nonuniform Fast Fourier Transform

Suppose that we are given N nonuniform samples $x(t_n)$, where $t_n = \frac{(1+\alpha_n)nT}{N}$, and we define

$$\tilde{x}(t) = \sum_{n=0}^{N-1} x(t_n)\delta(t - t_n). \tag{5.6}$$

Let $g_\tau(t)$ be a T-periodic Gaussian function with variance $\sigma^2 = 2\tau$, i.e.,

$$g_\tau(t) = \sum_{p=-\infty}^{\infty} e^{-\frac{(t-pT)^2}{4\tau}}. \tag{5.7}$$

Also, we define

$$\tilde{x}_\tau(t) = \tilde{x}(t) \star g_\tau(t) = \sum_{n=0}^{N-1} x(t_n) \left[\sum_{p=-\infty}^{\infty} e^{-\frac{(t-t_n-pT)^2}{4\tau}} \right]. \tag{5.8}$$

The key point in the development of the NUFFT is the fact that when τ is chosen properly, $\tilde{x}_\tau(t)$, within the time interval $0 \le t \le T$, is a close approximation (within a scaling factor that is introduced below) to the original signal $x(t)$. If we perform NUFFT for the segments of the received samples, each with duration T, and aggregate the results in time domain, we can recover the full original signal $x(t)$ for all t. Hence, we can extract the transmitted symbols s_k using standard OFDM and FBMC detectors.

The use of Gaussian pulse as an interpolator has two reasons. Firstly, the time-frequency isotropic property of the Gaussian pulse (i.e., the fact that the Fourier transform of a Gaussian pulse is Gaussian) is the key facilitator to the fast implementation of the NUFFT. Secondly, the Gaussian pulse $g_\tau(t)$ with a coarse choice of τ is always a very good interpolator of all choices of $x(t)$, [44].

The Fourier series coefficients of the T-periodic signal $\tilde{x}_\tau(t)$ are

$$\tilde{X}_\tau[k] = \frac{1}{T} \int_0^T \tilde{x}_\tau(t) e^{-j2\pi kt/T} dt. \tag{5.9}$$

On the other hand, using $\boldsymbol{\mathcal{F}}\{\cdot\}$ to denote Fourier transform, we recall that

$$\boldsymbol{\mathcal{F}} \left\{ e^{\frac{-t^2}{4\tau}} \right\} = 2\sqrt{\pi\tau} e^{-4\pi^2 f^2 \tau}. \tag{5.10}$$

Hence, the Fourier coefficients of the T-periodic Gaussian function $g_\tau(t)$ are

$$G_\tau[k] = \frac{2\sqrt{\pi\tau}}{T} e^{-4\pi^2 k^2 \tau/T^2}. \tag{5.11}$$

We also note that (5.8) implies $\tilde{X}_\tau(f) = \tilde{X}(f) G_\tau(f)$, which in turn leads to

$$\tilde{X}[k] = \frac{\tilde{X}_\tau[k]}{G_\tau[k]} = \frac{T e^{4\pi^2 k^2 \tau/T^2}}{2\sqrt{\pi\tau}} \tilde{X}_\tau[k]. \tag{5.12}$$

One notices that as long as $\tilde{x}_\tau(t)$ is a well interpolated version of $x(t)$ in the time interval $0 \le t \le T$, then the standard inverse fast Fourier transfrom (IFFT) of $\tilde{X}[k]$ will be very

close to $x(nT/N)$, the original signal sampled at the correct and evenly spaced intervals. We then perform this process again for the next T-duration segment and append the results to obtain a close approximate of $x(t)$ for all t.

In practice, this IFFT process can be omitted in the receiver as we need to apply FFT again to the received samples and pass the streams to the detector (for OFDM) or the analysis filterbank (for FBMC).

The evaluation of (5.9) can be performed using a numerical integration over an oversampled uniform grid. Let M be the number of samples in the interval $0 \leq t \leq T$. It has been shown in [44] that $M = 2N$ gives a sufficient accuracy. Then, we have

$$\begin{aligned}\tilde{X}_\tau[k] &= \frac{1}{T}\int_0^T \tilde{x}_\tau(t)e^{-j2\pi kt/T} \\ &\approx \frac{1}{M}\sum_{m=0}^{M-1} \tilde{x}_\tau\left(\frac{mT}{M}\right)e^{-j2\pi km/M}. \end{aligned} \tag{5.13}$$

This can be calculated by performing the M-point FFT on $\tilde{x}_\tau\left(\frac{mT}{M}\right)$ for $m = 0, \cdots, M-1$, where

$$\begin{aligned}\tilde{x}_\tau\left(\frac{mT}{M}\right) &= \sum_{n=0}^{N-1} x(t_n)\left[\sum_{p=-\infty}^{\infty} e^{-\frac{(mT/M - t_n - pT)^2}{4\tau}}\right] \\ &= \sum_{p=-\infty}^{\infty}\left[\sum_{n=0}^{N-1} x(t_n)e^{-\frac{t_n^2}{4\tau}+\frac{2mTt_n}{4M\tau}-\frac{2t_npT}{4\tau}}\right]e^{-\frac{m^2T^2}{4M^2\tau}-\frac{p^2T^2}{4\tau}+\frac{2mpT^2}{4M\tau}}, \end{aligned} \tag{5.14}$$

and, as defined earlier, $t_n = \frac{(1+\alpha_n)nT}{N}$.

5.3 Computational Complexity

After obtaining the estimate of the Doppler scaling factor, the receiver will use this information to correct the Doppler scaling effect in the signal and perform equalization. The process in interpolation based methods in the literature consists of two steps: resampling in time, and FFT. While the number of arithmetic operations required by the FFT block is proportional to $N\log(N)$, the complexity of the resampler increases with the interpolation factor. Although it is hard to give an exact figure of this complexity, as a variety of implementations are possible (with different degrees of accuracy), the complexity of this method increases proportional to

$$N \times \frac{1}{\varepsilon}, \tag{5.15}$$

where ε is a figure indicating the accuracy of the interpolation process. In our method, the Doppler scaling correction is done using only one step: the NUFFT block. The

number of arithmetic operations required by the resampling process in the NUFFT block is proportional to [44]

$$N \times \log\left(\frac{1}{\varepsilon}\right). \tag{5.16}$$

Note that if we fix the accuracy of the interpolation process to a small constant, (5.16) becomes a constant times N. For example, in order to obtain about 6 digits of accuracy, a computational cost of $12N$ and a storage cost of $12N$ are needed [43]. From the above discussion, we may conclude that while the accuracy of the method proposed in this chapter can be increased arbitrarily, as according to (5.16) it increases only with $\log(1/\varepsilon)$, the case is different from the methods proposed in the previous literature [31], [32] and [33].

5.4 Experimental Results of Doppler Scaling Correction Using NUFFT

To evaluate the performance of nonlinear Doppler scaling correction using NUFFT, we have performed simulations of an OFDM transceiver with nonlinear Doppler scaling on two scenarios: (i) an AWGN channel, and (ii) a more realistic underwater acoustic channel with a number of multipaths with Rayleigh distributed amplitudes, interarrival times of an exponential distribution, and Doppler spread due to the doubly dispersive channel. We compare the performance of the following three compensation methods:

- No Doppler scaling compensation.
- Traditional linear Doppler scaling compensation [42] by resampling the received signal $y(t)$ using

$$z(t) = y\left(\frac{1+\alpha}{1+\hat{\alpha}}t\right). \tag{5.17}$$

- Nonlinear Doppler scaling compensation using NUFFT.

In the first scenario, for comparison purposes, we use an AWGN channel with nonlinear Doppler scaling to better see the impact of the proposed NUFFT compensation of nonlinear Doppler scaling factor. The relative velocity and acceleration of the vehicles used are 10 m/s and 2 m/s^2, respectively. Fig. 5.1 shows the eye diagram of the received data symbols in one OFDM block using the three different compensation methods. As seen, with no compensation the detected symbols are badly scrambled, hence correct detection of the transmitted data symbols is unlikely. The eye pattern significantly improves and open eye is seen when a constant speed is assumed with linear Doppler scaling and compensated for. Further significant improvement is observed when the the acceleration, i.e., the first

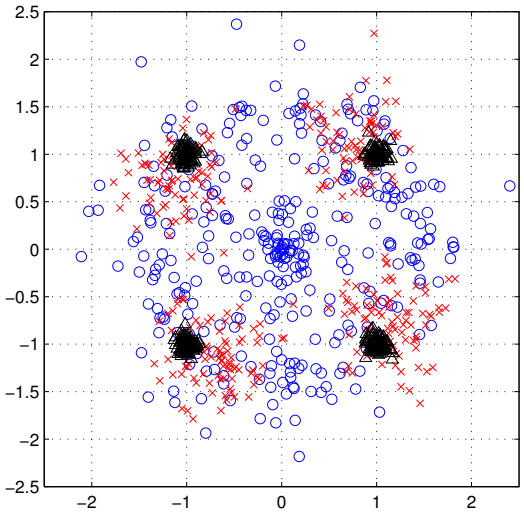

Figure 5.1: Eye diagram at the receiver with SNR = 30 dB. Compensation method: blue, none; red, linear Doppler scaling compensation through resampling (velocity only); black, nonlinear Doppler scaling compensation using NUFFT (velocity and acceleration).

derivative of $v(t)$, is also detected and compensated for using nonlinear Doppler scaling compensation with NUFFT.

In the second scenario, we use a channel model for the underwater acoustic channel similar to the one used in [42]. The channel is modeled to have 10 different multipaths. The interarrival times are generated using the exponential random variable with mean of 1 millisecond. The amplitudes of the paths are Rayleigh distributed, with an average power profile that decays exponentially from 0 dB to -20 dB. The maximum Doppler spread is selected to be $\sqrt{3}\sigma_v f_c/c$, where $\sigma_v = 0.25$ m/s is the velocity standard deviation, $f_c = 20$ kHz is the carrier frequency, and c is the speed of sound which is at 1484 m/s. Additive Gaussian noise is also added with SNR = 30 dB. The relative velocity ranges from 10 m/s to -10 m/s, and the deceleration of the vehicles used is 4 m/s^2.

We have simulated 12 OFDM packets, each with 43 blocks of OFDM symbols (with 262 usable data subcarriers), which give us 516 OFDM blocks and over 135,000 QPSK symbols. We perform Doppler scaling factor compensation with NUFFT, as well as the traditional resampling method assuming linear Doppler scaling. Afterwards, we use the pilot subcarriers inserted in the signal to perform least square estimation of the channel, and equalized it using MMSE equalization. Fig. 5.2 shows an example of the channel in time domain for a sample OFDM block. Channel equalization is done in the frequency

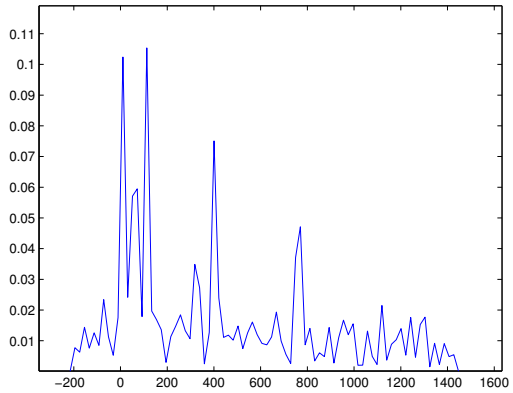

Figure 5.2: An example of the channel we obtained using least square estimation, with the noise variance measured at the pilots.

domain using the conventional single-tap per subcarrier method for OFDM.

The comparison of the mean square error for the 12 packets are summarized in Table 5.1. We can observed that with nonlinear Doppler scaling correction, the mean square error of the received data symbols are lower than the one using traditional compensation method ($\approx$ 44.2 % improvement). Of the 270384 bits transmitted, we get 26165 bit errors for the traditional method and 13064 bit errors for the NUFFT method ($\approx$ 50.1% improvement). Fig. 5.3 shows the eye diagram.

Table 5.1: Mean square error of the received data symbols after Doppler compensation and equalization.

Packet	Traditional (linear)	NUFFT (non-linear)
1	0.9901	0.5499
2	1.0029	0.5292
3	1.0251	0.4814
4	0.9482	0.5630
5	0.8594	0.4998
6	1.1369	0.5737
7	1.0005	0.5968
8	1.0461	0.5826
9	0.9031	0.5408
10	1.0596	0.6106
11	0.9859	0.6067
12	1.0374	0.5579
mean	0.9996	0.5577

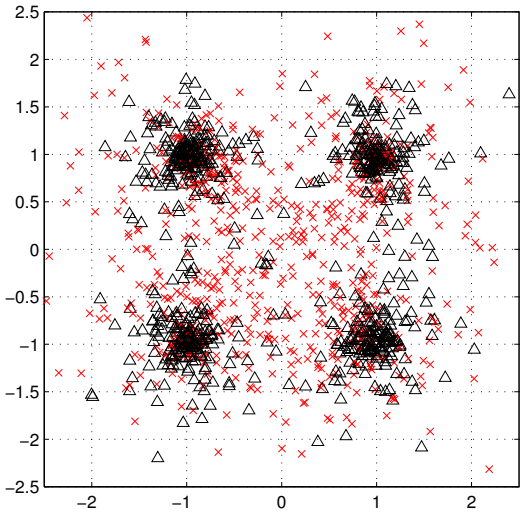

Figure 5.3: Eye diagram at the receiver with the channel and SNR = 30 dB. Compensation method: red, linear Doppler scaling compensation through resampling (velocity only); black, nonlinear Doppler scaling compensation using NUFFT (velocity and acceleration). Mean square error: red, 0.9996; black, 0.5577.

CHAPTER 6

DOPPLER SCALING FACTOR ESTIMATION AND CORRECTION[1]

In the previous chapter, we investigated the use of nonuniform fast Fourier transform (NUFFT) for compensation of Doppler scaling effects. In order to perform Doppler scaling compensation, we need to estimate the amount of Doppler scaling accurately. We will introduce a packet format that takes advantage of isolated pilots, discussed in this chapter, for detection of the Doppler scaling that has been caused due to the mobility of the communicating vehicles. Both orthogonal frequency division multiplexing (OFDM) and filterbank multicarrier (FBMC) signals are examined in an at-sea experiment using this proposed packet structure.

Our goal, in this chapter, is to validate the studies in [36] and [37] using real world at-sea experiments, and to extend the findings in [40] to UWA channels with Doppler scaling conditions. The results show that we are able to estimate and undo the effect of Doppler scaling using NUFFT and extract the data in the received signal with very low bit-error-rate (BER).

6.1 Isolated Pilot Structure for Doppler Scaling Factor Acquisition

Successful demodulation of a time-scaled multicarrier signal depends heavily on our knowledge of the Doppler scaling factor $1 + \alpha(t)$. The receiver must be able to estimate the nonlinear Doppler scaling factor accurately in order to demodulate the received signal correctly.

The kth subcarriers will experience a frequency dependent shift from $\frac{k}{T}$ to $\frac{(1+\alpha(t))k}{T}$. In order to correct the Doppler scaling factor, we need to find a method to detect how much each subcarrier has shifted from its original location in frequency.

As null subcarriers are minimally affected by the channel, the locations and energy of the null subcarriers can be used in a cost function to estimate how much the frequency spectrum of the received signal has been stretched or shrunk along the frequency domain by the effect of nonlinear Doppler scaling. We proposed a packet format in [37] such that blocks of null subcarriers are inserted around selected pilot subcarriers. To estimate the nonlinear Doppler scaling, we designed a cost function that calculates the energy of the received signal in the neighborhood of the null subcarriers. Fig. 6.1 shows a portion of the placement of 399 subcarriers. Among these, 96 are pilot subcarriers. In addition, 10 of the pilot subcarriers are isolated and placed between two groups of two or three null subcarriers. Fig. 6.2 shows an isolated pilot and its surrounding null subcarriers. These null subcarriers will increase the overhead and reduce the number of data subcarriers (from 75% to 60% of the bandwidth) if we compare it to the packet in [40].

Let us define

$$\begin{aligned} S_{\text{IP}} &= \{\text{subcarrier indices of isolated pilots}\} \\ S_{\text{null}} &= \{\text{subcarrier indices of null subcarriers}\} \end{aligned}$$

and assume a nonlinear Doppler scaling factor model with relative velocity $v(t) = v_0 + \gamma t$, which is the case of a constant acceleration or deceleration. It leads to nonlinear Doppler scaling as the the Doppler scaling factor changes within the duration T. For each α_k, we have $\alpha_k = (v_0 + \gamma kT/N)/c$, which implies it depends on the two parameters v_0 and γ. We designed a cost function $\xi(v_0, \gamma)$ that calculates the energy difference between the isolated pilots and the null subcarriers:

$$\xi(v_0, \gamma) = \sum_{k \in S_{\text{null}}} E\left[\left|\tilde{X}_\tau[k]\right|^2\right] - \sum_{k \in S_{\text{IP}}} E\left[\left|\tilde{X}_\tau[k]\right|^2\right] \tag{6.1}$$

where $\tilde{X}_\tau[k]$ was defined in the previous chapter in (5.13), which is the NUFFT output of the received samples.

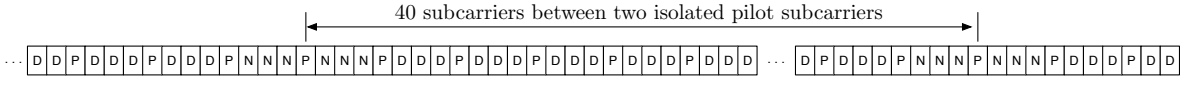

Figure 6.1: Subcarrier placement. P: pilot subcarriers (96 in total, with 10 of them as isolated subcarriers); D: data subcarriers (243 in total); N: null subcarriers (60 in total).

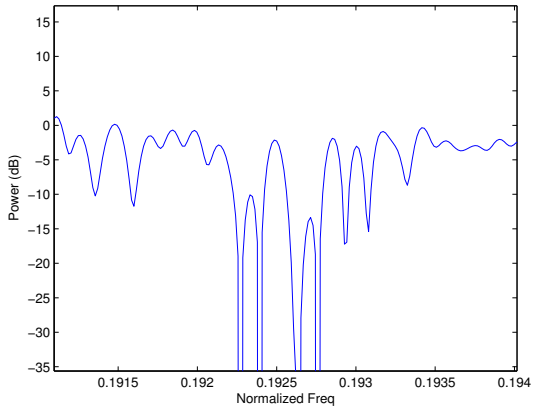

Figure 6.2: An isolated pilot and the surrounding two groups of two null subcarriers in the frequency domain.

To find the estimated values of v_0 and γ, we find

$$(\hat{v}_0, \hat{\gamma}) = \arg\min_{v_0,\gamma} \xi(v_0, \gamma) \tag{6.2}$$

using the method of steepest descent, that is,

$$\hat{v}_0^{(n+1)} = \hat{v}_0^{(n)} - \frac{\mu_1}{2\epsilon_1}\left[\xi(\hat{v}_0^{(n)} + \epsilon_1, \hat{\gamma}^{(n)}) - \xi(\hat{v}_0^{(n)} - \epsilon_1, \hat{\gamma}^{(n)})\right] \tag{6.3}$$

$$\hat{\gamma}^{(n+1)} = \hat{\gamma}^{(n)} - \frac{\mu_2}{2\epsilon_2}\left[\xi(\hat{v}_0^{(n)}, \hat{\gamma}^{(n)} + \epsilon_2) - \xi(\hat{v}_0^{(n)}, \hat{\gamma}^{(n)} - \epsilon_2)\right] \tag{6.4}$$

with some selected values of $\mu_1, \mu_2, \epsilon_1, \epsilon_2$.

In practice we can further simplify the process of optimizing $\xi(v_0, \gamma)$ by noticing that the velocity function $v(t)$ is correlated to reduce the degree of freedom of the cost function. Consider the velocity at the middle of an OFDM or FBMC symbol in time, $v_{\text{mid}} = v_0 + \gamma T/2$. Then we have $\alpha_k \approx v_{\text{mid}}/c$ and

$$\xi(v_{\text{mid}}) = \sum_{k\in S_{\text{null}}} E\left[\left|\tilde{X}_\tau[k]\right|^2\right] - \sum_{k\in S_{\text{IP}}} E\left[\left|\tilde{X}_\tau[k]\right|^2\right] \tag{6.5}$$

$$\hat{v}_{\text{mid}} = \arg\min_{v_{\text{mid}}} \xi(v_{\text{mid}}), \tag{6.6}$$

and, similarly, $\hat{v}_{\text{mid}}$ can be estimated using the method of steepest descent.

Let b be the block number in the packet, then we can estimate, for block b, the values of $v_{0,b}$ and γ_b using

$$\hat{v}_{0,b} \approx [\hat{v}_{\text{mid},b-1} + \hat{v}_{\text{mid},b}]/2 \tag{6.7}$$

$$\hat{\gamma}_b \approx [\hat{v}_{\text{mid},b} - \hat{v}_{\text{mid},b-1}]/T. \tag{6.8}$$

In other words, we estimate only the velocity in the middle of each OFDM or FBMC symbol and compute the initial velocity and the acceleration by linear interpolation. This works because the acceleration in the packet, while being nonzero, should not change too much from one symbol to the next one. In our experiment, which we will discuss in Sec. 6.3, we observed that this estimation of $\hat{v}_0$ can be off slightly due to the effect of the frequency dispersive channel, and we adjusted it using decision directed tracking methods.

The algorithm in (6.7) and (6.8) is performed along the packet. The timing phase and the duration of each symbol is calculated using the estimated information of $v(t)$. In each symbol, the values of $\hat{v}_0$ and $\hat{\gamma}$ are used to calculate $\hat{\alpha}_k = (\hat{v}_0 + \hat{\gamma} kT/N)/c$ for the input of NUFFT introduced in the previous chapter, and thus we can obtain the data symbol s_k.

6.2 Test of Doppler Scaling Acquisition and Correction

Before using the proposed packet structure designed for the real world test, we did an initial test of the performance of the method using the obtained data from the experimental results from ACOMM10, an at-sea experiment which took place on the continental shelf off the coast of New Jersey, during June 2010. Packets of OFDM were transmitted over underwater acoustic channels. The subcarrier placement is configured in a way that in a total of 399 subcarriers, 19 of them are null subcarriers. These null subcarriers allow us to estimate α using the method of steepest descent, introduced previously. The details of the configuration of the transceiver system are presented in [35].

Fig. 6.3 shows the frequency domain of the preamble part of the transmitted (blue) and the received (red) signal from the experiment. If we look at Fig. 6.4, the zoomed-in version of Fig. 6.3, the subcarriers with high subcarrier indices k misalign with the ones in the transmitted signal. This is due to the frequency dependent shifts in Doppler scaling over the underwater acoustic channel.

To correct the effect of the Doppler scaling, we used (6.3) to estimate the value of α and correct the received signal using NUFFT. We assumed the model of $v(t)$ to be a constant. Fig. 6.5 shows the result. The zoomed in version of the results are presented in Fig. 6.6. As we can see, the Doppler scaling corrected (back) signal has subcarrier peaks aligned with the ones in the transmitted signal in all the subcarriers. This confirms that our method of NUFFT is able to correct the effect of Doppler scaling.

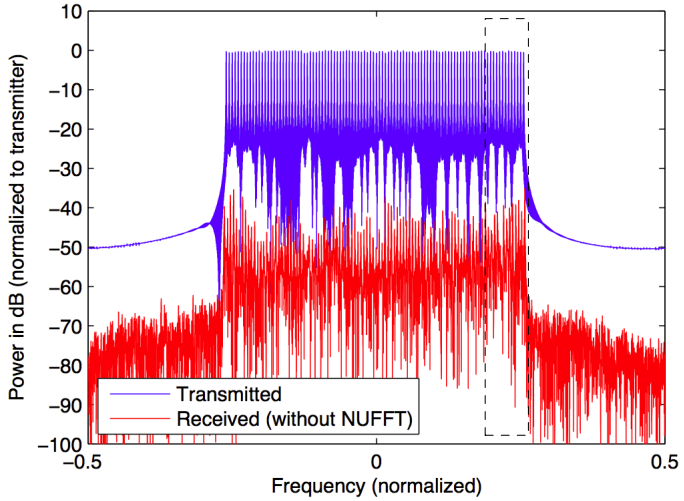

Figure 6.3: Preamble part of the transmitted signal and the received signal before Doppler scaling correction using NUFFT.

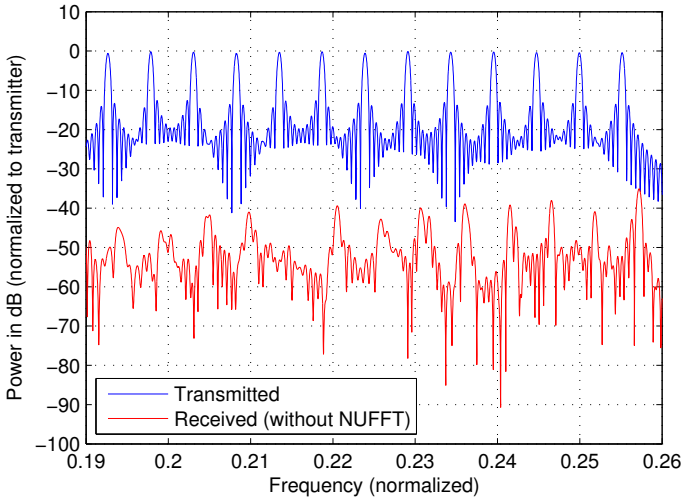

Figure 6.4: Zoomed-in version of Fig. 6.3.

6.3 At-sea Experiment

An at-sea experiment was conducted in October 2013 using an underwater audio transmitter that was deployed from a ship and an array of recorder receivers below a buoy. Fig. 6.7 shows the experimental setup [41]. FBMC and OFDM packets with a center frequency of 13.25 kHz and 5kHz bandwidth were sent over a UWA channel to an array of 4 receivers sampling at the frequency of 100 kHz at a recorder buoy. A total of 9 OFDM packets and 9 FBMC packets were tested, and they were generated using the pilot structure

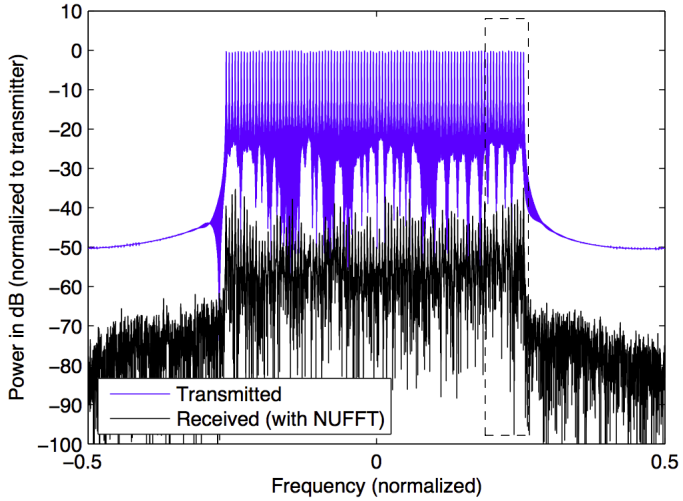

Figure 6.5: Preamble part of the transmitted signal and the received signal after Doppler scaling correction using NUFFT.

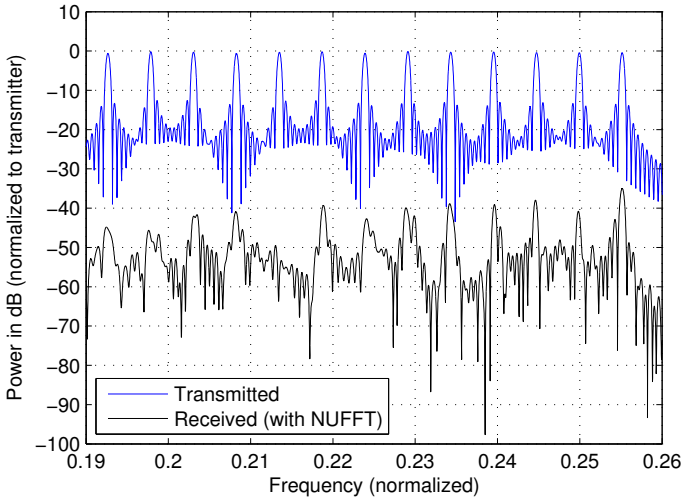

Figure 6.6: Zoomed-in version of Fig. 6.5.

described in Section 6.1, with 56 OFDM symbols and 56 FBMC symbols in each packet. Different packets consist of different QAM sizes (QPSK, 8PSK, or 16QAM) and channel coding methods (simple convolutional code or Turbo code, both at the rate of 1/2). In the case of FBMC, the prototype filter used is based on the one in [40], which was designed for doubly dispersive UWA channels. The distance between the transmitter and the receiver array varied from 500 m to 2500 m, with both of them at the depth of 25 ft and also 25 ft above the sea-bed. The transmitter was towed towards and away from the receiver array

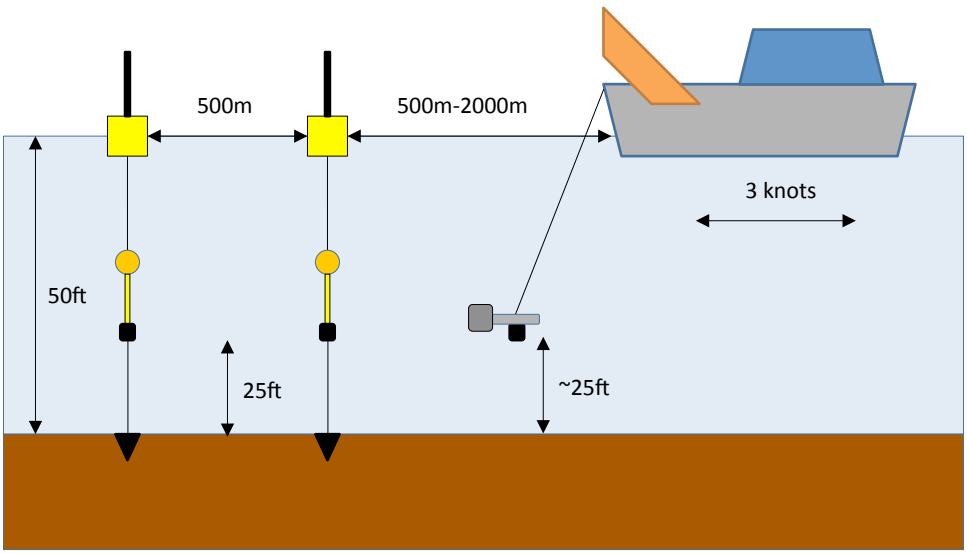

Figure 6.7: The experimental setup showing the equipment placement and movement. This image was created in collaboration with James Preisig and Keenan Ball from Woods Hole Oceanographic Institution and Chung Him Yuen and Behrouz Farhang from the University of Utah.

at the relative speed of about 3 knots, and a total of 4 tests were performed for each packet in the experiment.

Fig. 6.8 shows an example of the received UWA signal in the frequency domain from the experiment. As we have 1 transmitter element and 4 receiver elements, the method of maximum ratio combining (MRC) was used across the receiver. Table 6.1 shows the results, and we confirm that we can correctly detect and correct the Doppler scaling factor using our pilot structure with our algorithm. Fig. 6.9 shows one of the isolated pilot subcarriers in the received signal and how NUFFT corrects the effect of Doppler scaling, and Fig. 6.10 shows an example eye diagram of a Doppler scaling corrected 8PSK OFDM symbol. In our received signal, the estimation of the Doppler scaling factor, corresponds to a relative speed that varied between 1.25 m/s to 1.60 m/s, and we observed acceleration and deceleration in the duration of some of the packets.

We note that while both OFDM and FBMC have very low bit error rates, FBMC has a better performance than OFDM in terms of mean square error. The prototype filter for FBMC is designed for a doubly dispersive UWA channel, and if there is a slight offset in the detection and correction of the Doppler scaling factor the filter can minimize the effect of intercarrier interference. This is similar to what was observed in [40], in which FBMC outperforms OFDM.

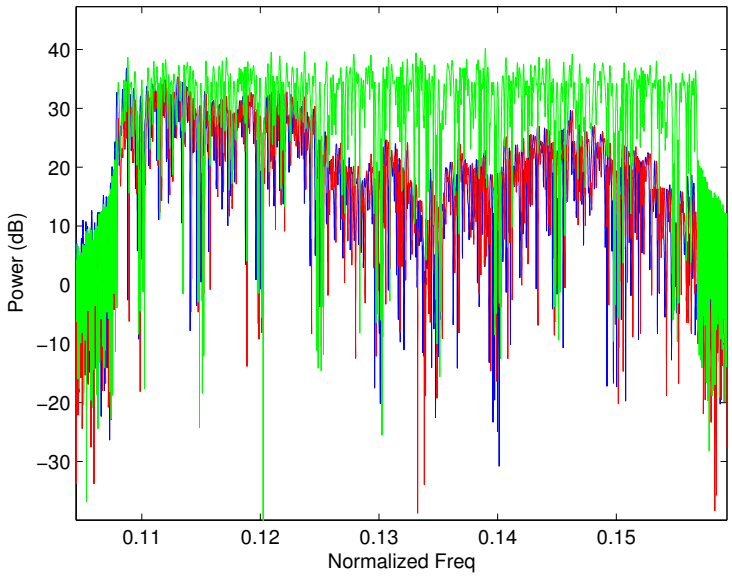

Figure 6.8: An example of the received UWA signal in the frequency domain recorded in the at-sea experiment. Blue: before NUFFT Doppler scaling correction; red: after NUFFT Doppler scaling correction; green: transmitted signal.

Table 6.1: At-sea experiment results after performing Doppler scaling detection and correction using NUFFT.

Mod Scheme	Coding	BER (OFDM)	MSE (OFDM)	BER (FBMC)	MSE (FBMC)
4PSK	Conv.	0	0.0657	0	0.0403
8PSK	Conv.	0	0.0696	0	0.0485
16QAM	Conv.	0.0309	0.0695	0.0137	0.0508
4PSK	Turbo	0	0.0517	0	0.0481
8PSK	Turbo	0	0.0819	0	0.0459
16QAM	Turbo	0	0.0562	0	0.0383

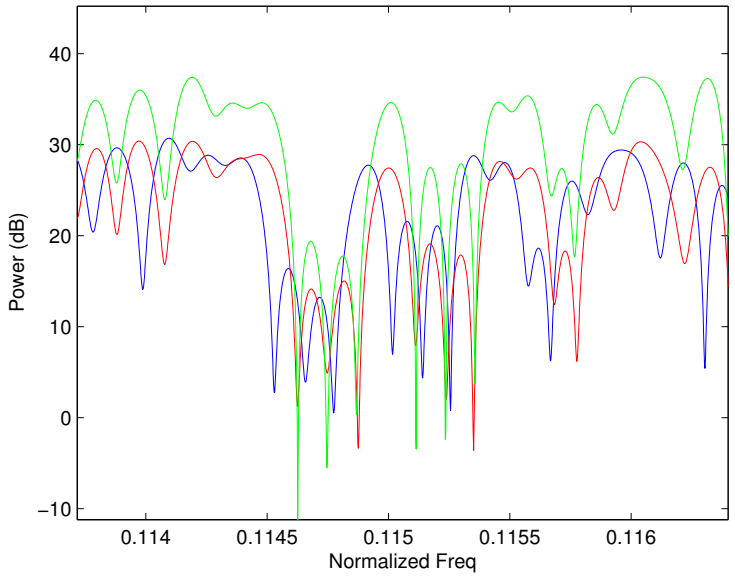

Figure 6.9: An isolated pilot in the received signal from the at-sea experiment. Blue: before NUFFT Doppler scaling correction; red: after NUFFT Doppler scaling correction; green: transmitted signal.

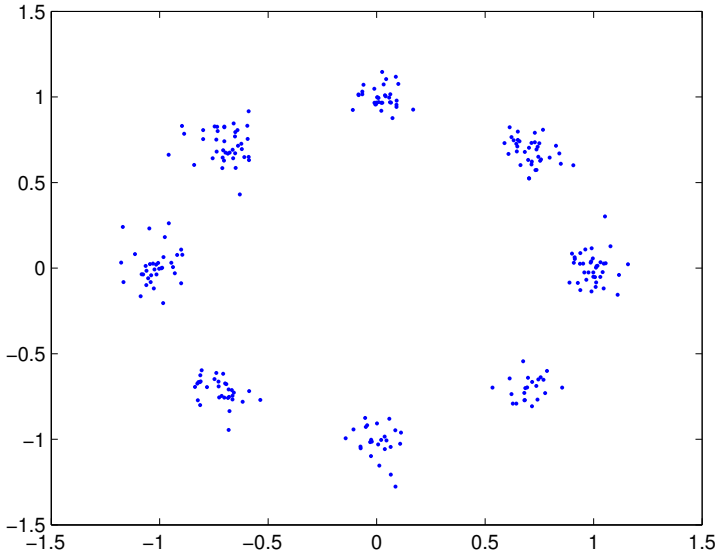

Figure 6.10: An example of an eye diagram of an 8PSK OFDM symbol after the NUFFT Doppler scaling correction.

We have also observed that there is inconsistency in the MSE and we suggest that this is due to the signal being affected by significant, but occasional, distortions in the recording process. While we removed the noticeably affected symbols from our calculations presented in Table 6.1, this may still have an impact on the MSE of the results.

In this chapter, we examined the application of a packet format that we introduce for Doppler scaling estimation in multicarrier signals. Both OFDM and FBMC signals were examined in an at-sea experiment and we investigated the use of nonuniform fast Fourier transform (NUFFT) for compensation of Doppler scaling effects. The proposed packet format takes advantage of the isolated pilots that are introduced for detection of the Doppler scaling that has been introduced due to the mobility of the communicating vehicles. Using the results from the at-sea experiment, we showed the effectiveness of the proposed packet format for estimating the Doppler scaling parameters and their compensation through NUFFT.

CHAPTER 7

CONCLUSIONS AND FUTURE RESEARCH

The high demand for broadband communications has led to the use of multicarrier techniques in RF and underwater channels, and the use of FBMC techniques can improve the performance of these transceiver systems. In this dissertation we focused on the use of FBMC techniques in several different applications. Some advancements related to OFDM have also been made.

We analyzed mathematically the timing and carrier offset sensitivity for SMT and CMT systems. Using closed form equations, we identified the signal to interference ratios in these systems. By understanding the timing and carrier offset sensitivity of these two FBMC systems, we showed that there is a simple relationship between SMT and CMT and we propose a novel method of how one can be transformed into the other one with the multiplication of a complex sine wave.

We presented a novel formulation of SC-FDMA, which is a special form of OFDM signaling, for the uplink of multiple access networks in the 3GPP LTE radio standard. We explored possible mimicking of the DFT precoding method for FBMC and investigated the direct application of SC-FDMA to FBMC systems. We compared the results with a single carrier SMT system and showed how FBMC can reduce the PAPR significantly over SC-FDMA, even without the precoder.

We investigated the use of DFT precoders with window functions having roll-off edges in SC-FDMA, and developed further analysis of SC-FDMA that explains the reasons behind why the conventional SC-FDMA precoding with a rectangular window has inferior performance to the cases where a window function with smoothly roll-off edges is used. Several different prototype filters used commonly in FBMC systems are applied as the window function in the precoder and the PAPR performance is investigated and compared to conventional SC-FDMA. Closed form equations are developed to find the upperbounds for the PAPR of these systems.

Using the minimization of the variance of the instantaneous power of the output signal of the transmitter as a means of reducing PAPR to near its minimum value, we developed a mathematical procedure to search for an optimal window that minimizes the PAPR. We formulated the problem in the form of a method of Lagrange multipliers and analyzed its second-order conditions to confirm analytically that the optimal window is indeed a strict local minimizer. We also analyzed and compensated the noise enhancement penalty of the optimal window. Our analysis also led us to find new window functions that further reduce the PAPR and improve the BER performance.

We investigated the use of OFDM and FBMC systems for underwater acoustic channels with Doppler scaling where the communicating vehicles are moving. We showed how the existence of Doppler scaling leads to unevenly spaced sampling in the receiver. We introduced the use of nonuniform fast Fourier transform (NUFFT) in detection of multicarrier signals in the presence of Doppler scaling in which the received samples are unevenly spaced. We showed how NUFFT could be implemented using numerical approximation methods and presented the equations for the procedure.

We presented a method of Doppler scaling estimation by using a novel pilot structure in which isolated pilot subcarriers are inserted in an OFDM or FBMC underwater acoustic signal. A gradient search method was proposed to perform acquisition and tracking of the Doppler scaling factor using NUFFT. We showed how our estimation method performs better than traditional resampling in both linear and nonlinear Doppler scaling. We developed the necessary equations that show how NUFFT should be applied to undo the effect of Doppler scaling, if the amount of Doppler scaling is known to us. Using both software simulation and real world at-sea experimental results, we showed how our novel method is able to estimate and correct the effect of Doppler scaling in UWA channels. Furthermore, we showed that, in UWA channels, FBMC performs better than OFDM in terms of mean square error of the detected data symbols.

7.1 Outlook of Future Research

From this research one can conclude that the use of FBMC techniques improves the performance of applications in broadband communications. The work in this dissertation can be considered as a starting point for many other challenging problems in development of FBMC techniques for other problems in broadband communications.

7.1.1 LTE Uplink with True FBMC Structures

We explored possible mimicking of the DFT precoding method for FBMC and investigated the direct application of SC-FDMA to FBMC systems, but the PAPR performance did not improve. Instead of replacing the SC-FDMA structures with FBMC systems, we applied FBMC techniques to the precoders by the use of window functions having roll-off edges to reduce the PAPR of the transmitted signal. This still does not allow us to remove the cyclic prefix (CP) in the signal, like what one can do in SMT or CMT systems. The existence of CP reduces the data efficiency. Design of FBMC systems with comparable PAPR to SC-FDMA for LTE uplink needs more investigation.

7.1.2 MIMO in UWA Channels with Doppler Scaling

We investigated the use of OFDM and FBMC systems for underwater acoustic channels with Doppler scaling where the communicating vehicles are moving. In our system, a single transmitter was used to transmit the signal to the multiple receivers. To increase the data rate, multiple-input multiple-output (MIMO) systems can be used. Doppler effect scaling may be different for different paths of the channel in a MIMO system. Design of algorithms to perform data symbol detection in such a system can be investigated.

7.1.3 Application of FBMC to Massive MIMO

Massive MIMOs, in which dozens or even hundreds of antennas are used at the same transmitter or receiver, have recently been proposed to increase the network capacity in the fifth generation of wireless communication systems. The use of FBMC in this application has also been proposed, [45] and [46]. In these papers, the authors have identified the advantages of FBMC over OFDM in the application of massive MIMO. For example, the absence of cyclic prefix in FBMC increases the bandwidth efficiency and FBMC's property of self-equalization can improve the issue of complexity, carrier frequency offset sensitivity, PAPR, and latency. On top of this, an extension of massive MIMO to underwater acoustic systems is a timely research topic that should be pursued.

REFERENCES

[1] R. Van Nee, and R. Prasad, *OFDM for Wireless Multimedia Communications.* Boston, MA: Arthec House, 2000.

[2] Y. Li and G. L. Stüber, Eds., *Orthogonal Frequency Division Multiplexing for Wireless Communications.* New York, NY: Springer, 2006.

[3] *Air Interface for Fixed and Mobile Broadband Wireless Access Systems.* IEEE Std. 802.16e, 2005.

[4] M. Morelli, C. C. Jay Kuo, and M. O. Pun, "Synchronization techniques for orthogonal frequency division multiple access (OFDMA): A tutorial review," *Proceedings of IEEE,* vol. 95, no. 7, July 2007, pp. 1394-1427.

[5] B. Farhang-Boroujeny and R. Kempter, "Multicarrier communication techniques for spectrum sensing and communication in cognitive radios," *IEEE Communications Magazine, Special Issue on Cognitive Radios for Dynamic Spectrum Access,* vol. 46, no 4, April 2008, pp. 80-85.

[6] R.W. Chang, "High-speed multichannel data transmission with bandlimited orthogonal signals," *Bell Sys. Tech. J.,* vol. 45, pp. 1775-1796, Dec. 1966.

[7] B.R. Saltzberg, "Performance of an efficient parallel data transmission system," *IEEE Trans. on Comm. Tech.,* vol. 15, no. 6, pp. 805-811, Dec. 1967.

[8] B. Hirosaki, "An orthogonally multiplexed QAM system using the discrete Fourier transform," *IEEE Transactions on Communications*, vol. 29, no. 7, pp. 982 - 989, Jul 1981.

[9] G. Cherubini, E. Eleftheriou, and S. Olcer,"Filtered multitone modulation for VDSL," in *Proc. IEEE Globecom '99,* vol. 2, 1999, pp. 1139-1144.

[10] P. Amini and B. Farhang-Boroujeny, "Packet format design and decision directed tracking methods for filter bank multicarrier systems," *EURASIP Journal on Advances in Signal Processing,* vol. 2010, article no. 7, January 2010.

[11] D. Tse and P. Viswanath, *Fundamentals of Wireless Communication.* Cambridge, MA: Cambridge University Press, 2004.

[12] C. Lélé , P. Siohan, R. Legouable, and M. Bellanger, "OFDM/OQAM for spread spectrum transmission," in *Proceedings of the International Workshop on Multi-Carrier Spread-Spectrum (MCSS '07),* Herrsching, Germany, May 2007.

[13] B. Farhang-Boroujeny, *Signal Processing Techniques for Software Radios, 2nd Edition.* Self published at Lulu publishing house, July 2010.

[14] G., Berardinelli, L.A. Ruiz de Temino, S. Frattasi, M. Rahman, and P. Mogensen, "OFDMA vs. SC-FDMA: Performance comparison in local area imt-a scenarios," *IEEE Wireless Communications,* vol. 15, no. 5, pp. 64 - 72, Oct. 2008.

[15] G. Huang, A. Nix, and S. Armour, "Impact of radio resource allocation and pulse shaping on PAPR of SC-FDMA signals," *IEEE 18th International Symposium on Personal, Indoor and Mobile Radio Communications, PIMRC 2007,* pp. 1 - 5, 2007.

[16] M. Rinne, M. Kuusela, E. Tuomaala, P. Kinnunen, I. Kovacs, K. Pajukoski, and J. Ojala, "A performance summary of the evolved 3G (E-UTRA) for voice over internet and best effort traffic," *IEEE Transactions on Vehicular Technology,* vol. 58, no. 7, pp. 3661 - 3673, Sept. 2009.

[17] *Evolved Universal Terrestrial Radio Access (E-UTRA): Physical channels and modulation (Rel-8).* 3rd Generation Partnership Project (3GPP) standard, http://www.3gpp.org/ftp/Specs/html-info/36211.htm, Dec. 2008

[18] S.B. Slimane, "Reducing the peak-to-average power ratio of OFDM signals through precoding," *IEEE Transactions on Vehicular Technology,* vol. 56, no. 2, pp. 686 - 695, March 2007.

[19] T. Ihalainen, A. Viholainen, T. H. Stitz, M. Renfors, and M. Bellanger, "Filter bank based multi-mode multiple access scheme for wireless uplink," *Proceedings of the 17th European Signal Processing Conference,* Aug. 24-28, Glascow, Scotland, pp. 1354-1358.

[20] P.P. Vaidyanathan, *Multirate Systems and Filter Banks.* Englewood Cliffs, NJ: Prentice Hall, 1993.

[21] B. Farhang-Boroujeny, "A square-root Nyquist (M) filter design for digital communication systems," *IEEE Trans. on Signal Proc.,* vol. 56, no. 5, May 2008, pp. 2127-2132.

[22] B. Farhang-Boroujeny and C.H. (George) Yuen, "Cosine modulated and offset QAM filter bank multicarrier techniques: A continuous-time prospect," *Eurasip Journal on Advances in Signal processing, Volume 2010, Special Issue on Filter Banks for Next-Generation Multicarrier Wireless Communications,* article id 165654, 2010.

[23] C. H. (George) Yuen, P. Amini and B. Farhang-Boroujeny, "Single carrier frequency division multiple access (SC-FDMA) for filter bank multicarrier communication systems," *Cognitive Radio Oriented Wireless Networks and Communications (CROWNCOM), 2010 Proceedings of the Fifth International Conference on,* 9-11 June 2010.

[24] C. H. (George) Yuen and B. Farhang-Boroujeny, "Analysis and optimization of PAPR in SC-FDMA systems," *Proceedings of the 8th International Conference on Information and Communications Security,* ICICS 2011, Singapore, December 2011.

[25] C. H. (George) Yuen and B. Farhang-Boroujeny, "Analysis of the optimum precoder in SC-FDMA," *Wireless Communications, IEEE Transactions on,* vol. 11, no. 11, pp. 4096-4107, November 2012.

[26] D. Falconer, "Linear precoding of OFDMA signals to minimize their instantaneous power variance," *IEEE Transactions on Communications,* vol. 59, no. 4, pp.1154-1162, April 2011.

[27] S.B. Slimane, "Reducing the peak-to-average power ratio of OFDM signals through precoding," *IEEE Transactions on Vehicular Technology,* vol. 56, no. 2, pp. 686 - 695, March 2007.

[28] H. G. Myung, J. Lim and D. J. Goodman, "Single carrier FDMA for uplink wireless transmission," *Vehicular Technology Magazine, IEEE* , vol.1, no.3, pp.30-38, Sept. 2006

[29] E. K. P. Chong and S. H. Zak, *An Introduction to Optimization, 2nd Edition.* New York, NY: Wiley-Interscience, 2001.

[30] U. Dang, M. Ruder, R. Schober, W. Gerstacker, "MMSE beamforming for SC-FDMA transmission over MIMO ISI channels," *EURASIP J. Advances in Signal Processing, Volume 2011,* 2011.

[31] Lei Wan, Zhaohui Wang, Shengli Zhou, T. C. Yang, and Zhijie Shi, "Performance comparison of Doppler scale estimation methods for underwater acoustic OFDM," *Journal of Electrical and Computer Engineering,* vol. 2012, article id 703243, 2012.

[32] Baosheng Li, Shengli Zhou, M. Stojanovic, L. Freitag, and P. Willett, "Multicarrier communication over underwater acoustic channels with nonuniform Doppler shifts," *Oceanic Engineering, IEEE Journal of,* vol. 33, no. 2, pp.198-209, April 2008.

[33] M. Stojanovic, "Low complexity OFDM detector for underwater acoustic channels," *OCEANS 2006,* pp.1-6, 18-21 Sept. 2006

[34] L. Greengard and J.Y. Lee, "Accelerating the nonuniform fast Fourier transform," *SIAM Rev.,* vol. 46, no. 3, pp. 443-454, 2004.

[35] P. Amini, Rong-Rong Chen; B. Farhang-Boroujeny, "Filterbank multicarrier for underwater communications," *Communication, Control, and Computing (Allerton), 2011 49th Annual Allerton Conference on,* pp.639-646, 28-30 Sept. 2011. doi: 10.1109/Allerton.2011.6120228

[36] C. H. Yuen, B. Farhang-Boroujeny, "Doppler scaling correction in OFDM," *Communications (ICC), 2013 IEEE International Conference on,* 9-13 June 2013.

[37] C. H. Yuen and B. Farhang-Boroujeny, "Non-linear Doppler scaling correction in underwater acoustic channels: Analysis and simulation," *Oceans '13 MTS/IEEE San Diego Conference,* pp.1-7, 23-27 Sept. 2013.

[38] J. Gomes and M. Stojanovic, "Performance analysis of filtered multitone modulation systems for underwater communication," in *Proc. MTS/IEEE OCEANS Conf. Marine Technology for Our Future: Global and Local Challenges,* 2009.

[39] S. J. Hwang and P. Schniter, "Efficient multicarrier communication for highly spread underwater acoustic channels," *IEEE J. Sel. Areas Commun.,* vol. 26, no. 9, pp. 1674-1683, Dec. 2008.

[40] P. Amini, R. R. Chen, and B. Farhang-Boroujeny, "Filterbank multicarrier communications for underwater acoustic channels," *Oceanic Engineering, IEEE Journal of ,* no. 99, pp. 1-16, 2013.

[41] C. H. Yuen and B. Farhang-Boroujeny, "Pilot structure for Doppler scaling estimation in multicarrier communications," *IEEE Sponsored Underwater Communications Networking Conference (UComms 2014),* Italy, Sept. 2014

[42] S.F. Mason, C.R. Berger, S. Zhou, and P. Willett, "Detection, synchronization, and Doppler scale estimation with multicarrier waveforms in underwater acoustic communication" *Selected Areas in Communications, IEEE Journal on ,* vol.26, no.9, pp. 1638-1649, December 2008.

[43] L. Greengard and J.Y. Lee, "Accelerating the nonuniform fast Fourier transform," *SIAM Rev.,* vol. 46, no. 3, pp. 443-454, 2004.

[44] A. Dutt and V. Rokhlin, "Fast Fourier transforms for nonequispaced data," *SIAM J. Sci. Comput.,* vol. 14, issue 6, pp. 1368-1393, 1993.

[45] A. Farhang, N. Marchetti, L. E. Doyle, and B. Farhang-Boroujeny, "Filter bank multicarrier for massive MIMO," *Vehicular Technology Conference (VTC Fall), 2014 IEEE 80th*, pp. 1-7, 2014.

[46] A. Farhang, A. Aminjavaheri, N. Marchetti, L.E. Doyle, and B. Farhang-Boroujeny, "Pilot decontamination in CMT-based massive MIMO networks," *Wireless Communications Systems (ISWCS), 2014 11th International Symposium on,* pp. 589-593, 2014.